Università degli Studi di Pavia
Dottorato di Ricerca in Fisica - XXXV Ciclo

Hidden sectors search at the CMS experiment and predictions for future colliders

Chiara Aimè

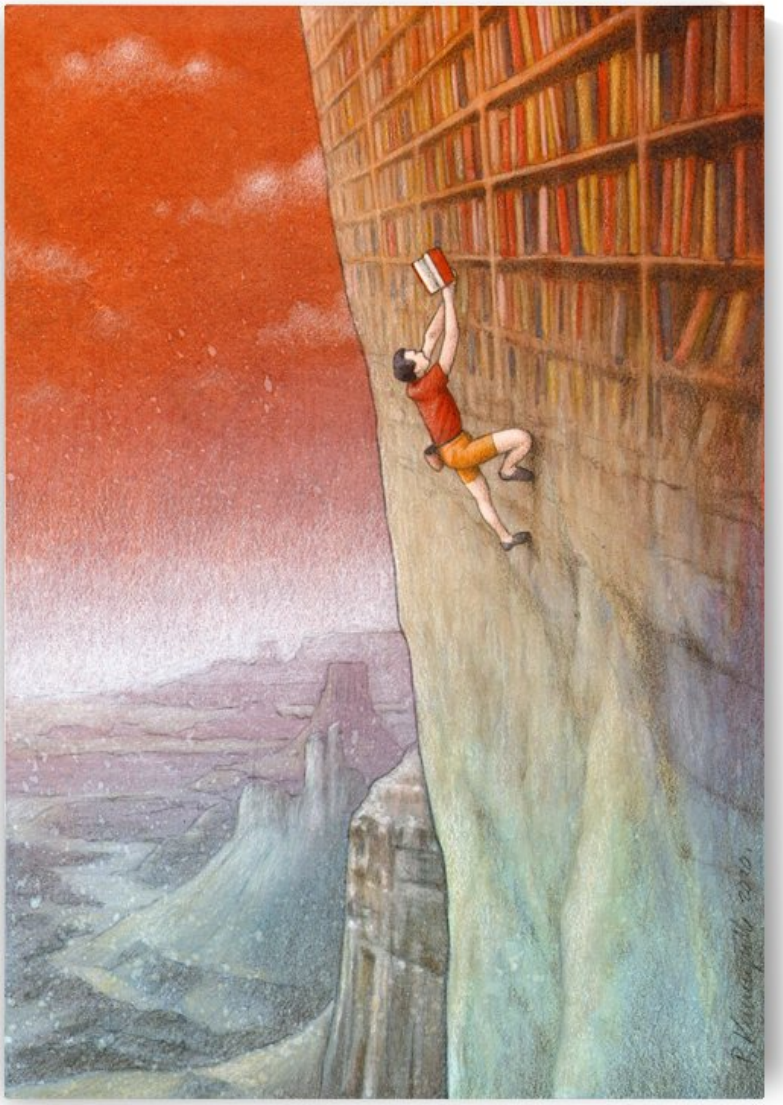

Tesi per il conseguimento del titolo

UNIVERSITÀ
DI PAVIA
Università degli Studi di Pavia

Dipartimento di Fisica

Dottorato di Ricerca in Fisica - XXXV Ciclo

Hidden sectors search at the CMS experiment and predictions for future colliders

Chiara Aimè

Submitted to the Graduate School of Physics in partial fulfillment of the requirements for the degree of *Dottore di Ricerca in Fisica* at the University of Pavia

Supervisor: Prof. Paolo Vitulo

Cover: *Climbing*, Pawel Kuczynski, 2020

Hidden sectors search at the CMS experiment and predictions for future colliders

Chiara Aimè
Ph.D Thesis - University of Pavia
Pavia, Italy, December 2022

It's the questions we can't answer that teach us the most. They teach us how to think. If you give a man an answer, all he gains is a little fact. But give him a question and he'll look for his own answers.

Patrick Rothfuss, *The wise man's fear*

Contents

Introduction

The last sixty years have been a constant stream of achievements for particle physics. The experimental discovery of the Higgs boson, which was for decades just a prediction, decreed the completion of the Standard Model (SM). This gauge theory is the current framework to describe elementary particles and their interactions. Its predictions have been verified with great precision, but many questions remain unsolved.

Why is electroweak symmetry broken and what sets the scale? Is it broken by the SM Higgs or by a richer Higgs sector? Is the Higgs an elementary or a composite particle? What is dark matter made of? What is the origin of the asymmetry between baryons and anti-baryons in the Universe? These are only a few hints that the SM is not the end of the story and there is physics beyond to explore.

In order to try to answer these questions, new theories have been proposed such as supersymmetry (SUSY). This is a generalization of the space-time symmetry of a quantum field theory that associates a fermion to each SM boson and the other way around. It also foresees the existence of a particle, the lightest neutralino, which is one of the most promising candidates for dark matter (DM).

DM is the most fascinating evidence of physics beyond SM. The existence of DM is in fact confirmed by astrophysical observations but its nature is still a mystery. Collections of new particles, called hidden sectors, have been proposed to solve this issue. They are not directly charged under SM strong, weak and electromagnetic forces, and interact with ordinary matter through a mediator. According to the mediator's spin and parity, different portals between SM and DM can be distinguished. The dark-SUSY is a vector-portal hidden sector that adds to the minimal SUSY model the gauge symmetry group $U(1)_D$ that spontaneously breaks giving rise to a light dark photon.

A possible strategy to search for DM exploits the potential of colliders. The latest achievements confirm that these machines are at the forefront of scientific

discoveries in high-energy physics.

The Compact Muon Solenoid (CMS) is one of the experiments hosted along the ring of the Large Hadron Collider (LHC). Together with ATLAS, it announced the discovery of the Higgs boson in 2012 and is still working incessantly to collect data and shed light both on the SM and new physics. In addition to existing apparatus, new colliders are proposed to deepen our understanding of the SM open questions and to tackle novel challenges that might emerge from future discoveries at the LHC. Among these, the Muon Collider would combine the high precision of electron-positron colliders and the high center-of-mass energy and luminosities of hadron machines leading to an unprecedented discovery potential.

In this context, we examine an extension of the dark-SUSY model with a dark Higgs boson, originating from a neutralino, decaying into two dark photons that then decay into pairs of muons. In total, starting from neutralino pair production, eight muons are present in the final state. The thesis deals with the search for this hidden sector in the CMS experiment (Part I) and also furnishes preliminary predictions for a future Muon Collider (Part II).

The work is organised as follows. After a brief introduction about the SM, Chapter 1 presents an overview of the physics beyond the SM, focusing in particular on supersymmetry, dark matter and hidden sectors. Chapter 2 shows the work done from a theoretical point of view to implement the extension of the model to be used in event generators.

Concerning the CMS experiment, Chapter 3 describes the LHC machine with design and operational parameters and the CMS detector with information about physics object reconstruction. Chapter 4 reports the search including signal sample generation, background estimation, analysis strategy for event selection, discussion of systematic uncertainties and statistical interpretation of the limits found on the cross section.

For the Muon Collider, on the other hand, Chapter 5 introduces the physics case and the machine and detector design. The last section is dedicated to studies performed on the muon system. The contribution of the beam-induced background (BIB), i.e. the collection of particles originating from the interaction of electrons and positrons from muon decay with the machine, in this region is examined and different technologies to be implemented are discussed. Finally, Chapter 6 presents the preliminary predictions obtained on the signal yield and the algorithms tested and developed for muon reconstruction with and without the BIB.

Chapter 1

Theoretical overview

Our current knowledge is encompassed in the Standard Model of particle physics, whose development and experimental evidence are here summarised. This, however, is not the end of the story: many questions still unsolved are presented together with one of the new theories proposed, supersymmetry.

Dark matter represents the most compelling piece of evidence of physics beyond the Standard Model. Its existence is confirmed by astrophysics, but its nature is still unknown. Hidden sectors have been suggested as a possible solution. The case of the dark photon is discussed in more detail.

1.1 The Standard Model of particle physics

The Standard Model (SM) of particle physics is the current framework that describes elementary particles and their interactions. Some key issues are here described, further information can be found in Refs. [1, 2, 3, 4]. The SM is a gauge theory, where forces are mediated by the exchange of gauge fields, based on the unitary symmetry group:

$$SU(3)_C \otimes [SU(2)_L \otimes U(1)_Y] \,. \tag{1.1}$$

The two factors in square brackets refer to the electroweak (EW) theory that unifies electromagnetism and weak nuclear force, while the first to Quantum Chromodynamics (QCD), the theory of the strong nuclear interaction. The fourth fundamental force of nature, i.e. gravitation, is not included.

Figure 1.1 summarizes the SM content. The basic constituents of matter are six quarks and six leptons, with their respective antiparticles, divided into three

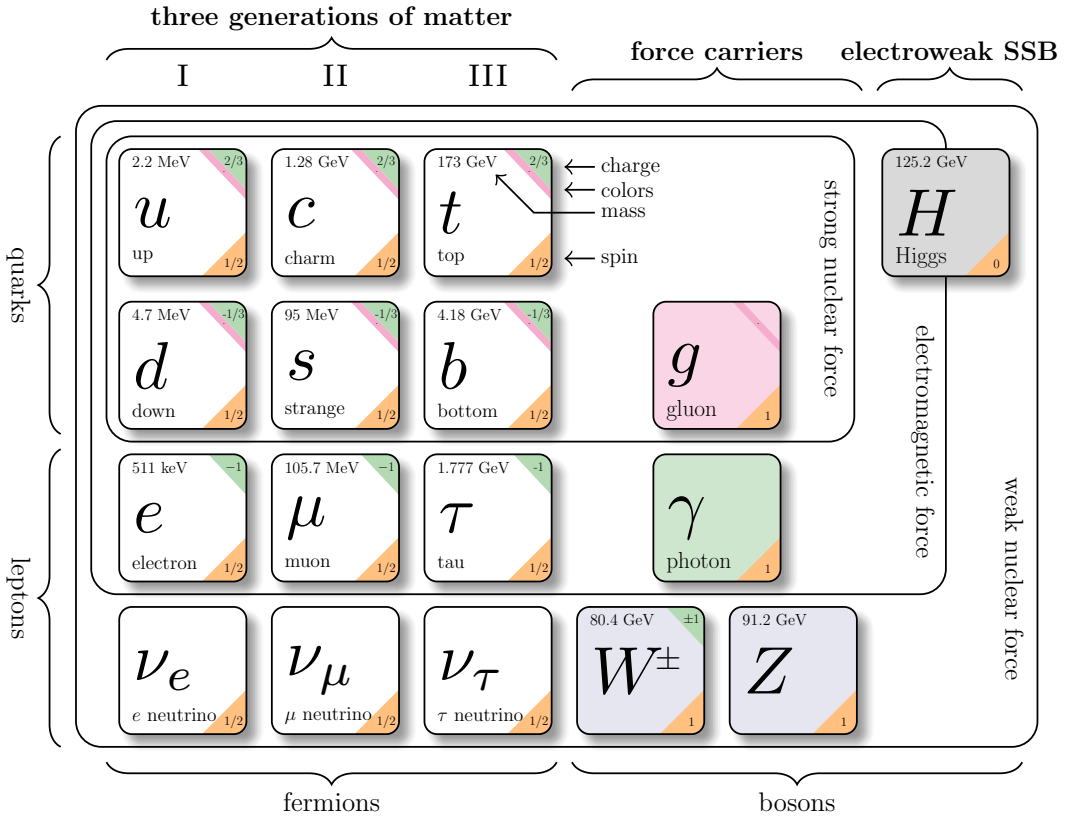

Figure 1.1: Standard Model of particle physics.

generations. They are all fermions (spin $S = \frac{1}{2}$) described by the Dirac spinors ψ satisfying the equation:

$$(i\gamma^\mu \partial_\mu - m)\psi = 0,$$

where γ are the Dirac matrices and m the mass of the particle. They are all massive, except the neutrinos. Leptons interact only weakly and electromagnetically, if charged, while quarks also strongly since they carry color charge.

The force propagators, also called *mediators*, are bosons. The number of gauge bosons for a certain symmetry group $U(n)$ is $n^2 - 1$. Therefore there are: one photon (γ) for the electromagnetic force, the $W^\pm$ and Z bosons for the EW and 8 gluons (g) for the strong interaction.

Quantum Chromodynamics (QCD)

The first and most successful quantum field theory was the Quantum Electrodynamics (QED) presented in the 1940s [5, 6, 7]. All electromagnetic processes can be described in terms of the elementary Feynman diagram

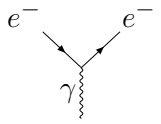

where the vertex $(-ie\gamma^\mu)$ is proportional to the fine structure constant α:

$$\alpha = \frac{e^2}{4\pi} = \frac{1}{137}.$$

The QCD is the non-abelian quantum generalization of the QED and was proposed in 1954 by Yang and Mills [8]. It was promoted to the theory of the strong interaction in 1973-74 with the discovery of asymptotic freedom by Gross, Wilczek [9, 10] and Politzer [11].

The color charge is the analogue of the electric charge but there are some remarkable differences due to the fact that there are three kinds of color (red, blue, and green) and only one electric charge. First of all gluons self-interact because they themselves carry color and anticolor charges. Thus there are tri- and quadri-linear vertices (ggg and $gggg$) that make QCD extremely rich. Moreover, the strong coupling constant α_s is *running*, because it depends on the distance between the interacting particles. At low energy scales, α_s is $\mathcal{O}(1)$, at modern collider energy scales is $\mathcal{O}(10^{-1})$, and $\alpha_s \to 0$ at very high energies. This behaviour is known as *asymptotic freedom* and is due to the fact that the theory is not abelian. Finally, quarks are confined in colorless packages called *hadrons*: mesons (one quark and one antiquark) and baryons (three quarks or three antiquarks).

The electroweak (EW) theory

The EW theory is somehow "rebel", it has to take into account the parity violation proved by the famous experiment of Madame Wu in 1957 [12], the charge-conjugation parity (CP) symmetry violation observed by Christenson, Cronin and Fitch [13], and the spontaneous symmetry breaking (SSB). In 1933 Fermi first described the weak force as a contact interaction of four fields with coupling G_F [14]; the theory was put in its present form in the 1960s by Glashow [15], Weinberg [16] and Salam [17]. The $U(1)_Y$ group in Eq. (1.1) is abelian and Y stands for *hypercharge*, which generalizes the electric charge Q and, according to Gell-Mann and Nishijna formula, is:

$$Q = I_3 + \frac{1}{2}Y,$$

where I_3 is the third component of the isospin, which plays the role of charge in the weak interaction. The subscript L in Eq.(1.1) means *left-handed*[1] and accounts for parity violation. The EW force is successfully described by a $V-A$ (vector minus axial) theory and, in the limit of massless particles charged current processes, i.e. mediated by $W^{\pm}$ bosons, involves only left-handed fermions.

Due to unification, the electric and weak charges are connected through the Weinberg angle θ_w:

$$e = g \sin\theta_w = g' \cos\theta_w.$$

The weak coupling strength is connected to the Fermi constant through:

$$g^2 = \frac{8 G_F m_W^2}{\sqrt{2}}.$$

In the lepton sector, the weak force conserves the flavour as it couples, for example, the electron only with the ν_e, but this is not true for the quarks. The quarks listed in Figure 1.1 are mass eigenstates but not weak eigenstates. In a weak process, the up quark is coupled with d' which is the linear combination of down, strange and bottom quarks according to the Cabibbo-Kobayashi-Maskawa matrix (V_{CKM}) [18, 19]:

$$\begin{pmatrix} d' \\ s' \\ b' \end{pmatrix} = \begin{pmatrix} V_{ud} & V_{us} & V_{ub} \\ V_{cd} & V_{cs} & V_{cb} \\ V_{td} & V_{ts} & V_{tb} \end{pmatrix} \begin{pmatrix} d \\ s \\ b \end{pmatrix}$$

V_{CKM} is not perfectly diagonal and therefore CP-violating processes, such as the decay of baryons Λ^0 and Ω^-, are allowed.

The Higgs mechanism

The Higgs mechanism is an SSB process that permits giving mass to the W and Z bosons, conserving the gauge invariance [20, 21]. It is spontaneous because no external agency is involved and arises from the fact that the vacuum does not share the same symmetry as the Lagrangian.

In the so-called *Minimal Higgs model*, which leads only to a neutral Higgs field, a doublet of complex scalar fields is added:

$$\phi = \begin{pmatrix} \phi^+ \\ \phi^0 \end{pmatrix}.$$

The Lagrangian is:

$$\mathscr{L}_{\mathrm{Higgs}} = (D_\mu \phi)^\dagger (D^\mu \phi) - V(\phi) \tag{1.2}$$

[1] Helicity is defined as the projection of the spin in the direction of motion. A spin-half fermion has two helicity states: right- and left-handed.

with the covariant derivate

$$D^\mu = \partial^\mu + igT_j W_j^\mu - ig'\frac{Y}{2}B^\mu,$$

where T_j are the three generators of the SU(2) symmetry. The potential has the form:

$$V(\phi) = \mu^2\phi^\dagger\phi + \lambda(\phi^\dagger\phi)^2 \tag{1.3}$$

with $\mu^2 < 0$ and $\mu^2 = -\lambda v^2$, where v is the vacuum expectation value. After the SSB the exact symmetry $U(1)_{em}$ is obtained. The four gauge bosons are:

- $W^{\pm\mu} = \frac{1}{\sqrt{2}}(W_1^\mu \mp W_2^\mu)$ with mass $m_W = \frac{1}{2}gv$
- $A^\mu = \frac{g'W_3^\mu + gB^\mu}{\sqrt{(g^2+g'^2)}}$ with mass $m_A = 0$, corresponding to the photon
- $Z^\mu = \frac{gW_3^\mu - g'B^\mu}{\sqrt{(g^2+g'^2)}}$ with mass $m_Z = \frac{1}{2}v\sqrt{(g^2+g'^2)}$.

The mass of the Higgs boson is $m_H = \sqrt{2\lambda}v$ and the vacuum expectation value is found to be $v = 246\,\text{GeV}$.

The Higgs mechanism is responsible also for the mass of fermions through the Yukawa coupling (y_f):

$$\mathscr{L}_{\text{Yukawa}} = -\sum_f y_f \bar{\psi}^f \phi \psi^f. \tag{1.4}$$

The mass of each fermion is given by:

$$m_f = \frac{y_f v}{\sqrt{2}}. \tag{1.5}$$

1.1.1 Experimental evidence of the SM

To summarize, the Lagrangian density of the SM is:

$$\mathscr{L}_{\text{SM}} = \mathscr{L}_{\text{kin, gauge}} + \mathscr{L}_{\text{kin, f}} + \mathscr{L}_{\text{Higgs}} + \mathscr{L}_{\text{Yukawa}},$$

where the first two addends are the kinetic terms for the gauge fields and the fermions respectively, $\mathscr{L}_{\text{Higgs}}$ is the one reported in Eq. (1.2) and $\mathscr{L}_{\text{Yukawa}}$ in Eq. (1.4). The model has 18 free parameters: the masses of the nine charged fermions plus the one of the Higgs boson, the three coupling constants (α, α_s and G_F), the vacuum expectation value of the Higgs v, the three mixing angles and the phase of the CKM matrix.

The first experimental evidence of the SM was the discovery in 1973 of the neutral weak current, i.e. interactions mediated by the Z boson, by Gargamelle at CERN (*Conseil Européen pour la Recherche Nucléaire*) [22, 23]. Ten years

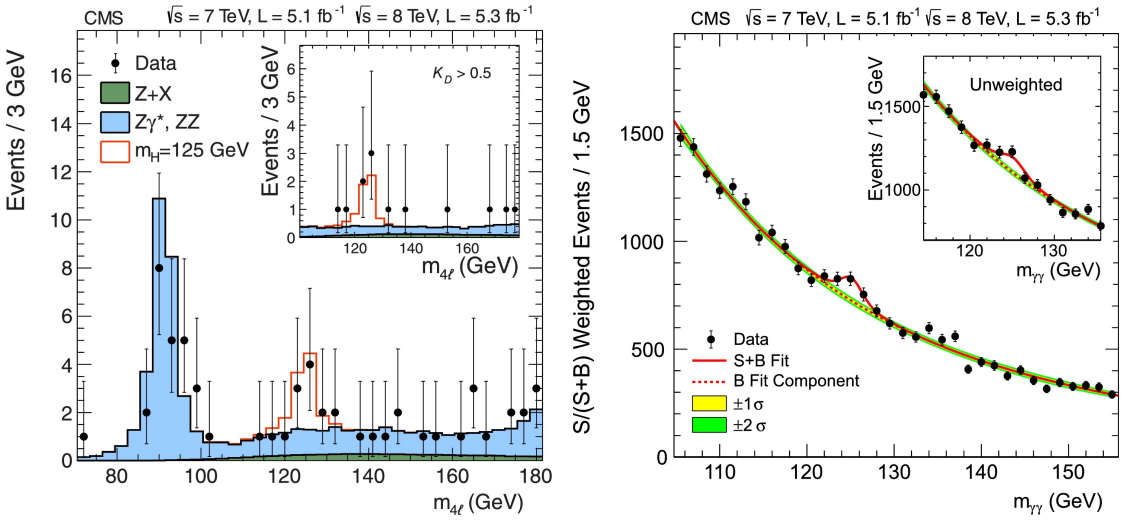

Figure 1.2: Left: Distribution of the four-lepton invariant mass for the $ZZ \to 4\ell$ analysis. The points represent the data, the filled histograms represent the background, and the open histogram shows the signal expectation for a Higgs boson of mass $m_H = 125\,\text{GeV}$, added to the background expectation. Right: The diphoton invariant mass distribution with each event weighted. The lines represent the fitted background and signal, and the colored bands represent the 1 and 2 standard deviations σ uncertainties in the background estimate [31].

later, again at CERN, the two experiments UA1 (Underground Area 1) and UA2 (Underground Area 2) found the $W^{\pm}$ and Z bosons [24]. Experiments at the Large Electron-Positron (LEP) and Tevatron colliders provided extremely precise measurements of the model parameters. Worth mentioning is the confirmation of the existence of three generations of leptons from the decay width of the Z boson [25]. All the particles listed in Figure 1.1 were discovered before the end of the century: in 1975 the Stanford Linear Accelerator Center (SLAC), for example, observed the charm quark in the J/ψ resonance [26], together with Brookhaven National Laboratory [27], and indirectly confirmed the τ lepton [28]. In 1995 the top quark was discovered at the Tevatron [29, 30].

The Higgs boson has remained only predicted for many years. Finally, in 2012, the CMS (Compact Muon Solenoid) [31] and ATLAS (A Toroidal LHC ApparatuS) [32] experiments at CERN announced its discovery. Figure 1.2 shows the signals that confirmed the evidence in $ZZ \to 4\ell$ and $\gamma\gamma$ analyses for the CMS apparatus. This completed the SM of particle physics.

The last result on the W boson mass by the CDF (Collider Detector at Fermilab) experiment [33] is the only measurement not in agreement with the theory and it is added to the list of open questions still unsolved that go beyond the SM.

1.2 Beyond the Standard Model

Despite all the phenomenological confirmations, the SM is not the end of the story. As an example of these outstanding issues, the problem of neutrinos' mass, the matter/antimatter asymmetry, the force unification, and the hierarchy problem are here discussed.

Experiments with solar, atmospheric and reactor neutrinos, such as Super-Kamiokande [34] and SNO (Sudbury Neutrino Observatory) [35], observed the phenomenon of oscillations, i.e. the changing of neutrinos' flavour while they are travelling in space. This can be explained only by abandoning the SM hypothesis of massless neutrinos. The easiest way to extend the SM is the introduction of a right-handed Dirac neutrino that allows writing a Yukawa term of the form in Eq. (1.4). This neutrino is called *sterile* because it is not affected by the EW and strong interactions. Such an extension does not change the nature of the neutrino, but, being the only neutral elementary fermion, it could be a Majorana particle with the antiparticle equal to the particle itself. The observation of a double beta decay with no neutrinos is the experimental evidence expected to confirm this nature. The *see-saw* mechanism is a possible solution to the problem of a Dirac-Majorana neutrino [36]. Because of the oscillation, reasoning similar to one of the quarks can be done. The Pontecorvo–Maki–Nakagawa–Sakata (PMNS) matrix [37, 38] can be introduced in analogy with the CKM matrix to relate weak and mass eigenstates. This can be expressed in terms of four new free parameters, one of which allows for the CP-violation in the leptonic sector. These four plus the three neutrino masses are free parameters to be added to the 18 listed above. Absolute masses are not determined yet, mass-squared differences and mixing angles have been measured by Super-Kamiokande [39], KamLAND [40], T2K [41] and Chooz [42] experiments.

In the early Universe, there was an equal number of baryons and antibaryons ($n_B = n_{\overline{B}}$). Now, however, there is an evident dominance of matter. The process that led to the matter/antimatter asymmetry starting from the baryon symmetric Universe is called *baryogenesis*. The ratio of baryons and antibaryons to photons is:

$$\frac{n_B - n_{\overline{B}}}{n_\gamma} = 10^{-9}.$$

Sakharov in 1957 listed the three conditions that generated such an imbalance: the violation of baryon number conservation, the CP-violation and the non-thermal equilibrium [43]. The SM predicts the CP-violation by the EW force in the quark and lepton sectors connected to the complex phase in CMK and PMNS matrices. In the quark sector, it has been observed firstly indirectly in K^0 decays in 1964 by Christenson, Cronin and Fitch and directly in 2001 at BaBar and Belle experiments in the B^0 decays [44, 45]. Finally, the LHCb experiment announced the discovery of CP-violation in B_s^0 [46] and D^0 decays [47]. But there are no

pieces of evidence up to now of CP-violation for neutrinos that might shed light on the so-called *leptogenesis*, the model for baryogenesis through the lepton number violation. Moreover, CP-violation in the strong interaction is given by a phase (θ_{QCD}) in the QCD Lagrangian that has been found very small experimentally $\theta_{QCD} < 10^{-10}$ [48]. This phase is the 26th free parameter of the SM. All these SM-accounted CP-violating terms are insufficient to explain the matter/antimatter asymmetry. Solutions have to be found beyond the Standard Model (BSM). Today the only explanation for such a small number, together with many other outstanding issues, is given by Grand Unified Theories (GUTs) that unify strong, weak and electromagnetic interactions at a certain scale of energy M_{GUT}. The first GUT was the one by Georgi and Glashow in 1974 [49], they accommodated the SM symmetry in Eq. (1.1) within a $SU(5)$ symmetry.

The running of the three proper renormalised gauge coupling constants (α_a)

$$\alpha_1 = \frac{5}{3}\frac{g'^2}{4\pi}, \qquad \alpha_2 = \frac{g^2}{4\pi}, \quad \text{and} \quad \alpha_3 = \alpha_s$$

is a hint of unification. From the values measured at the EW scale (M_Z), using the renormalization group equation (RGE):

$$\frac{1}{\alpha_a(\mu^2)} = \frac{1}{\alpha_a(M_Z^2)} - 4\pi b_a \ln\frac{\mu^2}{M_Z^2},$$

where b_a are the number of fermions and boson loops to gauge boson self-energy, the evolution shown in Figure 1.4 (left) is obtained. In QED b_1 is positive and α_1 decreases because photon self-energy presents only fermion loops. In EW and QCD, instead, there are also boson loops and the constants increases with energy. In the SM they converge at a scale $M_{\text{GUT}} \sim 10^{15}\,\text{GeV}$, although not exactly at the same value. This is orders of magnitude below the Planck scale ($M_P \sim 10^{19}\,\text{GeV}$) where quantum effects of gravity are expected to dominate and are closely related to the so-called *hierarchy problem*.

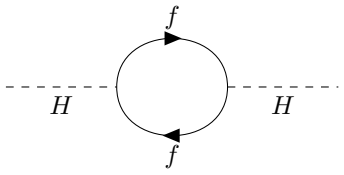

Figure 1.3: A fermion antifermion contribution to the self-energy of the Higgs boson in the SM.

This issue concerns one-loop corrections to scalar bosons' mass. In the SM the only scalar boson is the Higgs boson. From loop diagrams as the one in Figure 1.3 the tree level mass received quadratically divergent quantum corrections

$$m_H^2 = (m_H^2)_{\text{tree level}} + \mathcal{O}(\lambda, g^2, y_f)\Lambda^2,$$

with λ the coupling of the potential in Eq. (1.3), g the weak coupling strength and y_f the fermion Yukawa coupling as in Eq. (1.5). In the context of the SM

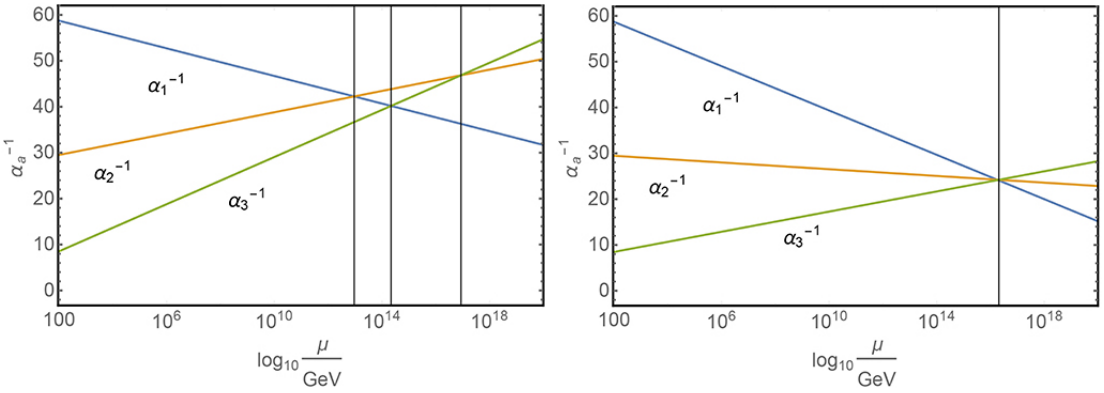

Figure 1.4: Running of the coupling constants for $SU(3)_C$ in green, $SU(2)_L$ in orange and $U(1)_Y$ in blue for the SM (left) and the Minimal Supersymmetric Standard Model (right) [50].

interpreted as an effective field theory, Λ is the cut-off scale, i.e. the mass scale of particles BSM. If Λ is of the order of the unification scale in GUT, or even worse of the Planck mass, the correction is enormous. The measured parameter m_H appears to be finely tuned, i.e. much smaller than the expected value and with huge corrections. The so-called *naturalness criterion* [51] states that, in an effective field theory, any parameter measured in unit of Λ is allowed to be smaller than unity only if setting it to zero increases the symmetry of the theory [52]. In the SM in the limit of a massless electron, the chiral symmetry appears, but no symmetry protects the Higgs mass. Thus, the naturalness paradigm suggests exploring new physics and an elegant solution to the hierarchy problem is provided by supersymmetry.

1.2.1 Supersymmetry

Supersymmetry (SUSY) is any symmetry which connects particles and fields with different spin-statistics. Since the early 1970s, many supersymmetric theories have been proposed and their mathematical structure has been defined. A detailed description of the algebra is reported in Refs. [53, 54, 55]. To summarize, SUSY algebra is generated by anticommuting generators Q with spin 1/2 that, therefore, transform fermions into bosons and the other way around:

$$Q|\text{fermion}\rangle = |\text{boson}\rangle$$
$$Q|\text{boson}\rangle = |\text{fermion}\rangle.$$

Particles and their associated superparticles, called *superpartners*, have the same electric, weak isospin, and color charge, and are degenerate in mass. They are

grouped in supermultiplets:

$$\begin{pmatrix} q \\ \tilde{q} \end{pmatrix} \qquad \text{spin} \begin{pmatrix} 1/2 \\ 0 \end{pmatrix},$$

where q is any quarks taken as an example. Fermions are coupled with sfermions, where the initial s stands for scalar, while bosons with bosinos.

As already mentioned, SUSY is the most appreciated solution to the hierarchy problem. Going back to the correction to Higgs boson's mass, for any loop of particles as the one in Figure 1.3 there is a corresponding sparticle loop with an opposite sign that allows canceling the divergence. This is true if partners in the supermultiplet have the same mass, but SUSY has to be broken because no supersymmetric particle has been observed yet. The mass difference between ordinary particles and sparticles is of the order of the SUSY breaking scale. To keep the Higgs mass small $\mathcal{O}(100\,\text{GeV})$, SUSY particles are expected to have a mass of around 1 TeV and to be detected at powerful enough accelerators. SUSY phenomenology strongly depends on the breaking mechanism.

Minimal Supersymmetric Standard Model

The simpler SUSY extension of the SM is the so-called Minimal Supersymmetric Standard Model (MSSM) where soft mass terms are introduced and the gauge coupling constants for sparticles are the same as particles. In MSSM, these constants converge exactly at the same value at the scale M_{GUT} (see Fig. 1.4 right).

The particle content is summarised in Table 1.1. The Higgs sector is rich compared to SM. Two complex Higgs doublets

$$H_1 = \begin{pmatrix} H_u^+ \\ H_d^0 \end{pmatrix} \quad \text{and} \quad H_1 = \begin{pmatrix} H_u^0 \\ H_d^- \end{pmatrix}$$

are required to give mass to charged 2/3 and -1/3 quarks and to ensure the cancellation of gauge anomalies, i.e. higgsinos that appear as internal lines in triangle diagrams with three external EW gauge bosons. The two doublets have eight degrees of freedom: three give mass to W^+, W^- and Z, and the others are the Higgs sectors. H^0, h^0 and $H^\pm$ are CP-even neutral and charged bosons respectively, A is a CP-odd neutral pseudoscalar. The h_0 corresponds to the Higgs boson found by ATLAS and CMS. Gauginos and higgsinos are not mass eigenstates. These last, called *neutralinos*[2] and *charginos*, are linear combinations:

$$\widetilde{\chi}_i^0 = a_i\widetilde{\gamma} + b_i\widetilde{Z} + c_i\widetilde{H_u^0} + d_i\widetilde{H_d^0} \quad \text{with} \quad i = 1, 2, 3, 4$$

[2]In this work the lightest supersymmetric neutralino is referred to as $\widetilde{N}_1$, n_1 or $\widetilde{\chi}_1^0$ equivalently.

$$\widetilde{\chi}^+ = a'\widetilde{W}^+ + b'\widetilde{H}_u^+ \qquad \widetilde{\chi}^- = c'\widetilde{W}^- + d'\widetilde{H}_d^- .$$

The MSSM has 105 additional free parameters. It has also another discrete symmetry, the R-parity, defined as:

$$R = (-1)^{3(B-L)+2S},$$

with B and L baryonic and leptonic numbers and S spin. Ordinary particles are R-even while sparticles are R-odd. In MSSM R-parity is conserved and, because of this, SUSY particles are always produced in pairs, and the lightest supersymmetric particle (LSP) is stable and therefore a good candidate for dark matter (see Section 1.2.2).

Table 1.1: Ordinary particles and superpartners, including right-handed particles and mass eigenstates.

Ordinary particles			SUSY particles			
Quarks			Squarks			
spin 1/2	$\begin{pmatrix} u \\ d \end{pmatrix}_L$	$u_R\ d_R$	spin 0	$\begin{pmatrix} \widetilde{u} \\ \widetilde{d} \end{pmatrix}_L$	$\widetilde{u}_R\ \widetilde{d}_R$	
	$\begin{pmatrix} c \\ s \end{pmatrix}_L$	$c_R\ s_R$		$\begin{pmatrix} \widetilde{c} \\ \widetilde{s} \end{pmatrix}_L$	$\widetilde{c}_R\ \widetilde{s}_R$	
	$\begin{pmatrix} t \\ b \end{pmatrix}_L$	$t_R\ b_R$		$\begin{pmatrix} \widetilde{t} \\ \widetilde{b} \end{pmatrix}_L$	$\widetilde{t}_R\ \widetilde{b}_R$	$\rightarrow \widetilde{t}_{1,2}\ \widetilde{b}_{1,2}$
Leptons			Sleptons			
spin 1/2	$\begin{pmatrix} \nu_e \\ e \end{pmatrix}_L$	e_R	spin 0	$\begin{pmatrix} \widetilde{\nu_e} \\ \widetilde{e} \end{pmatrix}_L$	$\widetilde{e}_R$	
	$\begin{pmatrix} \nu_\mu \\ \mu \end{pmatrix}_L$	μ_R		$\begin{pmatrix} \widetilde{\nu_\mu} \\ \widetilde{\mu} \end{pmatrix}_L$	$\widetilde{\mu}_R$	
	$\begin{pmatrix} \nu_\tau \\ \tau \end{pmatrix}_L$	τ_R		$\begin{pmatrix} \widetilde{\nu_\tau} \\ \widetilde{\tau} \end{pmatrix}_L$	$\widetilde{\tau}_R$	$\rightarrow \widetilde{\tau}_{1,2}$
Gauge bosons			Gauginos			
spin 1	g		spin 1/2	$\widetilde{g}$		
	γ			$\widetilde{\gamma}$		
	Z			$\widetilde{Z}$		Neutralinos
	$W^\pm$			$\widetilde{W}^\pm$		$\rightarrow \widetilde{\chi}^0_{1,2,3,4}$
Higgs bosons			Higgsinos			Charginos
spin 0	$H^0\ h^0\ A^0$		spin 1/2	$\widetilde{H}_u^0\ \widetilde{H}_d^0$		$\rightarrow \widetilde{\chi}^\pm_{1,2}$
	$H^+\ H^-$			$\widetilde{H}_u^+\ \widetilde{H}_d^-$		

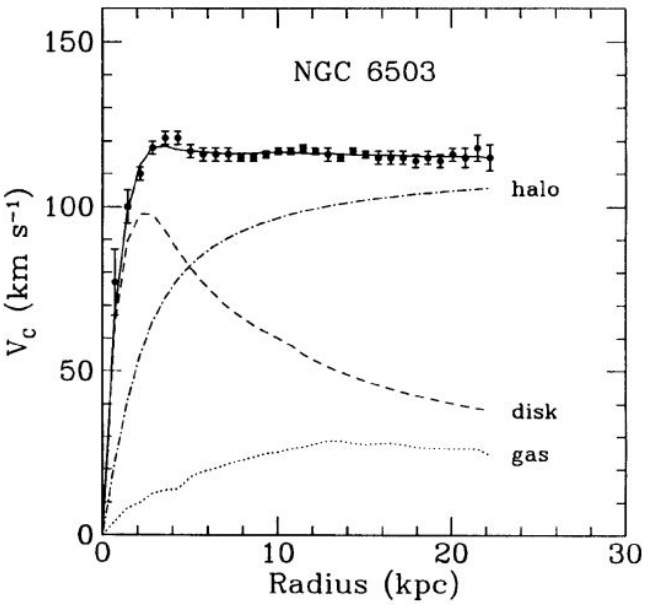

Figure 1.5: Rotation curves for the spiral galaxy NGC6503. The rotation velocity is plotted from the centre of the galaxy to the edges. The black dots show the measured values, and the solid line is the curve that best fits the measurements when dark matter and matter in the stars are included. If the galaxy consisted of just matter in the disk the curve would be the dashed line. The dotted/dashed line is the curve needed from the extra dark matter in the halo. The dotted curve is the contribution of the gas [61].

Experimental evidence

Up to now, no supersymmetric particle has been detected. Experiments simply put exclusion limits which depend on the model. In general, inclusive searches at the Large Hadron Collider (LHC) probe production of gluinos at 2.3 TeV, first and second generation quarks in the range 1-1.9 TeV while third generation quarks in 0.6-1.2 TeV, EW gauginos at scales of 400 to 1100 GeV and sleptons around 700 GeV [56]. All the results for the CMS experiment can be found in [57].

1.2.2 Dark matter

Dark matter (DM) is the most compelling evidence of physics BSM. It does not interact with any type of matter other than the pull of gravity and we do not know what it is [58]. The first evidence dates back to 1933 when Fritz Zwicky observed that the Coma cluster rotates faster than expected on the outside, suggesting the presence of additional and not visible matter [59]. DM was accepted later in the 1970s with the studies of Vera Rubin [60]. The typical astronomical indirect clues of the existence of DM are the rotational velocity of galaxies and the gravitational lensing.

Looking at the light from a spiral galaxy, the number and the mass of stars can be estimated. Then, using the standard equation of gravity, it is possible to calculate the rotational velocity. This is expected to decrease as $1/\sqrt{r}$ moving from the centre towards the edges as shown by the curve labelled "disk" in Figure 1.5. However, the values measured with the Doppler effect remain constant and this

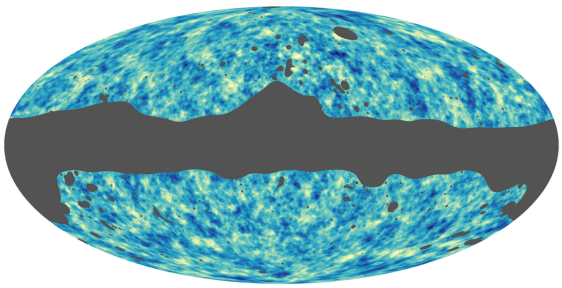

Figure 1.6: A map from Planck Collaboration of dark matter across the whole sky produced by gravitational lensing of CMB. Dark blue areas are where the dark matter is denser, and light yellow areas have less dark matter. The solid grey strip across the centre has been blocked out and is where the light from the Milky Way would be [64].

can be explained only by adding the contribution of a dark matter halo.

Gravitational lensing, instead, is the phenomenon of light magnification and distortion due to the presence of a massive object. It was first used for the Bullet Cluster, which are two colliding clusters of galaxies, to evaluate the distribution of DM [62]. In the last years, the Planck Collaboration[3] used the gravitational lensing of Cosmic Microwave Background (CMB) to map DM across the whole sky (see Figure 1.6), and recently it has been used to probe the distribution of dark matter around some of the earliest galaxies in the Universe, at a redshift of 4 [63].

Dark matter and CMB are two fundamental ingredients of the Standard Model of cosmology.

Standard Model of cosmology: ΛCDM

The Lambda Cold Dark Matter (ΛCDM) model is the current Standard Model of cosmology. Its key ingredients are the Big Bang, dark matter and dark energy. Λ, in fact, is the name initially given by Einstein to the cosmological constant in the general relativity field equation to describe a static Universe and was chosen at the end of the 20th century to refer to dark energy, the one responsible for the acceleration in Universe's expansion. The model is based on the

- cosmological principle, according to which the Universe is homogeneous and isotropic,
- expanding Universe, i.e. every galaxy is moving away from other galaxies with a velocity of recession
$$\frac{dl}{dt} = H_0 l$$
, where l is the mean distance between two objects and H_0 the Hubble constant at present time,
- general relativity,

[3]Planck was the first ESA (European Space Agency) mission to study the Cosmic Microwave Background.

Table 1.2: Some of the possible important events during the evolution of the Universe [65].

Events	E (GeV)	time	T (°K)
Big Bang	∞	0	∞
Planck scale	10^{19}	10^{-44} s	10^{32}
Grand Unification	10^{15}	10^{-37} s	10^{28}
L-violation, SUSY, baryogenesis, inflation, ...			
EW symmetry breaking	10^{2}	10^{-10} s	10^{15}
QCD chiral symmetry breaking and color confinement	10^{-1}	10^{-5} s	10^{12}
Nucleosynthesis	10^{-4}	100 s	10^{9}
Matter dominates over radiation, formation of atoms and decoupling of matter and radiation	2×10^{-10}	3×10^{5} y	3000
Formation of large scale structures	10^{-12}	10^{9} y	15
Present Universe	2.3×10^{-13}	13.7×10^{9} y	2.73

- CMB, i.e. the relic radiation from the Big Bang.

Table 1.2 shows some of the important events during the Universe's evolution that begins with the so-called *Big Bang*. The Universe's temperature is the average energy per particle at a given time; as it expands, the Universe starts to cool and the cooling allows for different physical processes. All the phase transitions correspond to gauge symmetry breaking of particle physics. Therefore, increasing the energy to unification scales (Fig. 1.4) is equivalent to looking back in the past. As an example, L-violation is the lepton number violation responsible for the asymmetry in matter and antimatter.

The evolution depends crucially on the total energy-matter density Ω, which is linked to the Universe's curvature. From CMB deviations from a black-body curve at ~ 2.73°K [66], the total density is measured:

$$\Omega = 0.9993 \pm 0.0019$$

compatible with the value of 1 of a flat geometry. The most updated values for cosmological parameters here reported are taken from Ref. [67]. Baryonic matter, dark matter, radiation (photons and relativistic neutrinos) and dark energy contribute to Ω:

$$\Omega = \Omega_b + \Omega_{DM} + \Omega_\gamma + \Omega_\Lambda. \tag{1.6}$$

Each density is normalised to the critical density (ρ_c):

$$\Omega_x = \frac{\rho_x}{\rho_c} \quad \text{with} \quad \rho_c = \frac{3H_0}{8\pi G}$$

, where G is the gravitational constant and H_0 is usually written in terms of h_0:

$$H_0 = 100 h_0 \frac{\text{km}}{\text{s Mpc}} \quad h_0 = 0.677 \pm 0.004.$$

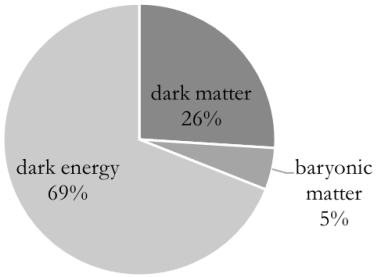

Figure 1.7: Pie chart of Universe energy density.

In Eq. (1.6) Ω_γ is negligible and the remaining three parameters are $\Omega_b = 0.0486 \pm 0.0010$, $\Omega_{DM} = 0.2589 \pm 0.0057$, and $\Omega_\Lambda = 0.6911 \pm 0.0062$. Thus, dark matter contributes to $\sim$ 26% of the entire density of the Universe and $\sim$ 85% of the total mass (see Fig. 1.7). According to the ΛCDM model, DM is cold, i.e. moving at not relativistic speed. In fact, computer simulations [68] proved that only cold dark matter matches the cosmic web which is the interconnected walls and filaments galaxies are arranged in.

Many candidates have been suggested as dark matter constituents. The first solution was a baryonic matter of astronomical remnants such as white dwarfs, neutron stars and black holes. These objects were called MAssive Compact Halo Objects (MACHO), but from gravitational lensing observations, it is evident that they can not account for all dark matter. Besides, MACHO do not explain the baryonic acoustic oscillation, i.e. the oscillations of matter in the very early Universe that created the temperature fluctuations in the CMB and a distinct distance that galaxies prefer to be apart from each other (today it is 490 million light-years). Therefore, non-baryonic candidates are now seriously investigated: axions, the already mentioned sterile neutrinos and Weakly Interacting Massive Particles (WIMPs). Moreover, there are complex models including a full dark matter sector that will be described in Section 1.3.

Axions are particles hypothesised by Peccei and Quinn [69] with no charge and weakly interacting with light but not matter. They offer a solution to many problems beyond that of DM, such as the strong CP-violation.

WIMPs, as the name suggests, are cold, heavy and weakly interacting particles. The most notable example of WIMP is the LSP of the MSSM.

Detection of dark matter

There are three strategies to search for DM: experiments essentially "make it, break it or shake it". It corresponds, respectively, to the production of DM particles at colliders, indirect and direct detection (see Figure 1.8).

Direct searches look for the elastic scattering of DM off nuclei. They detect nuclear recoil through ionization, scintillation light in sodium iodide or liquid noble gas detectors, and energy deposition in bolometers. The signal is very small: for a neutralino of mass in the range 10 GeV-1 TeV the deposited energy is below 100 keV. They are also very rare events, for a target nucleus of mass m_N with a DM flux ϕ_X the rate is:

$$R_{\text{direct}} = \frac{1}{m_N}\phi_\chi \sigma_{XN} = \frac{1.4}{m_X[\text{GeV}]}\text{kg}^{-1}\text{yr}^{-1},$$

where σ_{XN} is the nuclear-DM cross section. In general, the cross section can depend or not on nuclear isospin, and interactions are called respectively SD (spin dependent) or SI (spin independent). In SI the cross section is simply a function of the atomic number of the target nucleus. Experiments, like XENON [70] in Europe, LUX [71] in North America and PandaX [72] in China, have found no particle yet, but put strong limits on the cross section. Figure 1.9 shows the recent results of SI interaction for WIMPS searches.

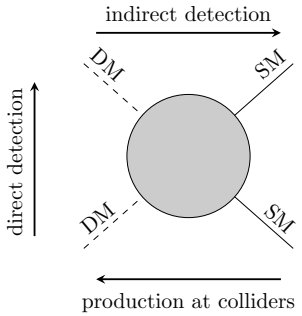

Figure 1.8: Strategies for dark matter (DM) searches.

Indirect detection looks for the decay products from DM annihilation: gamma rays (observed by telescopes such as Fermi-LAT [73], HESS [74], and VERITAS [75]), neutrinos (detected by experiments like IceCube [76]), and antimatter (AMS [77] spectrometer on the International Space Station). Any excess in the observation of these particles, not accounted for by any other source, is a signal of dark matter. An example is the discovery of an unexplained excess of high-energy positrons in cosmic rays by the AMS experiment in 2013 [78]. As for direct detection, the events are very rare. For a flux of neutrinos ϕ_ν, assuming P the probability to detect a neutrino, the rate is:

$$R_{\text{indirect}} = \phi_\nu P = \frac{1.8}{m_X[\text{GeV}]}\text{kg}^{-1}\text{yr}^{-1}.$$

Finally, at colliders, DM is tentatively produced by colliding SM particles. This leads to a variety of signatures such as the imbalance in the transverse momentum in an event due to the presence of undetectable dark matter particles or a bump in the di-jet or di-lepton invariant mass distributions. No one of these signals has been observed in the LHC experiments so far, but limits on the cross section have been put and compared with the ones from direct searches. The most recent results from ATLAS and CMS have been presented in [79].

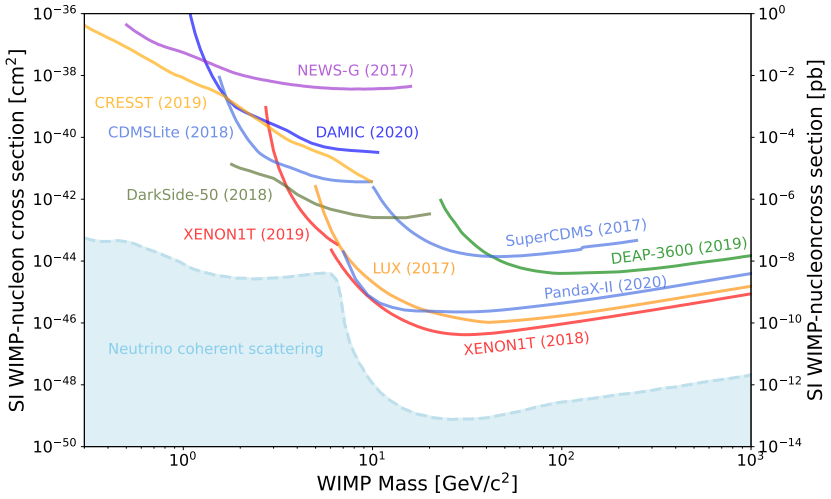

Figure 1.9: Upper limits on the spin independent DM-nucleon cross section as a function of DM mass [56].

1.3 Hidden sectors

Astrophysical observations confirmed the presence of dark matter, but its nature is still a mystery. Many solutions have been suggested to explain it and some of these ideas incorporate DM particles in the so-called *hidden sectors* or *dark sectors* They are collections of several new types of particles (dark bosons, fermions and scalars) that are not directly charged under SM strong, weak and electromagnetic forces, and interact with ordinary matter through a mediator. A detailed review is reported in Refs. [80, 81].

Dark sectors are so interesting because they can easily explain the known gaps of the SM model, such as naturalness, dark matter abundance and interaction, baryon asymmetry and neutrino masses. They might account for the enhancement of positron fraction in cosmic rays [82] or for the total CMB radiation energy density [83], and they appear naturally in GUT theories and SUSY models [84]. Moreover, a non-trivial hidden sector could affect high-precision measurements such as the anomalous magnetic momentum [85] of the muon or the proton charge radius [86].

According to the aforementioned mediator's spin and parity, different portals between SM and DM can be distinguished: spin-1 vector (dark photon and Z boson), spin-0 scalar (dark Higgs), spin-1/2 fermion (sterile neutrino) and pseudoscalar (axion). The gauge operators are shown in Figure 1.10. The case of the dark photon is discussed in detail because it is of interest to this work.

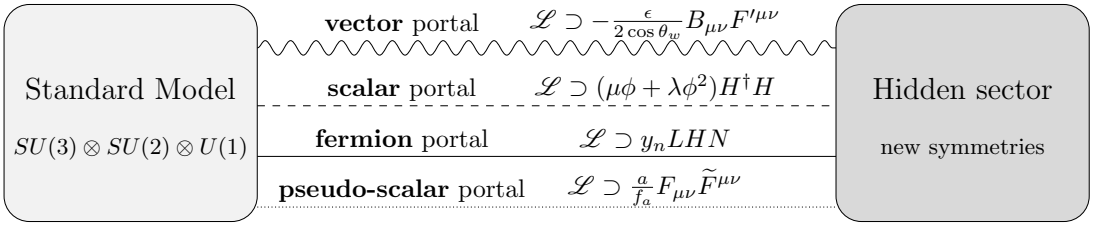

Figure 1.10: Dark sectors portals with gauge operators. Above, ε is the kinetic mixing parameter, $B_{\mu\nu}$, $F_{\mu\nu}$ and $F'^{\mu\nu}$ are the hypercharge, the SM photon and $U(1)_D$ boson field strength tensors respectively. H is the SM Higgs doublet (H^+, H^-), L is a lepton doublet of any generation. In the fermionic portal, the mediator N plays the role of a right-handed neutrino with Yukawa coupling y_n. In the pseudo-scalar portal, a is the axion mediator with mass scale f_a.

1.3.1 Dark photon

The prototypical hidden sector foresees a dark photon[4] from a spontaneously broken dark $U(1)_D$ gauge symmetry. It is present in many models, one of which will be described in the next chapter, to explain the excesses of gamma rays at the centre of the galaxy and of antiprotons in cosmic rays, and the abundance in excited Beryllium decays.

The interaction takes place because of the mixing of the dark and visible photons. Therefore, the parameters are the kinetic mixing term ε and mass $m_{A'}$. A massless dark photon does not couple directly to any SM currents and requires operators of dimensions higher than four to explain the interaction with ordinary matter. A great deal of effort has been put into this as reported in Refs. [87, 88, 89]. A massive dark photon, on the other hand, is produced through *Bremsstrahlung* with target nuclei N ($e^- N \to e^- N A'$), annihilation ($e^- e^+ \to \gamma A'$), meson decay ($\pi^0/\eta/\eta' \to \gamma A'$, $K \to \pi A'$ or $\phi \to \eta A'$) and Drell-Yan ($q\bar{q} \to A' \to$leptons/hadrons). The detection techniques are: bump hunt in visible final state invariant mass, bump hunt in missing mass and vertex detection. Figure 1.11 illustrates the strategies for the visible dark photon, i.e. the one with mass $m_{A'} > 2m_e \sim 1\,\text{MeV}$. The horizontal axis is related to the available kinetic energy while the vertical to the integrated luminosity (increasing downwards). The diagonal direction corresponds to the increasing decay length. The

[4]In this work the dark photon is referred to as A', Z_D or γ_d equivalently.

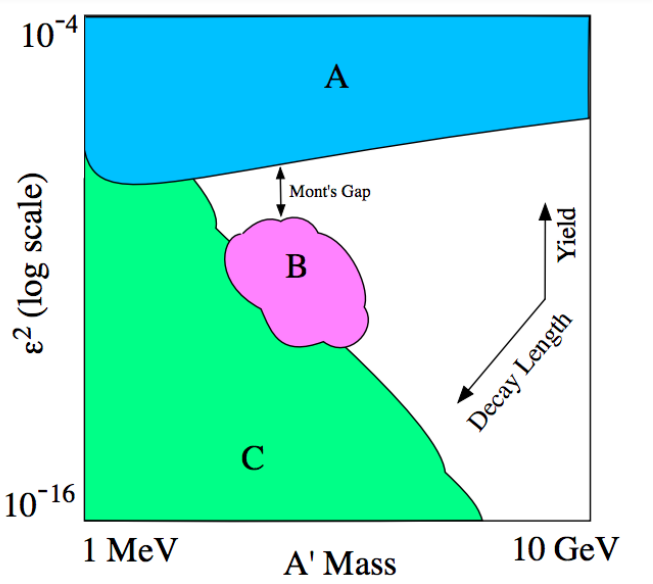

Figure 1.11: Cartoon of the sensitivity regions for the three generic experimental approaches in the ε^2 vs A' mass parameter plane. Region A includes prompt decays to (in)visible particles and bump hunt for resonance (missing mass). Region B and C represent displaced vertex searces with short and long decay lengths, respectively [81].

so-called *Mont's gap* could be closed from above improving the systematics with increased luminosity and from below with a great vertex resolution.

No single experimental approach is sufficient alone to cover the large parameter space. Collaborations and synergies are mandatory. The current constraints for the visible dark photon are shown in Figure 1.12. Similar results and perspectives for the non-visible massive dark photon are reported in Ref. [90]. Two kinds of complementary methods are involved: beam dumps and experiments at colliders with the latter typically sensitive to larger values of ε ($\varepsilon > 10^{-3}$) and mass. Collider experiments exploit different production mechanisms: meson decays at NA48/2 [91], *Bremsstrahlung* at A1 [92], annihilation at BaBar [93] and all three of them at KLOE [94, 95, 96, 97]. The LHC (CMS [98] and LHCb [99]) uses meson decays, *Bremsstrahlung* and Drell-Yan. At the beam dump experiments (E141 [100] and E137 [101] at SLAC, E774 [102] at Fermilab, CHARM [103] at CERN, ν-Cal [105, 104]) the collisions of an electron or proton beam with a fixed-target produce dark photons via *Bremsstrahlung*, meson production and QCD processes. Recent results from CMS and ATLAS are not included because framed within restrictive models, a selected list is discussed in Ref. [106]. Bounds from supernovae (SN1987A) [107] and from the precise determination of the electron magnetic momentum [85] are also shown.

The goal for future machines is to close the gap between beam dumps and colliders and extend to larger masses. The sensitivity of future experiments is shown in Figure 1.13. The results reported for future proton-proton colliders [119], i.e. High-Luminosity LHC (HL-LHC) and hadron Future Circular Collider (FCC-hh), are worth discussing in light of the work presented in this thesis. So far, only the

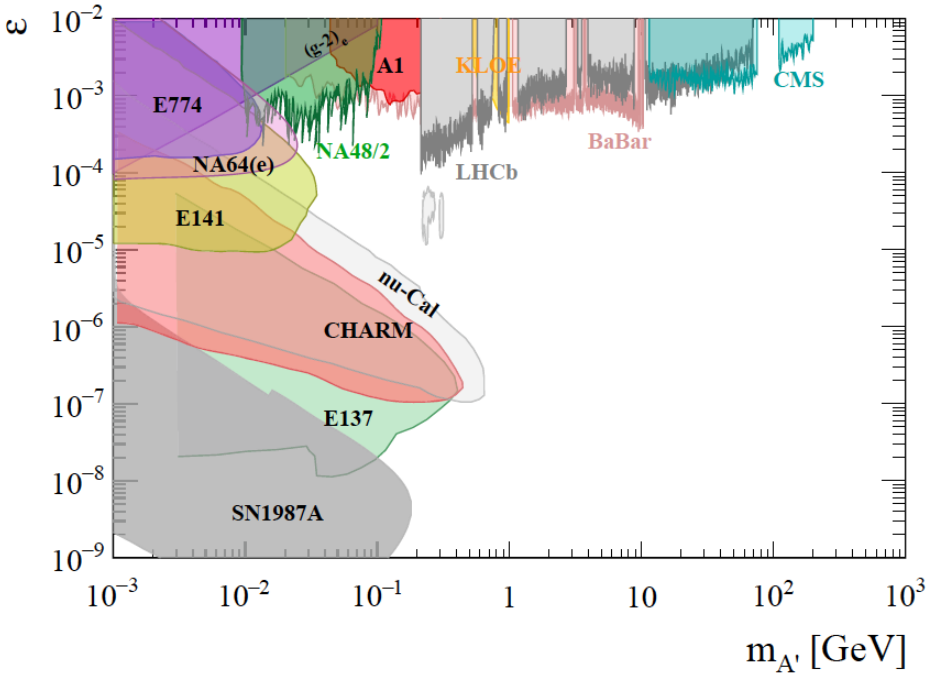

Figure 1.12: Existing limits on the massive dark photon for $m_{A'} > 1\,\text{MeV}$ from di-lepton searches at experiments at collider/fixed target (A1, NA48/2, KLOE, CMS, LHCb, BaBar) and beam dump (E141, E137, E774, CHARM). Bounds from supernovae and (g-2)$_e$ are also included. Figure taken from [90].

mixing ε between the dark photon and the ordinary hypercharge gauge bosons has been considered. In addition, a dark Higgs mechanism can be responsible for the $U(1)_D$ spontaneous symmetry breaking. In this case, the dark Higgs boson has a renormalizable coupling κ' to the 125 GeV SM-like Higgs. The hypercharge (or vector) portal allows for the direct production of the dark photon ($pp \to Z_D \to$lepton pair) and generates the exotic Higgs decay ($h \to ZZ_D$) in Figure 1.14 top left. The scalar portal with Higgs mixing allows for $h \to Z_D Z_D$ decay (Fig. 1.14 top right). In this last case, for a dark photon mass in the range $2m_\mu < m_{Z_D} < m_{h/2}$, a kinetic mixing parameter $\varepsilon = 10^{-9} - 10^{-6}$ and $\varepsilon = 10^{-10} - 10^{-7}$ can be investigated at the HL-LHC and FCC-hh respectively. The expected 95% confidence level (CL) limits on κ' at the LHC and future hadronic collider are shown in Figure 1.14 at the bottom. Since the SM predicts a very narrow decay width for the Higgs, even a small coupling to the new particles could result in a significant branching fraction, i.e. the ratio of the number of particles which decay via a specific decay mode with respect to the total number of particles which decay via all decay modes.

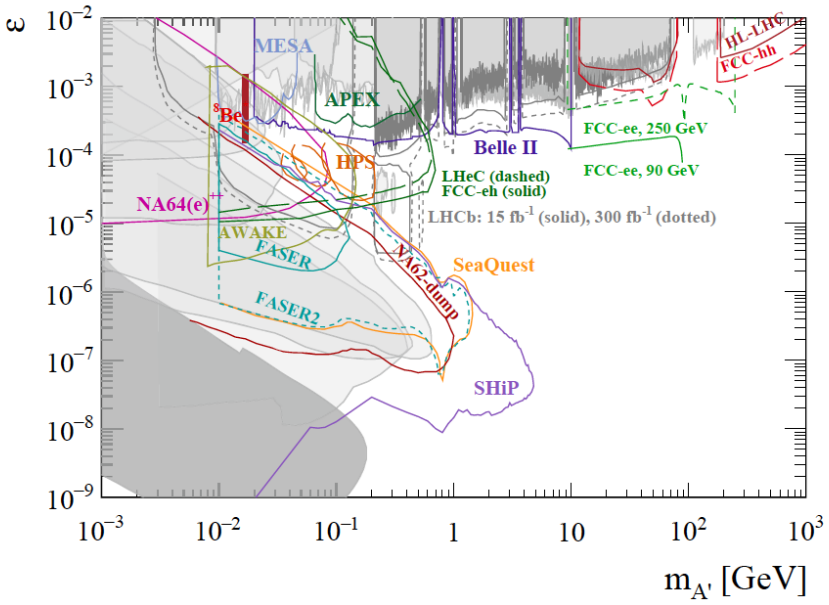

Figure 1.13: Colored curves are projections for existing and proposed experiments on the massive dark photon for $m'_A > 1\,\text{MeV}$: Belle-II [108] at SuperKEKb; LHCb [109, 110] upgrade at the LHC; NA62 [111] in dump mode and NA64(e)++ [112] at the SPS; FASER and FASER2 [113] at the LHC; SeaQuest [114] at Fermilab; HPS [115] at JLAB; an NA64-like experiment at AWAKE [116], and an experiment dedicated to dark photon searches at MESA [117, 118]. For masses above 10 GeV projections obtained for ATLAS/CMS during the high luminosity phase of the LHC (HL-LHC [119]) and for experiments running at a future FCC-ee [120], LHeC/FCC-eh [121], and FCC-hh [119] are also shown. The vertical red line shows the allowed range of couplings of a new gauge boson X to electrons that could explain the ^{8}Be anomaly [122, 123]. The existing limits are shown as grey areas. The bottom plot is revised from [124]. Figure taken from [90].

Therefore, the search for Higgs boson exotic decays, as those just shown, presents a good opportunity for BSM physics and provides an interesting window into dark matter.

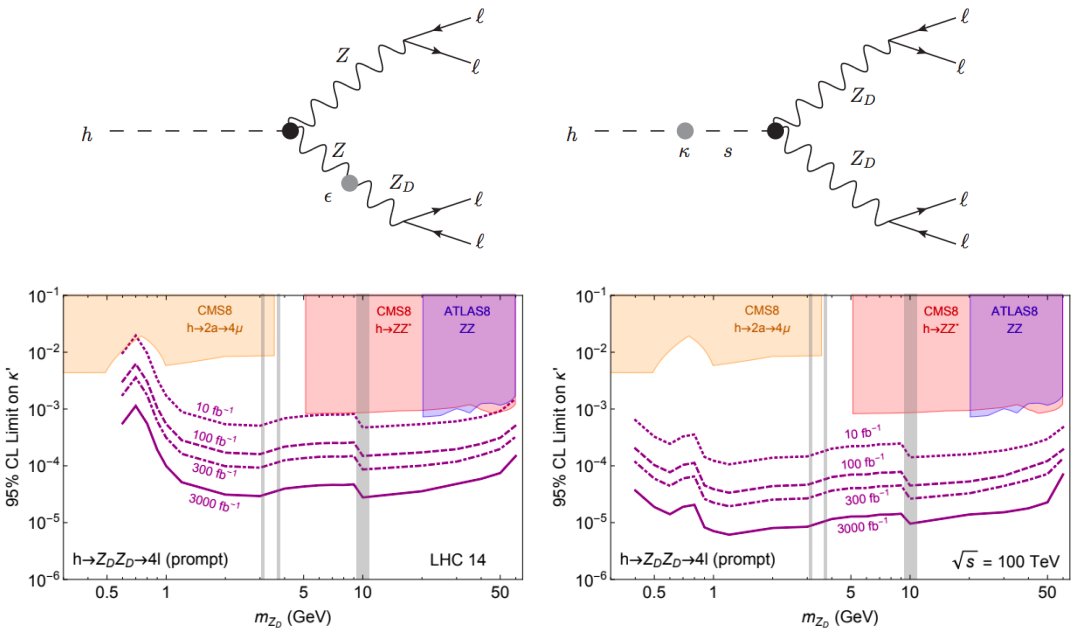

Figure 1.14: Exotic Higgs decays to four leptons induced by intermediate dark photons in the higgsed dark U(1) model. Top left: $h \to Z_D Z^* \to 4$ leptons via the hypercharge portal. Top right: $h \to Z_D Z_D \to 4$ leptons via the Higgs portal. Bottom: Expected 95% CLs limits on the effective Higgs mixing parameter κ' at the LHC (left) and a 100 TeV pp collider (right). Gray bands correspond to regions where quarkonium background (J/ψ, $\psi(2S)$, and Υ) may invalidate the analysis. The limits obtained during Run 1 are shown in red and blue shaded regions for the CMS [125] and ATLAS [126] experiment, respectively. In orange the limit from the CMS 8 TeV $h \to 2a \to 4\mu$ search [127]. Figure taken from [119].

Chapter 2

Theoretical implementation of the model

In this chapter, the extension of the Minimal Supersymmetric Standard Model Dark (dark-SUSY), with the addition of a dark Higgs boson, is described.

Moreover, the physics channel studied in this work is introduced.

Finally, the details of the model passed to the `FeynRules` tool are reported together with some considerations on the cross section.

2.1 Minimal Supersymmetric Standard Model Dark

The Minimal Supersymmetric Standard Model Dark (MSSMD), also known as dark-SUSY, is a vector portal dark sector that extends the MSSM by adding the gauge symmetry group $U(1)_D$ [128, 129, 130]. This is spontaneously broken giving rise to a light dark photon that mixes kinematically with the SM photon. The hidden sector communicates with the MSSM through

$$\mathscr{L}_{\text{mix}} = \frac{1}{2}\varepsilon A_D^{\mu\nu} B_{\mu\nu},$$

where ε is the kinetic mixing parameter, $A_D^{\mu\nu}$ and $B_{\mu\nu}$ the field strength of $U(1)_D$ and $U(1)_Y$ respectively.

A search has been done using a data sample of proton-proton collisions acquired by the CMS experiment at a center-of-mass energy of 13 TeV [142]. This looked for a Higgs boson that decays to two n_1, the lightest MSSM neutralino. Both of them then decay via $n_1 \to n_D + \gamma_D$ with n_D the dark neutralino that is undetected and γ_D the dark photon. Finally, this last decays in a pair of muons. The mass of n_1 was set to 10 GeV and the one of n_D to 1 GeV. Figure 2.1 shows the 90% CL upper limits on the Higgs boson production cross section and branching ratio in the two-dimensional plane ε and m_{γ_D}. The value for the branching ratio $\mathcal{B}(h \to 2\gamma_D + X)$

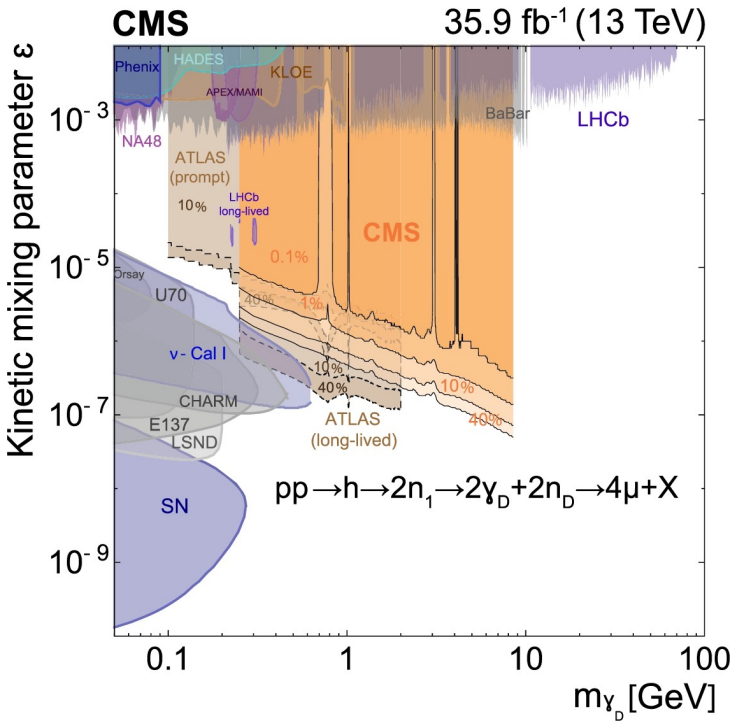

Figure 2.1: The 90% CL upper limits (black solid curves) from dark-SUSY search. The limits are presented in the plane of the parameters (ε and m_{γ_D}). Constraints from other experiments [80, 92, 93, 96, 103, 104, 131, 132, 133, 134, 135, 136, 137, 138, 139, 140, 141] showing their 90% CL exclusion contours are also presented. Figure taken from [142].

ranges from 0.1 to 40% with the last one given just for comparison since it has been excluded from results in Ref. [143]. The mass of the dark photon investigated goes from 0.25 to 8.5 GeV. The kinetic mixing parameter is related to the lifetime (see Section 2.2.2) which varies from 0 to 100 mm. These results improve those in Ref. [144] by a factor of approximately 2.5.

2.2 Extension of the MSSMD

The simplest way to generate dark photon mass is through a dark Higgs mechanism [145]. Thus a self-consistent hidden sector contains a massive photon γ_d, three hidden neutralinos n_d^i, which are a mixture of hidden gauginos and higgsinos, two CP-even scalars h_d and H_d, and a CP-odd scalar a_d [128].

Figure 2.2 shows the decay modes associated with these dark bosons. The channel studied in this work is a neutralino pair production event with the neutralino ultimately decaying in the dark sector and, in particular, to a dark Higgs

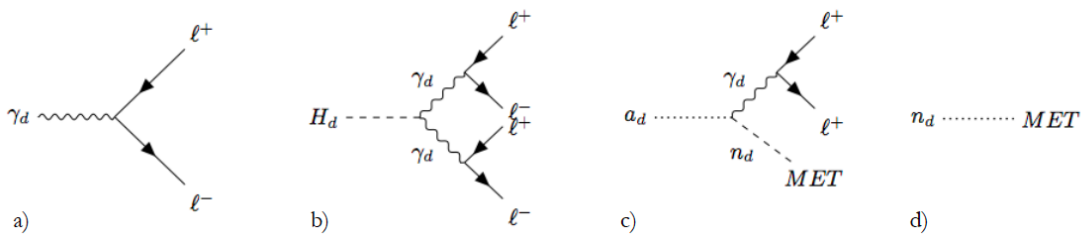

Figure 2.2: The different decay modes associated with the dark bosons: a) γ_d direct decay into leptons through kinetic mixing; b) H_d decays into two on-shell γ_d which then decay into two leptons each; c) a_d decays into n_d and dileptons through an on-shell or off-shell dark vector-boson depending on the detailed spectrum; d) n_d if lighter than the other bosons typically decays outside the detector and constitutes missing energy. Figure taken from [146].

and a dark neutralino that escapes the detector. Each dark Higgs decays in two dark photons (as in Fig. 2.2 b) and each of these last in a pair of muons (as in Fig. 2.2 a). The entire process is depicted in Figure 2.3. Therefore, the expected signature consists of four muon pairs and missing energy. The CP-even H_d has to be added to the MSSMD.

2.2.1 Implementation of the model

To use the extended dark-SUSY model in event generators, it has to be first implemented in `FeynRules`. `FeynRules` is a `Mathematica` [147] package that allows for the calculation of Feynman rules in momentum space for any quantum field theory physics model [148]. The user provides the package with minimal information through a model file. Starting from the one for the MSSMD[1], all the details needed for the implementation have been added. The $U(1)_D$ is defined as an Abelian group with coupling constant g_d fixed as default to 0.1:

$$\texttt{gd} := \{\text{ParameterType} \to \texttt{External}\ ,\ \text{ComplexParameter} \to \texttt{False},\ \text{Value} \to \texttt{0.1},\ \text{InteractionOrder} \to \texttt{\{DV,1\}}\}.$$

Since only the leading-order (LO) matrix element is considered, the interaction order is set to 1.

The maximum value to be allowed in the entire diagram for the power of the coupling is

$$\text{InteractionOrderLimit} = \texttt{\{DV,8\}}.$$

[1] `https://feynrules.irmp.ucl.ac.be/wiki/MSSMD`

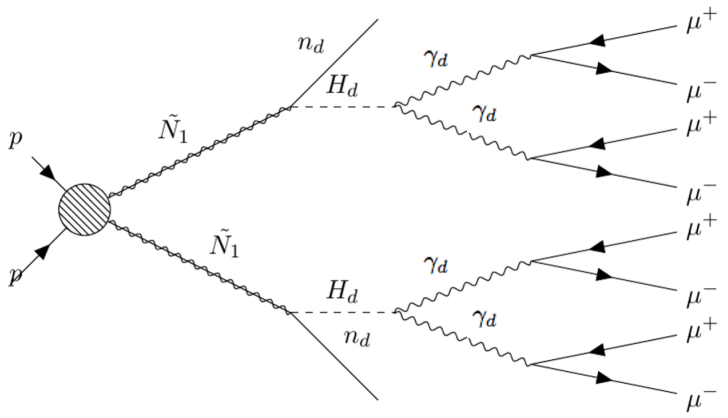

Figure 2.3: Feynman diagram of the dark-SUSY channel analysed in this thesis for an hadron collider.

in fact, there is one g_d factor from the vertex $\widetilde{N}_1 \to H_d + n_d$, one for $H_d \to \gamma_d\gamma_d$ and two for each $\gamma_d \to \mu^+\mu^-$, for a total of four Then, they have to be doubled because the event is a neutralino pair production.

The desired hierarchy coupling is set as:

$$\text{InteractionOrderHierarchy} = \texttt{\{QCD, 1\}, \{DV, 2\}, \{QED, 2\}}$$

which means that a power of g_d is considered equivalent to g_s^2.

Since the physics field for the vector dark photon and the fermionic dark neutralino were already defined as

$$\begin{aligned}\texttt{V[5]} :=\{&\text{ClassName} \to \texttt{AD}\ , \text{SelfConjugate} \to \texttt{True}, \text{Mass} \to \texttt{MAD},\\ &\text{Width} \to \texttt{WAD}, \text{ParticleName} \to \texttt{"ad"}, \text{PDG} \to \texttt{3000022},\\ &\text{PropagatorLabel} \to \texttt{"AD"}, \text{PropagatorType} \to \texttt{Sine},\\ &\text{PropagatorArrow} \to \texttt{None}\}\end{aligned}$$

and

$$\begin{aligned}\texttt{F[8]} :=\{&\text{ClassName} \to \texttt{neuD}\ , \text{SelfConjugate} \to \texttt{True}, \text{Mass} \to \texttt{MneuD},\\ &\text{Width} \to \texttt{WneuD}, \text{ParticleName} \to \texttt{"nD"}, \text{PDG} \to \texttt{3000001},\\ &\text{PropagatorLabel} \to \texttt{"neuD"}, \text{PropagatorType} \to \texttt{Straight},\\ &\text{PropagatorArrow} \to \texttt{None}\}\end{aligned}$$

only the scalar field for the dark Higgs boson has to be added:

```
S[11] :={ClassName → Hdark , SelfConjugate → True, Mass → MHd,
         Width → WHd, ParticleName → "Hdark", PDG → 3000025,
         PropagatorLabel → "Hdark", PropagatorType → ScalarDash,
         PropagatorArrow → None}
```

The self-conjugate flag set to `True` indicates that it is equivalent to its antiparticle. The mass and the width are variables to be set in the event generator. The propagator type suggests that it propagates as a scalar boson with spin 0.

The user has finally to write the different terms of the Lagrangian. The coefficients have been adapted from Ref. [149]. For the decay of the MSSM neutralino in the dark Higgs and dark neutralino, the Lagrangian is:

$$\mathscr{L}_1 := \varepsilon' \frac{e}{2\cos\theta_w} \overline{N}_1 n_d H_d.$$

Similarly, for the decay into a dark photon and neutralino, it is:

$$\mathscr{L}_2 := \varepsilon' \frac{-ie}{2\sin\theta_w \cos\theta_w} \left(\overline{N}_1 \gamma^\nu n_d\right) \cdot A_{d\nu}$$

where A_d is used instead of γ_d for the dark photon to avoid confusion with Dirac matrices (γ^ν).

The Lagrangian density for the Higgs dark decaying into two dark photons is:

$$\mathscr{L}_3 := 2v\mathcal{M} H_d A_{d\nu} A_d^\nu \tag{2.1}$$

with a coefficient $\mathcal{M}$ proportional to the dark photon mass squared.

For the decay of the dark photon into two muons, it holds:

$$\mathscr{L}_4 := \varepsilon e \left(\overline{\mu}\gamma_\nu \mu\right) \cdot A_d^\nu.$$

The total Lagrangian is the sum of the one of MSSM with the addition of these four terms. Based on this information, `FeynRules` calculates the Feynman rules and provides the model in UFO (Universal FeynRules Output) format to be imported into the event generator chosen.

2.2.2 Evaluation of the cross section

Each physics process is characterised by a cross section that represents the probability to happen as will be discussed in Section 3.1. In the case of the channel reported in Figure 2.3, the total cross section is:

$$\sigma(pp \to \widetilde{N}_1\widetilde{N}_1) \times \mathcal{B}^2(\widetilde{N}_1 \to n_d H_d) \times \mathcal{B}^2(H_d \to \gamma_d\gamma_d) \times \mathcal{B}^4(\gamma_d \to \mu^+\mu^-) \tag{2.2}$$

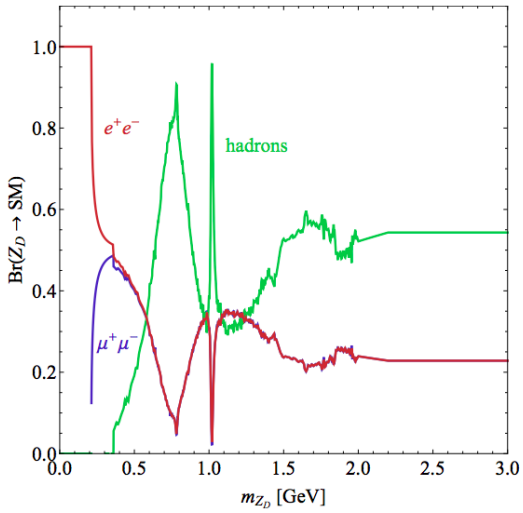

Figure 2.4: Branching ratios for dark photon decay with masses below 3 GeV [150].

where $\mathcal{B}$ is the branching ratio for the specific decay that has to be powered to the number of times it appears in the process.

Starting from the end, the dark photon decays to SM leptons with a partial width given by:

$$\Gamma(\gamma_d \to l^+ l^-) = \frac{1}{3}\alpha\varepsilon^2 m_{\gamma_d}\sqrt{1-\frac{4m_l^2}{m_{\gamma_d}^2}}\left(1+\frac{2m_l^2}{m_{\gamma_d}^2}\right), \tag{2.3}$$

where ε is the already introduced kinetic mixing parameter. The $\Gamma(\gamma_d \to \text{hadrons})$ is also proportional to ε^2 [90]. Therefore, the partial width dependence on ε^2 can be factorised

$$\left(\frac{\Gamma}{\varepsilon^2}\right)^{-1} = f(m_{a_d}),$$

and the branching ratio of the dark photon in muons

$$\mathcal{B}(\gamma_d \to \mu^+\mu^-) = \frac{\Gamma(\gamma_d \to \mu^+\mu^-)}{\Gamma_{\text{total}}} \tag{2.4}$$

results independent of ε^2. The kinetic mixing parameter has to be taken into account again when the lifetime is evaluated:

$$\tau_{\gamma_d} = \frac{\hbar}{\Gamma_{\text{total}}} = \frac{1}{\varepsilon^2} \times f(m_{a_d}).$$

Some values of the partial width and the branching ratio have been computed[2] for the model presented at the end of Chapter 1 and have been used to check the results of this work[3]. The leptons considered are just electrons and muons so the values of $\mathcal{B}(\gamma_d \to \mu^+\mu^-)$ are the ones in the table on the website divided by 2. Figure 2.4 shows the branching ratio, for masses of the dark photon above 2 GeV it is around 1/4 both for muons and electrons.

The branching ratio $\mathcal{B}(H_d \to \gamma_d\gamma_d)$ is supposed equal to 1 and the same holds for the branching ratio of the MSSM neutralino in a dark Higgs and a dark neutralino. Thus, the neutralino can only decay in this channel. A more general discussion can be found in Ref. [130, 151].

Therefore, the total cross section in Eq. (2.2) is simply:

$$\sigma(pp \to \widetilde{N}_1\widetilde{N}_1) \times \mathcal{B}^4(\gamma_d \to \mu^+\mu^-). \tag{2.5}$$

Finally, the production cross section of a pair of neutralinos has to be computed. The event generator `MadGraph5` [152] has been used to evaluate it in the case of proton-proton collisions for different masses of $\widetilde{N}_1$ at a center-of-mass energy of 13 TeV. The mass choice (10 GeV) of the previous analysis at the CMS experiment, described at the beginning of this chapter, has been rejected because excluded by the results of LEP [153]. Values above 60 GeV have been taken into account. From Figure 2.5 on the left it is evident that the smaller the mass is, the higher the cross section. In fact, if the neutralino is sufficiently light, the Higgs branching fraction into it is around 2.5% and therefore at around 60 GeV the neutralino pair is produced resonantly through an SM Higgs boson. Hence, for the analysis at the CMS experiment (see Part I of this work) the mass neutralino has been fixed to 60 GeV to ensure the higher cross section ($\sigma = 1.148$ pb). The wino soft-SUSY breaking mass M_2 is 191.5 GeV, the Higgs-higgsino mass parameter μ is 357.7 GeV and the tangent of the vacuum expected value of the two Higgs doublet fields ($\tan\beta$) is 9.75. The other MSSM parameters are reported in Appendix A for the sake of completeness.

[2] `http://insti.physics.sunysb.edu/~curtin/HiggsedDarkPhoton_BrTableData.txt`

[3] For example, from Eq.(2.3) for a dark photon mass (m_{γ_d}) of 20 GeV:

$$\frac{\Gamma(\gamma_d \to \mu^+\mu^-)}{\varepsilon^2} = 0.049\,\text{GeV}$$

and similar for $\Gamma(a_d \to e^+e^-)$.

The total width is 0.365, according to the second column of the table, and therefore from Eq.(2.4):

$$\mathcal{B}(\gamma_d \to l^+l^-) = \frac{0.049 \times 2}{0.365} = 0.268$$

In the table at the link in the previous note there is 0.286, which is consistent.

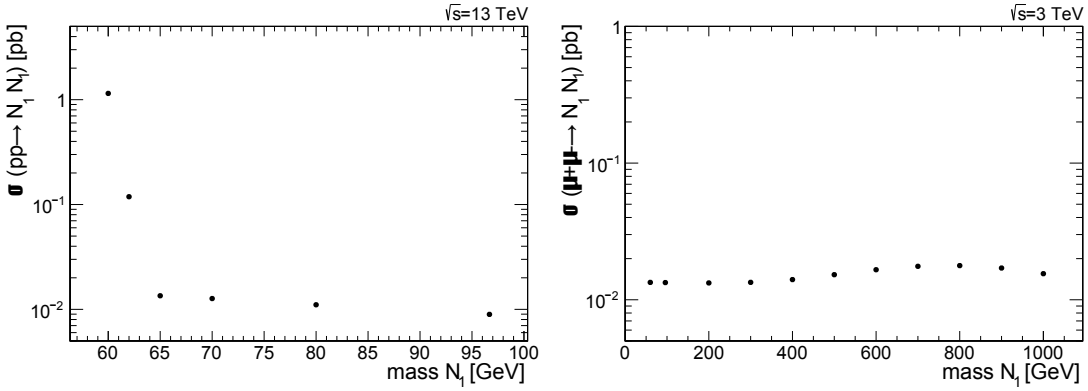

Figure 2.5: Simulated production cross section of neutralino pairs at a 13 TeV center-of-mass energy proton collider (left) and at a 3 TeV center-of-mass energy muon collider (right).

In the case of a muon collider, it has been shown that at a multi-TeV center-of-mass energy the dominant production mode is through vector boson fusion (VBF) [154]. Figure 2.6 depicts the case of WW fusion for neutralino pair production with muon neutrinos. On the right, the cross section via VBF is compared with s-channel annihilation for different neutralino masses and collision energies. For low masses (0.4-0.8 TeV) the VBF becomes dominant at $\sqrt{s} = 3-4$ TeV, while for $\mathcal{O}$(TeV) at $\sqrt{s} = 7 - 13$ TeV. In absence of neutrinos, on the other hand, the neutralino pair production cross section has been evaluated with `MadGraph5`. The results are shown on the right of Figure 2.5: the curve is quite flat over a large $\widetilde{N}_1$ mass range. For the predictions in Part II of this work, the mass has been set to 96.68 GeV, which is the default value in MSSM (see Appendix A).

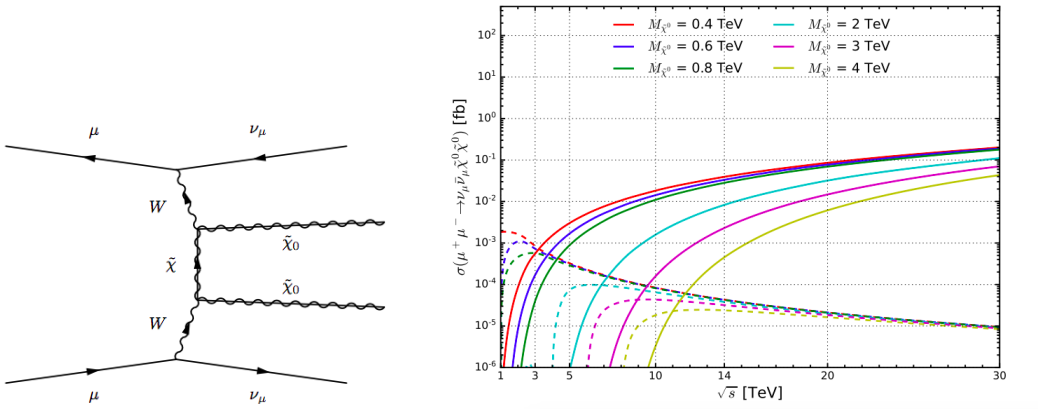

Figure 2.6: Left: Diagrammatic representation of neutralino pair production through WW fusion. Right: production cross section via s-channel annihilation (dashed lines) and VBF (solid lines) in $\mu^+\mu^-$ collisions as a function of collider energy for representative neutralino mass. Figure taken from [154].

Part I

Search at the CMS experiment

Chapter 3

The experimental apparatus: the Compact Muon Solenoid

The Compact Muon Solenoid is one of the four main experiments at the Large Hadron Collider, which discovered the Higgs boson and will likely have access to rare phenomena both included in the SM and beyond it.

This chapter furnishes details of the machine and the future planned increase of luminosity. All the detector subsystems are briefly described together with information on the reconstruction and identification of physics objects performed with the particle-flow algorithm. In the end, the reprocessing of raw data is schematised.

3.1 The Large Hadron Collider

The Large Hadron Collider (LHC), with its $\sim 27\,\text{km}$ circumference and $14\,\text{TeV}$ nominal center-of-mass energy, is the largest and most powerful particle accelerator in the world. It was approved by the CERN (*Conseil Européen pour la Recherche Nucléaire*) Council at the end of 1994 and built from 1998 to 2008, aiming at the discovery of the Higgs boson and the study of rare events [155].

The choice of a proton-proton (pp) machine was dictated by three main reasons. First of all, hadrons consent to reach higher center-of-mass energy with respect to electrons because of the low synchrotron radiation. Then, since protons are not elementary particles and the center-of-mass energy is distributed among the partons (gluons and quarks), a wider range of energies may be explored with fixed-energy beams. Finally, proton beams allow obtaining a higher luminosity compared to antiprotons. Thus, the two crucial features of the LHC are the energy available at the center-of-mass and the luminosity (other parameters are reported

Table 3.1: Nominal parameters of the LHC [155].

Parameters	
Beams	pp
Circumference	26.66 km
Centre-of-mass energy	14 TeV
Number of bunches	2808
Protons per bunch	10^{11}
Bunch crossing	25 ns
Luminosity	$1 \times 10^{34}\,\mathrm{cm^{-2}s^{-1}}$

in Table 3.1).

For the first one, a nominal value of $\sqrt{s} = 14\,\mathrm{TeV}$ was selected to study physics at the TeV scale. In fact, since only a fraction x of the proton energy is carried by partons, the mass of the particles produced in the collisions is less than the $\sqrt{s}$:

$$\sqrt{s'} = \sqrt{s x_1 x_2}. \tag{3.1}$$

A complex acceleration chain, consisting of one linear accelerator and three circular, is used to achieve this energy. The LINAC2 generates 50 MeV protons that enter the Proton Synchrotron Booster (PSB) and are accelerated up to 1.4 GeV. Then in the Proton Synchrotron (PS) energy of 26 GeV is reached and proton bunches are formed with a spacing of 25 ns. Finally, bunches are accelerated by Super Proton Synchrotron (SPS) up to 450 GeV and injected into the LHC ring in two parallel beam pipes with opposite directions.

The instantaneous luminosity ($\mathcal{L}$) for two equal Gaussian beams colliding head-on, usually measured in $\mathrm{cm^{-2}s^{-1}}$, can be calculated as:

$$\mathcal{L} = N_p^2 n_b \frac{\gamma}{4\pi\epsilon_n\beta^*} f_{rev} F \qquad F = 1/\sqrt{1 + \frac{\theta_c \sigma_z}{\sigma}}$$

with

N_p	number of protons per bunch	n_b	number of bunches per colliding beam
ϵ_n	transverse normalised emittance	γ	Lorentz factor
β^*	betatron function at interaction point	f_{rev}	revolution frequency
F	luminosity geometrical reduction factor	σ	transverse r.m.s. size
θ_c	full crossing angle between beams	σ_z	longitudinal r.m.s. size.

The interaction rate, i.e. the number of events detected per second, is given by:

$$R = \frac{dN}{dt} = \mathcal{L}\sigma,$$

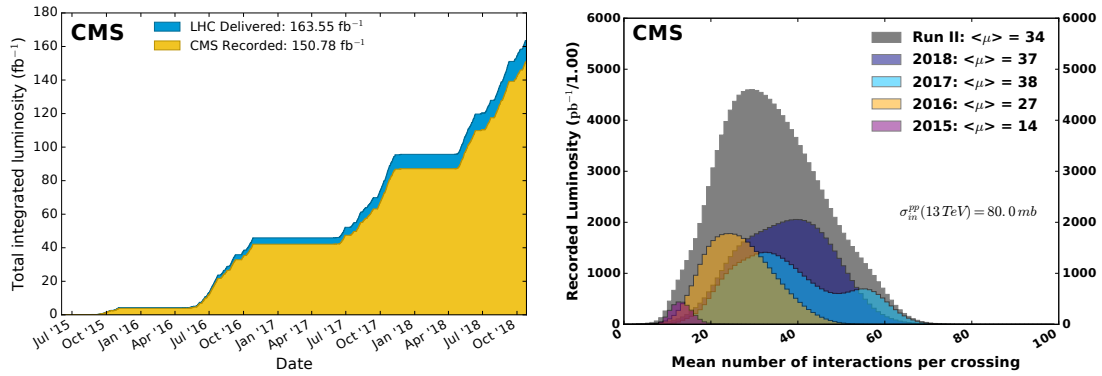

Figure 3.1: Left: Integrated delivered and CMS recorded luminosity cumulative over all years of Run 2 during stable beams for pp collisions at nominal center-of-mass energy ($\sqrt{s} = 13\,\text{TeV}$). Right: Distribution of the average number of interactions per crossing (pileup) for pp collisions including only Run 2 data. The overall mean values ($\langle\mu\rangle$) and the minimum bias cross section are also shown [156].

where σ is the cross section. The cross section is proportional to the probability that a specific process will take place, it has the dimensions of an area, and is measured in barn ($1\,\text{b} \equiv 10^{-24}\,\text{cm}^2$). Given the integrated luminosity, usually in fb^{-1}, during a run period:

$$\mathcal{L}_{int} = \int_0^T \mathcal{L} dt,$$

the total number of interactions is:

$$N = \mathcal{L}_{int}\sigma.$$

During the so-called *Run 2* from 2015 to 2018, the LHC reached and exceeded the designed luminosity $\mathcal{L} = 10^{34}\,\text{cm}^{-2}\text{s}^{-1}$, delivering an integrated luminosity of $163.55\,\text{fb}^{-1}$, as shown in Figure 3.1 left.

Each of the 2808 bunches circulating in the LHC ring contains $\mathcal{O}(10^{11})$ protons. They collide every 25 ns giving several simultaneous proton-proton collisions in the same bunch crossing. This effect is known as *pileup*. Figure 3.1 right reports the distribution of the pileup for Run 2 data with the mean values.

Four experiments are located at the points where the collision between the beams takes place. ATLAS (A Toroidal LHC ApparatuS) and CMS (Compact Muon Solenoid) are general-purpose, they have been designed to investigate a wide range of scenarios from the Higgs boson properties to new physics at the TeV scale. The latter will be described in detail in Section 3.2. LHCb (Large Hadron

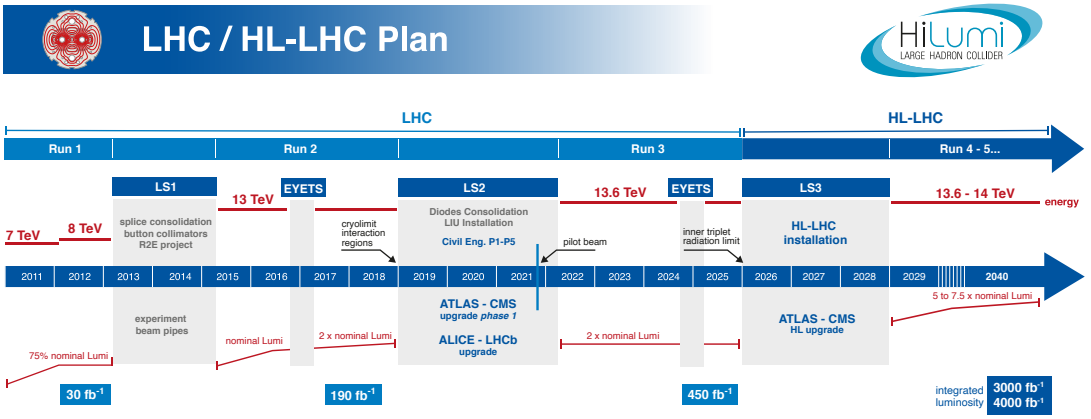

Figure 3.2: Schedule of the LHC and HL-LHC operations [157].

Collider beauty) is focusing on the physics of the hadrons containing a bottom quark, studying for example the CP -violation in this sector. ALICE (A Large Ion Collider Experiment) exploits heavy ion collisions (Pb-Pb) to understand the so-called *quark-gluon plasma*, i.e. strongly interacting matter at extreme energy densities.

3.1.1 High-Luminosity LHC

After the discovery of the Higgs boson by the ATLAS and the CMS experiment, on the 30th May 2013, the CERN Council approved the new European Strategy for Particle Physics, identifying the HL-LHC project as the top priority. Figure 3.2 shows the schedule for the operations. There are alternating periods of data taking, called *runs*, and long shutdowns. The LHC is now in Run 3 with a center-of-mass energy of 13.6 TeV and a luminosity of $2 \times 10^{34}\,\mathrm{cm}^{-2}\mathrm{s}^{-1}$, which was already reached in 2018 by reducing the betatron function β^* from 55 cm to 30 cm.

The HL-LHC project will start in 2026 to sustain and extend the LHC physics discovery potential, investigating deeply the properties of the Higgs boson such as the self -coupling, looking for additional bosons with exotic decays, improving measurements for the top quark and in the EW sector, and searching for SUSY particles.

The technical goal is to run at the nominal center-of-mass energy $\sqrt{\sigma} = 14\,\mathrm{TeV}$ increasing the peak luminosity up to $5 \times 10^{34}\,\mathrm{cm}^{-2}\mathrm{s}^{-1}$ (or even $7.5 \times 10^{34}\,\mathrm{cm}^{-2}\mathrm{s}^{-1}$) to achieve $3000\,\mathrm{fb}^{-1}$ ($4000\,\mathrm{fb}^{-1}$) of integrated luminosity in about twelve years of operations. The expected pileup is $\langle\mu\rangle = 140$. The HL-LHC project foresees the LHC injector upgrade program and the upgrade of all the experiments in order to handle the higher particle rates expected [158]. This is scheduled for the Long

Shutdown 3 (LS3) and is referred to as Phase-2 upgrade.

3.2 The Compact Muon Solenoid experiment

The Compact Muon Solenoid (CMS) apparatus is one of the two general-purpose experiments of the LHC. It consists of a cylindrical barrel and two endcap disks to ensure a 4π coverage for particle detection. As the name suggests, it is quite compact, only 14.6 m high and 21.6 m long, it was especially designed to detect muons and the main feature is the 3.8 T magnetic field provided by the solenoid. The superconducting magnet is 12.5 m long with an inner diameter of 6 m and a 1.5 m thick iron yoke. It weighs around 12 000 tons. Figure 3.3 shows the detector with the reference to all the subsystems. Following the traditional onion scheme, moving from the interaction point (IP) outward, there are:

1. the tracking system to build the trajectory of charged particles and reconstruct vertices,
2. the calorimeters to measure electrons, photons and hadrons energy,
3. the muon spectrometer to detect muons.

The first two are inside the magnetic coil, the third is in the gaps of the return yoke. Further information about the experiment can be found in Refs. [159, 160].

Before describing the subdetectors in detail, the coordinates adopted by CMS are briefly explained (see Figure 3.4). The origin of the right-handed system is the IP.
The x-axis points toward the center of the LHC ring while the y-axis upwards. The z-axis is parallel to the beampipe and directed to the Jura mountain. Polar coordinates are used: the radial distance $r = \sqrt{x^2 + y^2}$, the azimuthal angle with respect to y-axis ϕ, and the polar angle θ from the z-axis.

Two useful quantities are the transverse momentum of a particle:

$$p_T = p \sin\theta$$

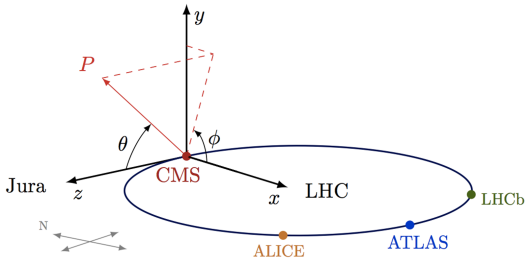

Figure 3.4: CMS coordinate system.

with p the momentum modulus, and the pseudorapidity:

$$\eta = -\ln\left[\tan\frac{\theta}{2}\right]$$

which provides information about the angle between the particle and the beam axis. It is equal to zero at $\theta = 90°$ and tends to infinity at $\theta = 0°$.

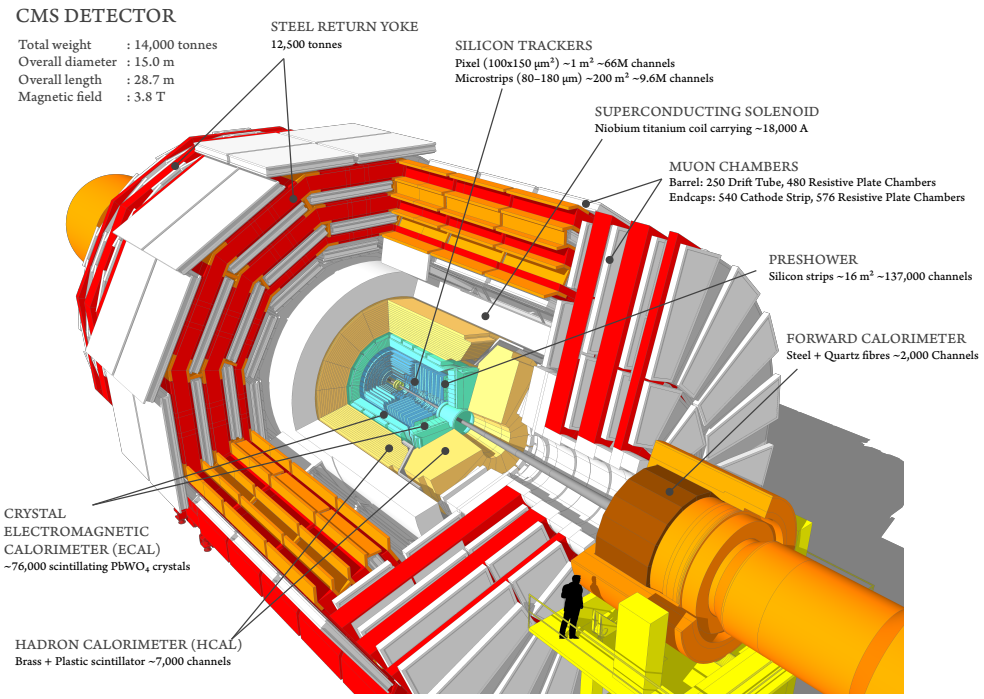

Figure 3.3: Cutaway diagram of the CMS detector for Run 2 [161].

3.2.1 The inner tracker

The tracker is the closest detector to the IP, deputed to the measurement of the trajectory of each charged particle and the reconstruction of vertices. It has a total length of 5.8 m and a diameter of 2.5 m, and it covers the region up to $|\eta| \approx 2.5$. It is inside the 3.8 T magnetic field that bends the particles in the transverse plane, allowing for the derivation of the momentum from the radius of curvature R:

$$p_T[\text{GeV}] = 0.3B[\text{T}]R[\text{m}]. \tag{3.2}$$

The inner part of the tracker is the pixel detector. In the original design, there were three layers of pixels in the barrel (TPB) and two disks in both endcaps (TPE). During the Extended Year-End Technical Stop (EYETS) in 2016, a layer was added both in TPB and TPE to cope with the increase in luminosity. This upgrade is known as Phase-1. The pixels size is $100 \times 150\,\mu\text{m}^2$ and the endcap disks are arranged in a turbine-like geometry, i.e. with blades 20° rotated one with respect to the other, to benefit from the large Lorentz angle. This ensures a spatial resolution of $\sim 10\,\mu\text{m}$ in the $r - \phi$ plane and $\sim 20 - 40\,\mu\text{m}$ in the longitudinal plane. The pixel detector provides p_T and impact parameter measurements, particle identification (b- and t-jets), and vertex reconstruction.

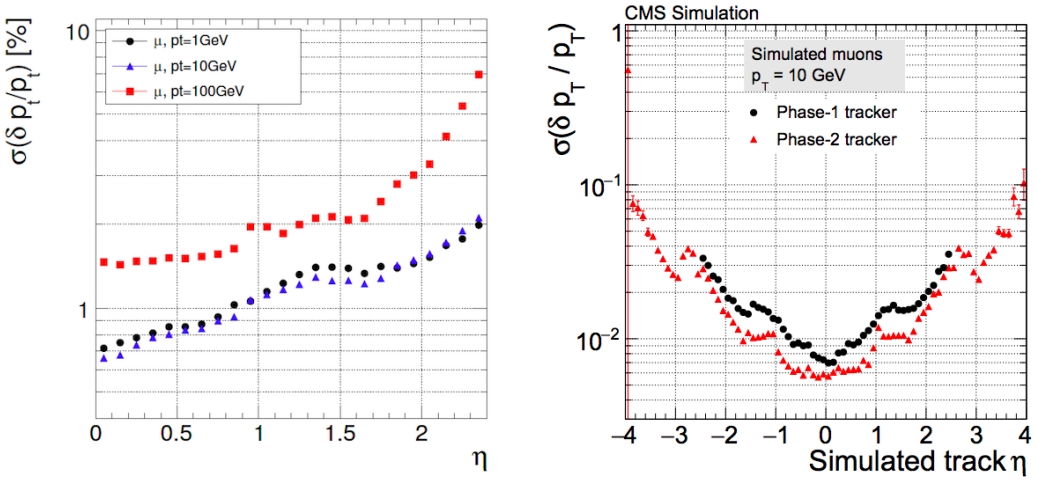

Figure 3.5: Left: Transverse momentum resolution for single muons with transverse momenta of 1, 10 and 100 GeV [160]. Right: Relative resolution of the transverse momentum as a function of the pseudorapidity for the Phase-1 (black dots) and the upgraded (red triangles) tracker, using single isolated muons with a transverse momentum of 10 GeV [163].

The silicon strip detector surrounds the pixel one and is made of microstrip sensors with $80-180\,\mu m$ pitch distributed in 4 layers in the inner barrel (TIB) and 6 in the outer barrel (TOB), 3 disks in the inner endcap (TID) and 9 in the outer endcap (TEC). Some modules, called *stereo modules*, are mounted back-to-back at an angle of 100 mrad to measure the coordinate orthogonal to the strip. The spatial resolution of the silicon microstrips is very different from one module to the other. This system provides momentum and energy measurements. Further technical details are reported in Figure 3.3 and Ref. [162].

Figure 3.5 left shows the transverse momentum resolution for single muons at different energies. For high momentum tracks (100 GeV) up to $|\eta| \approx 1.6$ it is around 1-2%. The performance will be discussed in Section 3.3.

During the LS3, in order to exploit the increase in luminosity of the HL-LHC, the entire silicon system (both pixels and strips) will be replaced to increase the forward acceptance up to $|\eta| \approx 3.8$, the radiation hardness and the granularity [163]. In general, an improvement in performance is expected. For example, the simulation of the p_T resolution with the new detector is compared with the present one in Figure 3.5 right.

3.2.2 The calorimeters

Calorimetry is the measurement of the energy deposited in a medium. Two systems are installed in CMS: the inner one, the electromagnetic calorimeter (ECAL), is designed for electrons and photons, and the outer one, the hadronic calorimeter (HCAL), for jets and missing transverse energy (MET).

The ECAL is a homogenous calorimeter made of lead tungstate ($PbWO_4$) crystals. The homogeneity guarantees a good energy resolution and thus the capability to detect the decay of the Higgs boson in two photons which is one of the main requirements. As for the tracker, it consists of two parts: the barrel (EB) covers the region up to $|\eta| < 1.48$, and the endcap (EE) extends up to $\eta \sim 3$. The $PbWO_4$ is characterised by a short radiation length[1] ($X_0 = 0.89\,\text{cm}$) and a small Molière radius[2] ($R_M = 2.2\,\text{cm}$), ensuring fine granularity and a compact calorimeter. The EB has $\sim 20 \times 20\,\text{mm}^2$ cells for a total length of 230 mm, corresponding to 25.8 X_0. The EE, instead, is 24.7 X_0 long and made of $\sim 30 \times 30\,\text{mm}^2$ crystals. The scintillation light produced by the crystals is detected by avalanche photodiodes (APDs) in the EB and vacuum phototriodes (VPCTs) in the EE. In the two endcaps, a preshower detector has been added to discriminate photons from π_0 decay and improve the direction's measurement. It is a two-layer sampling calorimeter made of a lead radiator that initiates the shower and a silicon strip detector for a total length of 3 X_0. Further technical details are available in Ref. [164]. The energy resolution can be written as:

$$\left(\frac{\sigma(E)}{E}\right)^2 = \left(\frac{S}{\sqrt{E}}\right)^2 + \left(\frac{N}{E}\right)^2 + C^2,$$

where S, the stochastic source, takes into account the fluctuations in the lateral shower containment and the photostatistics contribution, N represents the electronics, pileup and digitization noise, and C is a constant term that contains, for example, intercalibration errors. It was measured in a test beam with 20-250 GeV electrons giving $S = 2.8\%$, $N = 12\%$ and $C = 0.3\%$ [165]. The results are shown in Figure 3.6 left.

The HCAL is a sampling calorimeter devoted to the measurement of energy and direction of jets and of MET, which is crucial in the search for SUSY particles [166]. It consists of four subsystems: the hadron barrel (HB), the hadron endcap (HE), the HCAL outer (HO), and the HCAL forward (HF). The HB and HE covers the region up to $\eta = 3$, brass is used as absorber and plastic scintillators as active materials. The interaction length, i.e. the average distance a high-energy

[1] The radiation length is the mean distance over which the electron loses all but $1/e$ of its energy by *Bremsstrahlung*.

[2] The Molière radius is the radius of a cylinder that contains 90% of the shower energy deposition.

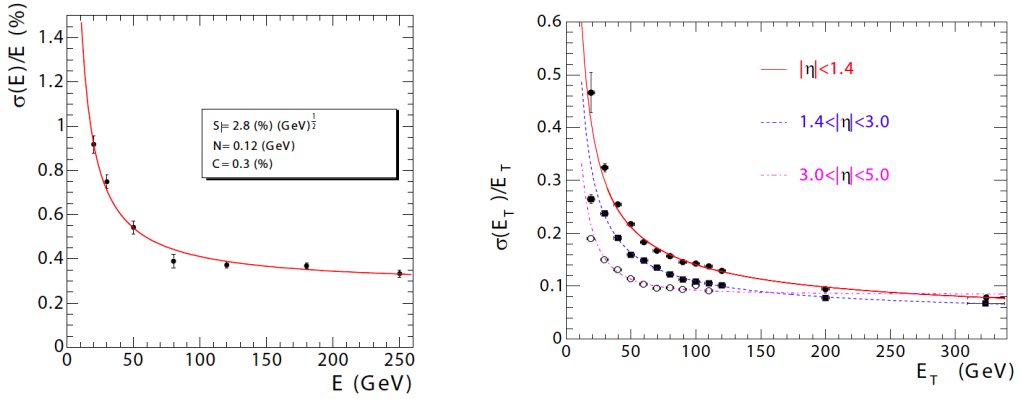

Figure 3.6: Left: Resolution as a function of the electron energy for CMS ECAL [165]. Right: The jet transverse-energy resolution as a function of the jet transverse energy for barrel jets (red), endcap jets (blue), and very forward jets (violet) [160].

hadron has to travel inside the material before a nuclear interaction occurs, varies from 5.8 to 10.6 λ_I depending on the pseudorapidity. During the Phase-I upgrade, the HB and HE photodetectors were upgraded by exploiting SiPM (Silicon Photo-Multipliers) instead of Hybrid Photodiode. The HO is placed outside the magnetic coil; it uses the same scintillators of the HB and HE and the steel return yoke of the solenoid ad active material. Finally, the HF is a Cherenkov calorimeter with steel and quarts fibers that covers up to $|\eta < 5.2$. The combined (ECAL+HCAL) calorimeter energy resolution was measured in a pion test beam [167] to be:

$$\frac{\sigma(E)}{E} = \frac{A}{\sqrt{E}} \oplus B$$

with $A = 84.7 \pm 1.6\%$ and $B = 7.4 \pm 0.8\%$. Figure 3.6 right shows the expected jet MET resolution in different η regions.

For the HL-LHC program, the EB will feature upgraded front-end electronics, while the EB and HB the replacement of the off-detector electronics [168]. The endcap of both ECAL and HCAL will be substituted by the High Granularity Calorimeter (HGCal), a sampling calorimeter that will provide highly-segmented spatial information in both transverse and longitudinal directions, as well as high-precision timing information [169].

3.2.3 The muon spectrometer

Muons do not interact strongly and therefore reach the most external system of the CMS apparatus, the muon spectrometer. It is especially designed for muon

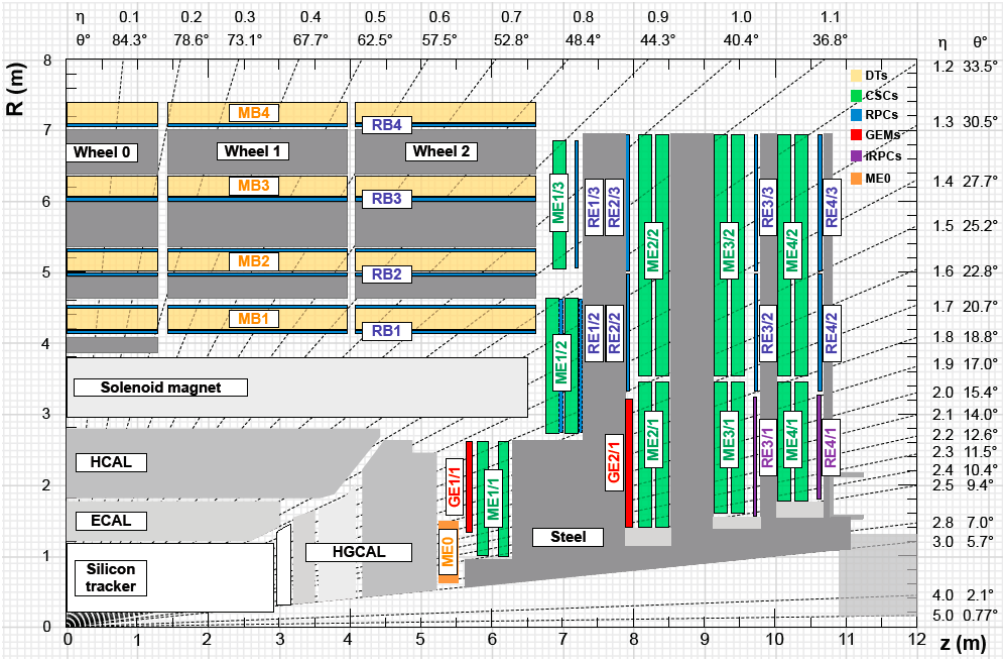

Figure 3.7: An R-z cross section of a quadrant of the CMS detector, including the Phase-2 upgrades (RE3/1, RE4/1, GE1/1, GE2/1, and ME0). The acronym iRPCs in the legend refers to the new improved RPC chambers RE3/1 and RE4/1. The interaction point is at the lower left corner. M denotes Muon, B stands for Barrel and E for Endcap. The magnet yoke is represented by the dark grey areas [170].

identification, transverse momentum measurement together with the inner tracker, and triggering. As the name suggests, the CMS experiment invests a lot of effort in the reconstruction of muons which are the signature of many interesting physics channels such as the Higgs golden channel $H \to ZZ \to 4\mu$ or the rare $B_s^0 \to \mu\mu$. Because of the large area to be covered, the system is equipped with gaseous detector stations interleaved with the magnet return yoke.

A longitudinal view of a quarter of the muon system is shown in Figure 3.7. Originally, Drift Tubes (DT) and Cathode Strip Chambers (CSC) were selected for the barrel ($|\eta| < 1.2$) and endcap region respectively ($0.9 < |\eta| < 2.4$) together with Resistive Plate Chambers (RPC) [171]. These last ensure a fast response, while DT and CSC were chosen for their excellent spatial resolution $\mathcal{O}(100\,\mu\text{m})$. Three stations (ME4/2 RE4/2 and RE4/3) were added in the endcap during LS1 and one (GE1/1) during LS2. This last was equipped with Gaseous Electron Multiplier (GEM) detectors.

As far as the performance is concerned, Figure 3.8 shows the p_T resolution for the muon system for two different η regions. Without the tracker, the resolution

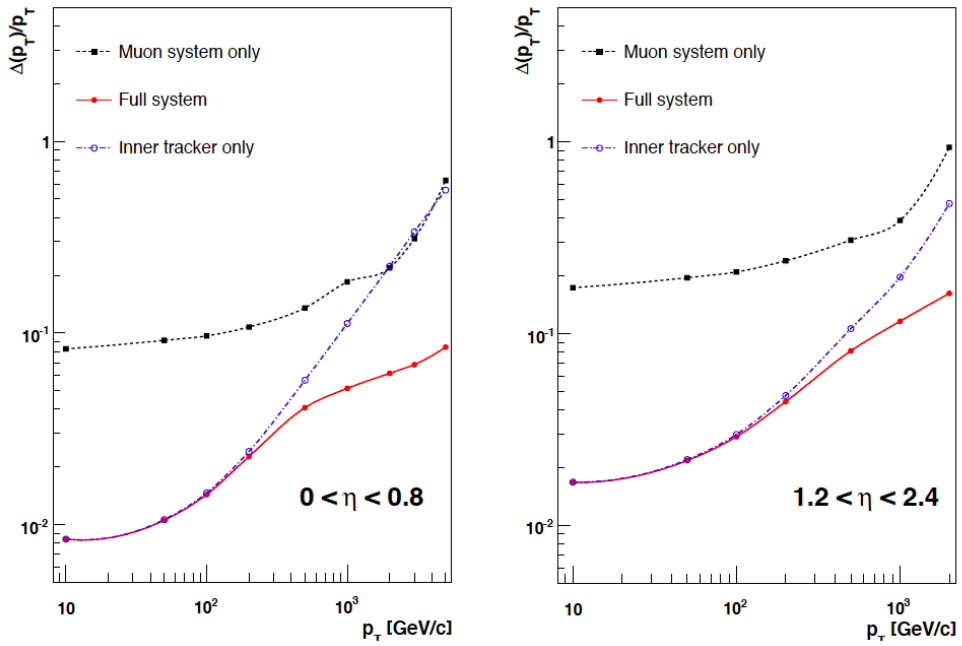

Figure 3.8: The muon transverse momentum resolution as a function of the transverse momentum using the muon system alone, the inner tracking alone, and both [160].

is $\sim 20\%$ for $p_T < 200\,\text{GeV}$ and $|\eta| < 2.4$, but the muon system becomes relevant in the reconstruction of high-energy muons at low η. The uncertainties at low momentum are dominated by multiple scattering.

As for all the others subsystems, an upgrade is foreseen to cope with the increase in luminosity. The DT and CSC front-end and backend electronics and the RPC backend electronics will be replaced. New GEM and RPC stations will be installed in the very forward region to extend coverage up to $|\eta| \sim 3$. Further details can be found in Ref. [170].

3.2.4 The trigger system

Because of the proton bunch crossing frequency of 40 MHz and the single collision event size of $\sim 1\,\text{MB}$, storing data is a crucial problem to be solved. A trigger is needed to reduce the number of events to a level that can be read out, stored and processed offline. The challenge is to reject $\sim 99.998\%$ of all the data keeping interesting events from energetic and hard pp collisions. To achieve this goal, CMS opted for a two-level system consisting of a Level 1 Trigger (L1) and High Level Trigger (HLT).

The L1 is purely hardware based and exploits custom-made (ASICs) and pro-

grammable logic (FPGAs) to reduce the rate from 40 MHz to 100 kHz [172]. It has a local buffer of 128 memory cells and therefore the latency, i.e. the time during which the raw data information must be stored awaiting for L1 trigger decision, is 3.2 µs. Because of this limit, up to now, L1 uses inputs only from calorimeters and muon system. Track reconstruction is indeed too slow. Energy deposits in ECAL and HCAL towers, and hits in DT, CSC and RPC are preprocessed into Trigger Primitives (TPs). Then, different TPs from the same event are processed in parallel until a Global Trigger merges information from the Global Calorimeter Trigger (GCT) and the Global Muon Trigger (GMT) and makes the final decision.

The HLT is an offline software trigger that receives full event information to reduce the rate to $\mathcal{O}(100\,\text{Hz})$ in $\sim 100\,\mu\text{s}$ [173]. It uses CPU farms with ~ 30 cores to run logical independent trigger paths in parallel. A trigger path is a chain of producers and filters. The first ones compute physics objects from the event information. The second ones decide to select or reject the event. If after HLT the rate is too high a prescale (P) is applied and only the fraction $1/P$ of events is stored.

The trigger system will also be upgraded to keep and improve performance in view of the HL-LHC program. The L1 rate and latency will be 750 kHz and 12.5 µs. This last will allow using also tracks from the strip outer tracker. Thus, the techniques of offline analysis, such as particle-flow (see Section 3.3), will become possible at L1 and will benefit enormously from HGCal. The expected HLT output is 7.5 kHz. Further details are presented in Refs. [174, 175].

3.3 Physics objects reconstruction and identification

The raw data from detectors, i.e. hits from the tracker and muon chambers and energy deposits in calorimeters, are stored and then the particle-flow (PF) algorithm reconstructs and identifies all the stable particles in the event through the combination of all subsystems [176]. LEP measurements of jet fragmentations proved that a typical jet has 62% of the energy transported by charged hadrons, 27% by photons, 10% by long-lived neutral hadrons (neutrons and K_L) and 1.5% by neutrinos [177]. Adopting a standard approach based on the sum of ECAL and HCAL energies' measurements, since approximately 72% of the energy comes from HCAL, the energy resolution is limited by the one of HCAL. PF, instead, reconstructs the four momenta of all visible particles using the information from the subdetector with the best accuracy, reaching a further better jet resolution. CMS is particularly suitable for PF thanks to the highly segmented tracker, the granular ECAL, the hermetic HCAL and the strong magnetic field. PF is based

on the so-called *fundamentals elements* and *blocks*. Muons are independent of PF, their reconstruction is described in detail in 3.3.1.

Fundamental elements

The fundamental elements are the charged particle tracks and the clusters that are reconstructed in the subdetectors independently.

Tracking is an iterative procedure [178] that aims to achieve high efficiency and low fake rate starting. Each iteration is fourfold:

1. seeding: all possible combinations of hits (called *seeds*) provide track candidates and give an initial estimate of trajectory parameters. At the first iteration, seeds are asked to be prompt and with high p_T. Then this very tight criterium is loosened;
2. pattern recognition based on Kalman Filter (KF) [179]: each track candidate is extrapolated to the external layers to look for hits and to update parameters. If no hit is found, the layer is skipped. If more than one hit is there, many tracks are created. Once the last layer is reached, the algorithm proceeds from the outside in to add hits that might be excluded;
3. final fitting: after combining all associated hits the best parameters of each smooth trajectory are estimated;
4. selection: tracks are selected according to a quality flag based on the χ^2 and compatibility with the interaction region.

After reconstruction, tracks are extrapolated backwards to find the vertex, i.e. the position of the pp interaction. Since in each bunch crossing there is more than one collision, many vertices are reconstructed. The primary one is selected according to the features of linked tracks (e.g. high p_T), and the others are pileup vertices.

Clustering aims to detect and measure the energy and direction of stable neutral particles, separate them from charged ones, and reconstruct and identify electrons and all accompanying *Bremsstrahlung* photons. It is performed separately in each subdetector: EE, EB, HB, HE, HO and the two layers of the preshower detector. For HF each cell gives rise to one cluster so no clustering is done. There are three steps:

1. seeds are local energy minima above given energy;
2. topological clusters start from the seeds aggregating cells with at least one side in common with a cell already in the cluster, and with energy exceeding a given threshold;
3. each PF cluster is corrected for energy loss.

Blocks and simple objects reconstruction

The PF fundamental elements plus muon tracks are associated in blocks through a link algorithm. Each pair of elements is tentatively associated, and the quality of the link is quantified by the link distance, i.e. the distance in (η, ϕ) plane. At this point the PF algorithm proceeds for each block as follows:

- muons are reconstructed from global muons (see Section 3.3.1);
- PF clusters in ECAL are grouped in superclusters that merge the energy associated to *Bremsstrahlung* photons and pairs. Each track in the block passes a pre-identification stage and is filtered with a Gaussian Sum Filter (GSF) that takes into account the sudden curvature change due to *Bremsstrahlung* emission [180]. The GSF track is finally associated with the supercluster and the PF electron is created;
- tracks with large uncertainties are removed, allowing to get rid of most of the fake ones;
- the remaining elements give rise, in order, to charged hadrons, photons and neutral hadrons.

A detailed description of the algorithm is reported in Ref. [176].

Complex objects reconstruction

The resulting list of PF reconstructed particles, without double counting, constitutes a global description of each event and is available for the reconstruction of more complex objects such as taus, jets and MET.

Jets are narrow cones of collimated particles produced from the fragmentation, called *hadronization*, of a parton. Quarks and gluons, in fact, can not be observed free due to QCD confinement. `FastJet` is a package that provides implementations of many sequential recombination algorithms to reconstruct jets [181]. All the PF objects are treated as pseudo-jets. Then, the distance of a PF object i and a pseudo-jet j is computed:

$$d_{ij} = \min(k_{ti}^{2n}, k_{tj}^{2n}) \frac{\Delta R_{ij}^2}{R^2}, \tag{3.3}$$

where k_t is the transverse momentum, $\Delta R_{ij} = \sqrt{(\phi_i - \phi_j)^2 + (\eta_i - \eta_j)^2}$ is the angular distance and R is the jet-radius parameter. This is compared with the distance of the PF object to the beam:

$$d_{ib} = k_{ti}^{2n}.$$

If $d_{ij} < d_{ib}$ i and j are combined in a new pseudo-jet, otherwise i is promoted to jet. This is repeated for all the pseudo-jets. CMS uses the anti-k_t algorithm with

$n = -1$ [182], meaning that PF candidates are clustered around the more energetic particle in the event. The parameter $R = 0.4$, apart for heavy particles ($R = 0.8$). The momentum of the jet is just the sum of all the particles that compose it and is considered equivalent to the momentum of the original parton.

Weakly interacting particles, such as neutrinos and dark matter candidates, are not detected at CMS. However, at the interaction point, the transverse energy of protons is null, and it has to be conserved. So the MET can be defined as the negative vector sum of p_T of all reconstructed PF candidates N in the event:

$$E_T^{\text{miss}} = -\sum_{i=1}^{N} \overrightarrow{p_{Ti}}.$$

Deservedly for these complex objects, the method called PUPPI (PileUp Per Particle Identification) has to be mentioned. This is a new technique that allows the removal of pileup contamination by employing a per-particle approach with improved results. PUPPI operates by using charged pileup to characterize the pileup in an event and assigns a weight to particles of unknown origin. This weight is used to rescale the particle's momentum. All the details are reported in Ref. [183].

3.3.1 Muon reconstruction

The CMS apparatus has been designed to detect and identify muons with high efficiency. Muons are reconstructed with a dedicated algorithm independent from PF, using information from the tracker and muon system. According to that, there are three different types of objects: standalone, global and tracker muons.

Standalone muons are reconstructed using only the muon system. Segments from the innermost DT and CSC chambers are used as seeds that give an initial estimate of track parameters (position, momentum and direction). Muon trajectories are then built inside-out using the KF technique. Hits from RPC chambers can participate. The momentum resolution of standalone muons was already shown in Figure 3.8 (black curve). It is around 9% and 20% in the barrel and endcap respectively, due to multiple scattering.

Global muons are the extension of standalone muons. They are built outside-in using both the inner tracker and muon system. The muon trajectory at the innermost muon station is extrapolated to the outer tracker to identify a region of interest (ROI). Inside the ROI the KF algorithm is used to create tracker tracks. This is matched with the standalone muon and parameters are refitted. In the refit, for particles with $p_T < 200\,\text{GeV}$ only tracker information is used because global muons become powerful at high p_T. The efficiency is greater than 99% (see Figure 3.9 for 2017 data).

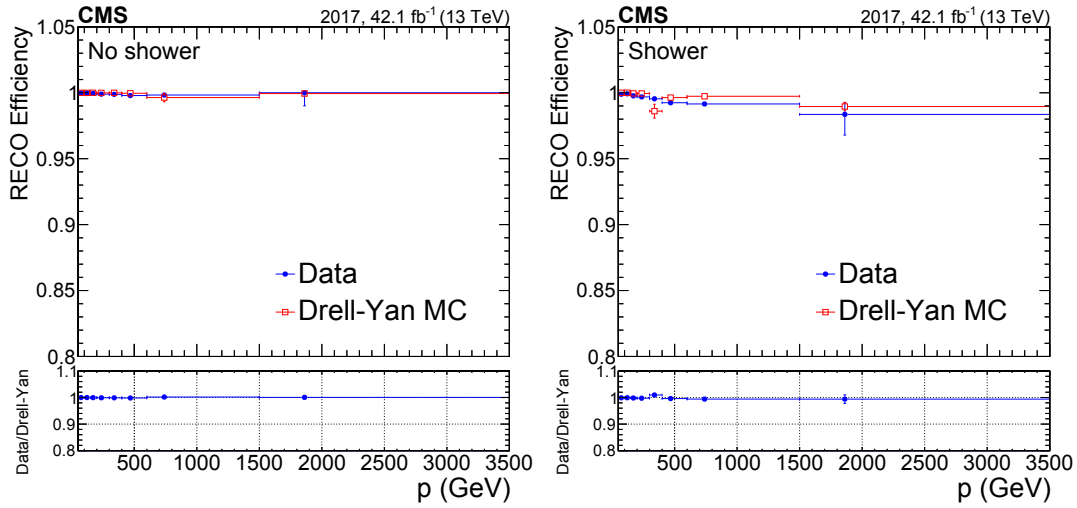

Figure 3.9: Global muon reconstruction efficiency as a function of muon momentum. The left plot is obtained with events without any showers, while the right one contains events with at least one shower. The blue points represent data and the red empty squares represent simulation. The lower panels of the plots show the ratio of data to simulation. The central value in each bin is obtained from the average of the distribution within the bin [184].

Lastly, tracker muons are complementary to global muons, they are in fact reconstructed inside-out. They are particularly efficient in the case of low p_T muons (<6-7 GeV) for which the number of hits in the muon chambers is small. Tracker tracks are propagated towards the solenoid and have to be matched with at least one segment. A subset of tracker muons that will be cited in the next chapter is RPC muons. Depending on the number of RPC layers and stations with hits associated to the track, three working points are defined. The so-called *RPCMuLoose* requires hits on at least two layers.

After the independent reconstruction, the PF algorithm identifies three types of muons

- loose: either tracker or global muons,
- medium: loose muons with the additional tracker and muon quality requirements,
- tight: global muons with constraints on muon quality.

The loose identification recognizes prompt muons from the primary vertex and muons from light and heavy flavor decays. The medium one is optimised for prompt muons and for muons from heavy flavor decay. Finally, the tight identification aims to suppress muons from decay in-flight and from hadronic punch-through induced

by high-energy pions passing through the calorimeters [185]. Another parameter useful to distinguish prompt muons and muons in jets is the isolation estimated from the transverse momentum of PF candidates emitted in a cone with R=0.4 around the muon:

$$\text{Iso} = \frac{1}{p_T^{\mu}} \left\{ \sum p_T^{\text{charged, PV}} + \max\left(0, \sum p_T^{\text{neutral had.}} + \sum p_T^{\gamma} - 0.5 \sum p_T^{\text{charged, PU}}\right)\right\}.$$

3.4 CMS Run 2 data flow

Dealing with raw data from the apparatus would be impossible. Therefore, they have to be processed through the following steps:

1. raw data from the detectors are digitised (DIGI),
2. they passed through reconstruction algorithms to create basic physics object collections (RECO),
3. only some information is kept in the Analysis Object Data (AOD) format,
4. AOD level objects are passed through more selection to discard information and stored in MiniAOD. The design philosophy beneath is to use the minimum amount of space, extracting only the minimum required data and reusing existing formats and algorithms. MiniAOD contains high-level objects (leptons, photons, jets and MET) stored in the PAT (Physics Analysis Toolkit) format, particle candidates from PF in a packed format with only basic kinematic information, trigger data and interaction vertices.
5. Further slimming is performed to obtain NanoAOD.

AOD was used in Run 1 analyses, but is not sustainable for Run 2. MiniAOD and NanoAOD formats meet the challenge of LHC Run 2.

Chapter 4

Dark-SUSY analysis

We implemented a dedicated search for the dark-SUSY process characterised by neutralino pair production events with neutralino ultimately decaying in the dark sector, giving eight muons in the final state.

In this chapter, the details regarding the data and MonteCarlo samples for the signal and background are discussed. The studies to identify suitable triggers are reported together with the algorithm developed to select events. A brief evaluation of the systematic uncertainties, both theoretical and experimental, follows. Finally, some key concepts of statistics are reported to allow for the interpretation of the model independent upper limits.

4.1 Samples

The signal search has been performed with the `DoubleMuon` data collected in 2018 at a center-of-mass energy of 13 TeV. This dataset contains fully reconstructed events selected by a collection of triggers requiring at least two muon objects. The list of samples is reported in Table 4.1. The MiniAOD format described in Section 3.4 has been chosen. The corresponding delivered integrated luminosity is

Table 4.1: 2018 `DoubleMuon` datasets.

Dataset	Number of events
`/DoubleMuon/Run2018A-15Feb2022_UL2018-v1/MINIAOD`	75499908
`/DoubleMuon/Run2018B-15Feb2022_UL2018-v1/MINIAOD`	35057758
`/DoubleMuon/Run2018C-15Feb2022_UL2018-v1/MINIAOD`	34565869
`/DoubleMuon/Run2018D-15Feb2022_UL2018-v1/MINIAOD`	168620231

$67.86\,\text{fb}^{-1}$, of which only $61.31\,\text{fb}^{-1}$ are recorded and certified. UL in the sample name stands for "UltraLegacy" and implies the reprocessing of data with new calibration factors for the ECAL to achieve optimal performance. As already shown in Figure 3.1 the average number of pileup (PU) interactions is 37.

For background and signal, MonteCarlo (MC) samples have been simulated.

4.1.1 Background

The channel analysed is almost free of background. In fact, the number of SM processes that lead to eight muons in the final state is very small. The only contribution arises from multi-vector bosons, such as four Z bosons or two Z plus four W, and the double Higgs production. All these processes, however, have a small cross section which is further reduced by the branching ratio to muons[1]. Thus, they are all negligible.

Still, the average PU is 37 and the contribution of muons originating from semileptonic decays of hadrons has to be taken into account. This, on the one hand, allows for the selection of events that would be otherwise rejected. The top quark, for example, may decay leptonically so an event of $ttZZ$ brings to six muons and, due to the addition of muons from PU, passes the request of eight muons. On the other hand, there is also a background entirely due to the combinatorial of such spurious muons that have to be handled properly. Table 4.2 summarizes all the available samples in the CMS database with a high multiplicity of muons in the final state that might play the role of background in combination with PU muons. The format used is the MiniAODSIM which is the same as MiniAOD with extra information about simulated particles.

The first part of the dataset name provides an indication of the physics channel and the MC generator used for the production (`MadGraph`, `Powheg` [186] or `JHU` generator [187] advisable for the decay of Higgs boson in four leptons). `Pythia` is the program that allows for the description of collisions at high energy between electrons, protons, photons, and heavy nuclei including hard and soft interactions,

[1]Multi-vector bosons cross sections, computed at a center-of-mass energy of 13 TeV, are:

$$\sigma(pp \to 4Z) \times \mathcal{B}^4(Z \to 2\mu) \approx 1.7 \times 10^{-5}\,\text{pb} \times (3.4 \times 10^{-2})^4 \approx \mathcal{O}(10^{-11}\,\text{pb})$$

$$\sigma(pp \to HHjj) \times \mathcal{B}^2(H \to ZZ) \times \mathcal{B}^4(Z \to 2\mu) \approx 1.4 \times 10^{-3}\,\text{pb} \times (2.67 \times 10^{-2})^2 \times (3.4 \times 10^{-2})^4 \approx \mathcal{O}(10^{-12}\,\text{pb})$$

$$\sigma(pp \to 2Z4W) \times \mathcal{B}^2(Z \to 2\mu) \times \mathcal{B}^4(W \to \mu\nu_\mu) \approx 1.2 \times 10^{-7}\,\text{pb} \times (3.4 \times 10^{-2})^2 \times (1.06 \times 10^{-1})^4 \approx \mathcal{O}(10^{-14}\,\text{pb})$$

The last calculation is not straightforward due to the high multiplicity of particle in the final state. A more detailed discussion is reported in Section 6.1.2.

Table 4.2: Background processes datasets.

Dataset	Number of events	Cross section (pb)
/TTZZ_TuneCP5_13TeV-madgraph-pythia8/RunIISummer20UL18MiniAODv2-106X_upgrade2018_realistic_v16_L1v1-v1	457948	1.39×10^{-3}
/TTWW_TuneCP5_13TeV-madgraph-pythia8/RunIISummer20UL18MiniAODv2-106X_upgrade2018_realistic_v16_L1v1-v1	909926	6.98×10^{-3}
/bbH_HToZZTo4L_M125_TuneCP2_13TeV-jhugenv7011-pythia8/RunIISummer20UL18MiniAODv2-106X_upgrade2018_realistic_v16_L1v1-v2	460395	1.38×10^{-3}
/TTZH_TuneCP5_13TeV-madgraph-pythia8/RunIISummer20UL18MiniAODv2-106X_upgrade2018_realistic_v16_L1v1-v2	361927	1.13×10^{-3}
/TTHH_TuneCP5_13TeV-madgraph-pythia8/RunIISummer20UL18MiniAODv2-106X_upgrade2018_realistic_v16_L1v1-v2	499962	6.65×10^{-4}
/GluGluToHHTo2W2ZTo4L_node_cHHH1_TuneCP5_PSWeights_13TeV-powheg-pythia8/RunIIAutumn18MiniAOD-102X_upgrade2018_realistic_v15-v1	978689	4.62×10^{-5}
/GluGluHToZZTo4Mu_M125_TuneCP5_13TeV_powheg2_pythia8/RunIISummer19UL18MiniAODv2-106X_upgrade2018_realistic_v16_L1v1-v1	10775594	1.37×10^{-3}
/TTH_HToJPsiG_JPsiToMuMu_TuneCP5_13TeV-madgraph-pythia8/RunIISummer20UL18MiniAODv2-106X_upgrade2018_realistic_v16_L1v1-v2	499906	1.04×10^{-5}
/GF_HHTo4W_TuneCP5_PSWeights_13TeV-madgraph-pythia8/RunIISummer19UL18MiniAODv2-106X_upgrade2018_realistic_v16_L1v1-v1	1999984	1.37×10^{-3}
/b_bbar_4l_TuneCP5_13TeV-powheg-pythia8/RunIISummer20UL18MiniAODv2-106X_upgrade2018_realistic_v16_L1v1-v1	92655003	52.54

parton distribution functions, initial and final state radiation (ISR and FSR), parton showering, fragmentation and decay [188]. The tune is the set of adjustable parameters that controls the behaviour of the event modelling. The `CP5`, for example, uses the NNPDF3.1 parton distribution functions at the next-to-next-to-leading-order and $\alpha_s = 0.018$ with the one for ISR emissions ordered according to rapidity [189].

The second part, on the other hand, furnishes information about the CMS software (CMSSW) version. When at hand, the recommended MiniAOD second version and global tag `106X_upgrade2018_realistic_v16_L1v1` are chosen. The global tag records all the conditions needed to set up the detector and calibrate its physical response.

Other processes have been initially considered as sources of background, such as $bbH \to WW \to 2\ell 2\nu$, Drell-Yan $\to 2\ell$, and $ttZ \to 2\ell 2\nu$, but they do not pass the trigger requirements discussed in Section 4.2.

4.1.2 Signal

The signal Feynman diagram is the one shown in Figure 2.3. The UFO model generated with `FeynRules` is used in the event generator `MadGraph` to simulate the process under consideration. The mass of $\widetilde{N}_1$ is set to 60 GeV for the reasons explained in Section 2.2.2, the one of n_d to 1 GeV, while different masses of the dark Higgs and photon are taken into account. The dark Higgs mass has to be smaller than the one of $\widetilde{N}_1$, thus the maximum value considered is 55 GeV. The dark photon is limited to half of the mass of the dark Higgs. The complete list is reported in Table 4.3 with the values of the cross section evaluated according to Eq.(2.5) where the branching ratios $\mathcal{B}(\widetilde{N}_1 \to n_d H_d)$ and $\mathcal{B}(H_d \to \gamma_d \gamma_d)$ are equal to 1. The cross section is higher for smaller masses of the dark photon. The full simulation to include the detector is performed according to the recipe in Appendix B.

4.2 Trigger

The signal signature is the presence of eight muons, thus the first selection is based on them. The collection used, called `slimmed muons`, contains all the reconstructed muons in PAT format that pass at least one of these three requirements:

- $p_T > 5$ GeV,
- $p_T > 3$ GeV and any identification (ID) among PF, global, tracker, standalone and `RPCMuLoose` (see Section 3.3.1 for details),
- any p_T if they pass the PF ID.

Table 4.3: Dark Higgs and dark photon masses chosen for signal samples. The cross section has been evaluated for a neutralino mass of 60 GeV assuming the branching ratios $\mathcal{B}(\widetilde{N}_1 \to n_d H_d)$ and $\mathcal{B}(H_d \to \gamma_d \gamma_d)$ equal to 1.

H_d mass (GeV)	γ_d mass (GeV)	Cross section (pb)
55	17.5	3.60×10^{-4}
55	12.5	4.19×10^{-4}
55	7.5	3.95×10^{-4}
55	2.5	2.34×10^{-3}
50	20	3.63×10^{-4}
50	15	3.83×10^{-4}
50	10	4.39×10^{-4}
50	5	5.34×10^{-4}
45	17.5	3.60×10^{-4}
45	12.5	4.19×10^{-4}
45	7.5	3.95×10^{-4}
45	2.5	2.34×10^{-3}
40	15	3.83×10^{-4}
40	10	4.39×10^{-4}
40	5	5.34×10^{-4}
35	12.5	4.19×10^{-4}
35	7.5	3.95×10^{-4}
35	2.5	2.34×10^{-3}
30	10	4.39×10^{-4}
30	5	5.34×10^{-4}
25	7.5	3.95×10^{-4}
25	2.5	2.34×10^{-3}
20	5	5.34×10^{-4}
15	2.5	2.34×10^{-3}

Table 4.4: Selected muon triggers for the analysis.

Trigger	Recorded $\mathcal{L}_{int}$ (fb^{-1})
`HLT_TripleMu_5_3_3_Mass3p8_DZ_v8`	52.22
`HLT_TripleMu_5_3_3_Mass3p8_DCA_v3`	52.22
`HLT_TripleMu_10_5_5_DZ_v10`	52.22
`HLT_TripleMu_12_10_5_v10`	52.22

To reduce the number of events, around 280 trigger paths with requests on three or two muons have been tried. Each one is characterised by different demands on transverse momentum, isolation, and so forth. First of all, the efficiency, i.e. the fraction of events that pass the trigger, on signal samples has been evaluated. Then, to select the ones suitable for the analysis, the total integrated luminosity of the particular HLT in 2018 has to be considered. Triggers with high efficiency but low luminosity in the data taking are discarded, the `HLT_Dimuon0_LowMass` path, for example, has very high efficiency ($\sim 72\%$), but the luminosity is only $9 \times 10^{-3}\,\text{fb}^{-1}$. This allows taking into account also the prescale factors. The chosen triggers are listed in Table 4.4. They all require three muons with different p_T thresholds, identified by the first three numbers in the name. An extra requirement on the invariant mass of dimuon systems to be larger than 3.8 GeV is applied to reduce the rate from resonances as the J/ψ. During the 2016 data taking, a cut on the longitudinal distance between muons along the beam (DZ) was added requiring it to be less than 0.2 cm [190]. A similar request is applied to the distance of closest approach (DCA). Different versions of the path can be applied, labelled by the final number of the name.

The efficiency is shown in Figure 4.1. In general, at a fixed γ_d mass, it is higher for heavier H_d. Except for the smallest dark photon, it is above 70% for all triggers but `HLT_TripleMu_12_10_5` which requires greater transverse momenta for the three muons. The reason for these trends lies in the kinematics of the event. As an example, the distribution of the transverse momentum for the three leading muons is plotted in Figure 4.2 for dark Higgs mass of 55 GeV and 15 GeV (with γ_d mass equal to 2.5 GeV). In the first case, the leading muon (yellow histogram) has an average p_T of 21.7 GeV with a standard deviation $\sigma = 4.4$ GeV. The other two (red and blue histograms) have $p_T = 17.1$ GeV ($\sigma = 3.5$ GeV) and $p_T = 14$ GeV ($\sigma = 3.1$ GeV), respectively. In the second case, instead, the transverse momenta are lower, resulting in an average p_T of 15.9 GeV ($\sigma = 4.4$ GeV) for the first muon, $p_T = 10.9$ GeV ($\sigma = 2.9$ GeV) for the second and $p_T = 8.1$ GeV ($\sigma = 2.2$ GeV) for the third.

To reduce the amount of data to analyse, events are required to have at least eight reconstructed muons of the collection `slimmed muons` and pass one of these

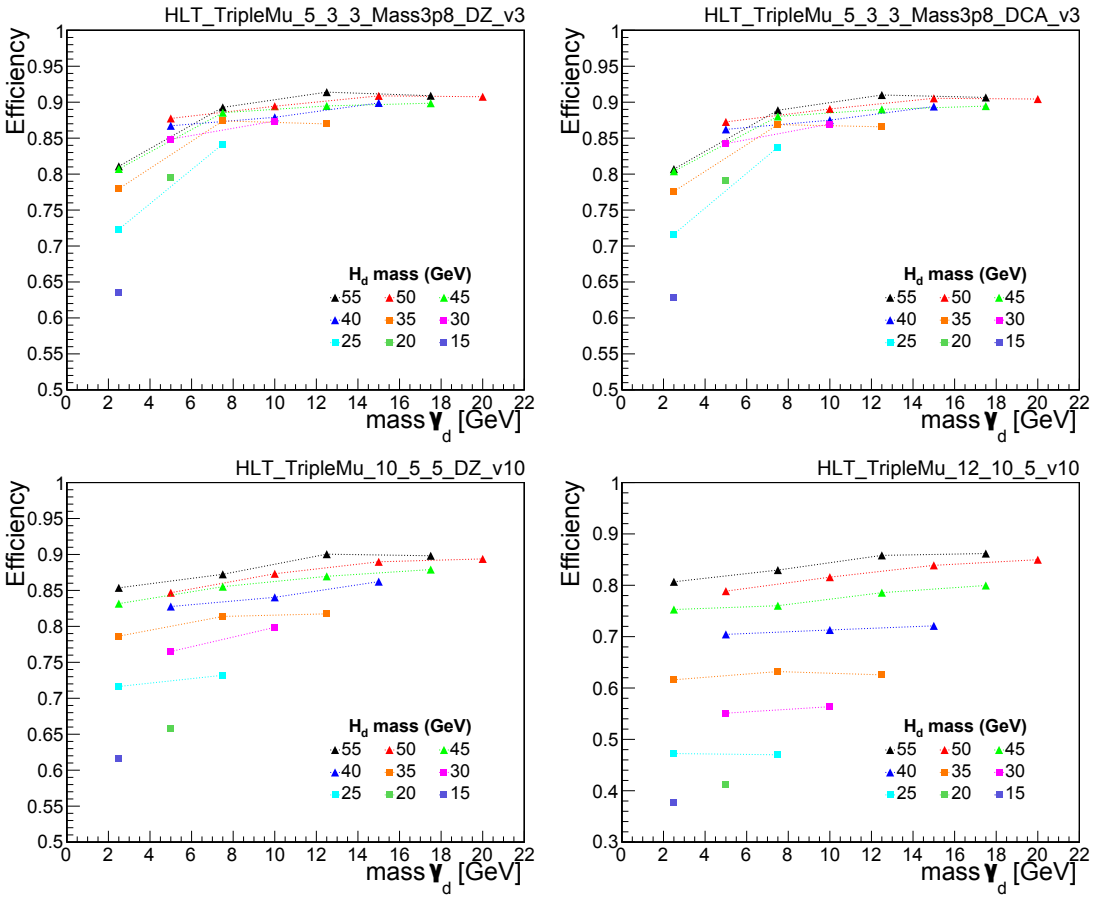

Figure 4.1: Trigger efficiency on signal samples as a function of dark photon mass for different dark Higgs masses. The four trigger paths reported require triple muons and are the ones selected for the analysis.

four triggers. The efficiency of this first selection on signal is shown in Figure 4.3 on the left. The loss of efficiency compared to the ones for the triggers in Figure 4.1 is due to the request for eight muons to be reconstructed. For the background, the number of events expected has been evaluated as:

$$B = \epsilon\sigma\mathcal{L} \tag{4.1}$$

with ϵ the efficiency, σ the cross sections reported in Table 4.2, and $\mathcal{L}$ the integrated luminosity for 2018 equal to 61.31 fb^{-1} as discussed at the beginning of this chapter. In this case, the efficiency is less than 20% resulting in less than 10 expected events for all processes but $b\bar{b}$ which is characterised by the highest cross section.

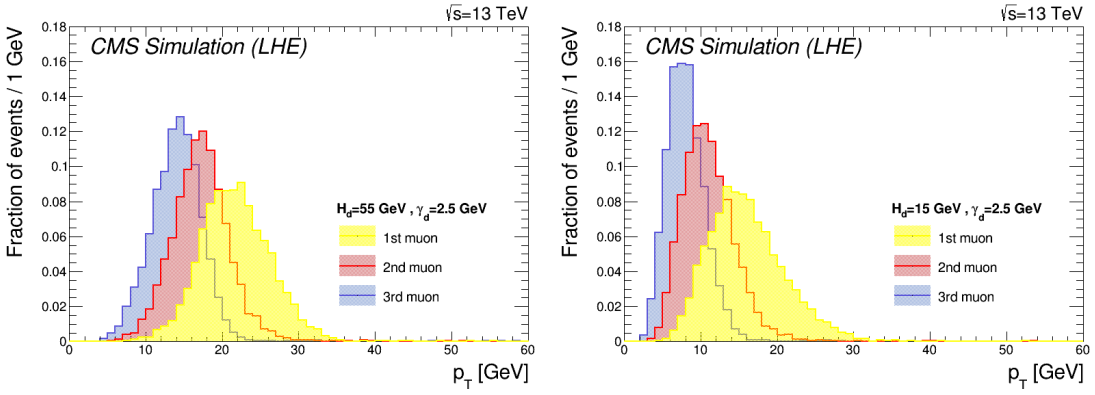

Figure 4.2: Transverse momentum distributions of the three leading generated muons from the LHE (Les Houches Event) file for γ_d mass of 2.5 GeV and H_d mass of 55 GeV (left) and 15 GeV (right).

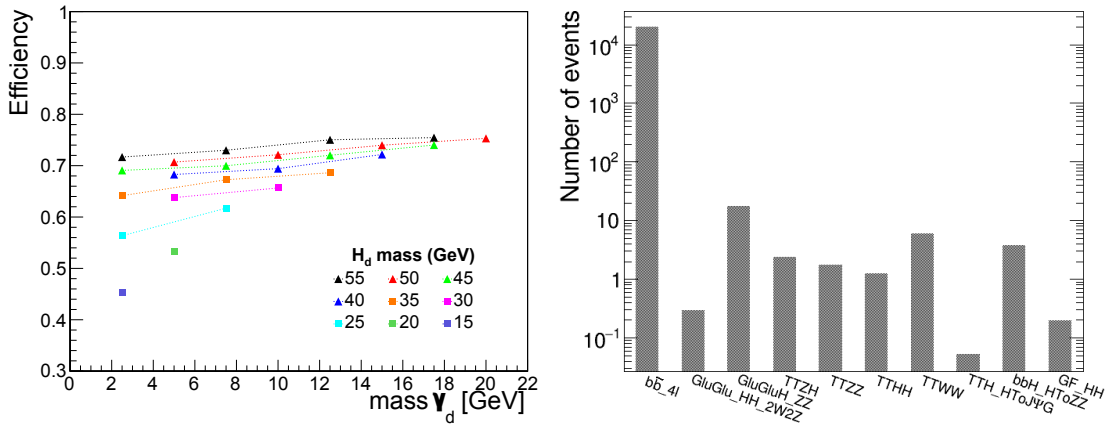

Figure 4.3: Left: Efficiency for signal samples. Efficiency is defined as the fraction of events that have equal or more than eight reconstructed muons and pass at least one of the triggers `HLT_TripleMu_5_3_3_Mass3p8_DZ_v8`, `HLT_TripleMu_5_3_3_Mass3p8_DCA_v3`, `HLT_TripleMu_10_5_5_DZ_v10` or `HLT_TripleMu_12_10_5_v10`. Right: Number of events expected for the background processes calculated according to Eq. 4.1.

4.3 Selection algorithm

Since the final state consists of oppositely charged muons from dark photon decays, an algorithm is designed to pair muons by exploiting the symmetry of the event. The steps are the following:

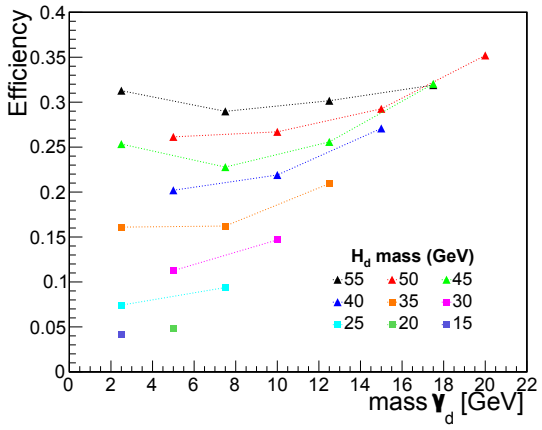

Figure 4.4: Efficiency for signal samples. Efficiency is defined as the fraction of events selected by the algorithm in a defined mass region.

- among all the reconstructed muons passing the trigger, the first eight with higher transverse momentum are selected requiring four with a positive and four with a negative charge. An additional requirement is added on the distance of the associated tracker track from the primary vertex. The transverse impact parameter (d_{xy}) is smaller than 2 mm, in order to suppress cosmic muons while preserving muons from the b and c decays. The longitudinal distance (d_z) is smaller than 5 mm. This again allows getting rid of cosmic muons and suppressing tracks from PU.
- The eight muons are coupled in pairs according to the charge, and then two pairs are associated if they satisfy the condition given by:

$$\frac{|m_{(\mu\mu)1} - m_{(\mu\mu)2}|}{\frac{1}{2}(m_{(\mu\mu)1} + m_{(\mu\mu)2})} < 0.2, \tag{4.2}$$

  where $m_{(\mu\mu)}$ is the pair invariant mass. This is based on the assumption that the dark photons from which the muon pairs originate decay in the same way.
- If the four muon pairs respect Eq. (4.2), a similar cut is applied to the quartets

$$\frac{|m_{(\mu\mu\mu\mu)1} - m_{(\mu\mu\mu\mu)2}|}{\frac{1}{2}(m_{(\mu\mu\mu\mu)1} + m_{(\mu\mu\mu\mu)2})} < 0.2$$

  assuming again that the dark Higgses decay in the same way.

This algorithm is independent of the masses of dark photons and dark Higgs. To evaluate the acceptance of this criterion, the number of events inside a mass region

Table 4.5: List of the tentative cuts added to the selection algorithm.

Cut	Brief description
C1	$4\mu^+4\mu^-$ from primary vertex
C2	$4\mu^+4\mu^-$ from primary vertex & ≥ 4 tight (+medium)
C3	$4\mu^+4\mu^-$ from primary vertex & MET$< 40\,\text{GeV}$
C4	$4\mu^+4\mu^-$ from primary vertex & MET$< 50\,\text{GeV}$
C5	$4\mu^+4\mu^-$ from primary vertex & no jet $p_T < 50\,\text{GeV}$
C6	$4\mu^+4\mu^-$ from primary vertex & no b-jet $p_T < 50\,\text{GeV}$
C7	$4\mu^+4\mu^-$ from primary vertex & all μ $p_T > 3\,\text{GeV}$

that pass all the requests in the above list are counted. The mass region is defined by requiring the mass of the muon quartet/pair (m) to be

$$|m - m_{\text{ref}}| < 2\sigma_{\text{ref}}, \tag{4.3}$$

where "ref" refers to the dark Higgs/photon and the standard deviation σ has been obtained by the fit of the mass distribution. The efficiency of the algorithm on the signal is shown in Figure 4.4 as a function of the dark photon mass for different values of dark Higgs mass. As expected, it is higher for greater masses because the muon transverse momentum increases and therefore the resolution on reconstructed p_T, and consequently on invariant mass, improves.

4.3.1 Additional cuts

To further reduce the number of events selected by the algorithm, additional cuts have been applied. They are all listed in Table 4.5. The first one, labelled as C1, is the starting request of the algorithm: four of the eight muons should have a positive electric charge and the other negative to build pairs and they should all be associated with the primary vertex ($d_{xy} < 2\,\text{mm}$ and $d_z < 5\,\text{mm}$).

In addition to this, C2 requires at least four muons to be identified as tight and the remaining as medium. As already introduced in Section 3.3.1, medium muons are loose muons with a fraction of valid tracker hits greater than 80%. They also need to satisfy a tight request on segment compatibility (> 0.451) or a looser one (> 0.303) in addition to cuts on the χ^2 of the global track, on the kink and the matching with the tracker standalone segment. Tight muons, on the other hand, are PF candidates reconstructed as global muons with a normalised χ^2 of the global-muon track fit smaller than 10 and at least one muon-chamber hit included in the fit to suppress the hadronic punch-through and muons from decay in-flight. They should have muon segments in at least two muon stations to avoid accidental track-to-segment matches. They come from the primary vertex with

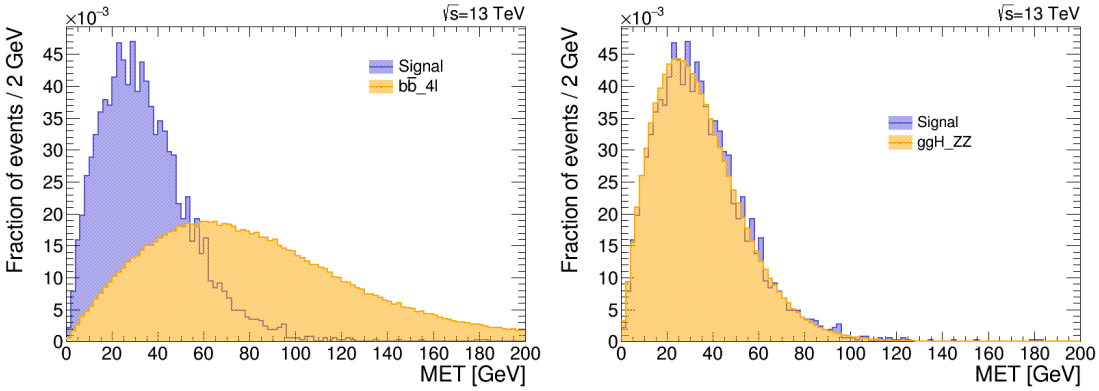

Figure 4.5: Missing transverse energy (MET) distribution for the signal with the H_d = 45 GeV and the $\gamma_d = 17.5$ GeV (blue histogram) and the background (orange histogram) $b\bar{b} \to 4\ell$ on the left and $ggH \to ZZ$ on the right.

the previously discussed cuts on the transverse impact parameter and longitudinal distance. At least one pixel hit is required and more than 5 tracker layers should have hits to guarantee a good p_T measurement.

C3 and C4 add the request on the MET, while C5 and C6 on the presence of jets. Figure 4.5 on the left compares the MET distribution of the signal (H_d mass = 45 GeV and γ_d mass = 17.5 GeV) in blue with the one of $b\bar{b}$ process in orange. It is evident that the cuts on the MET allow getting rid of most of the background preserving the signal. For other background sources, such as the double Z bosons from the Higgs, instead, this cut is not efficient since the MET distribution for signal and background is very similar (Figure 4.5 right). For the b-tagging the `DeepFlavour` discriminator has been used. It was a deep-neural network algorithm added in 2017 and exploits effectively all PF candidates and vertices as input [191]. The b discriminator is the sum of `pfDeepFlavourJetTags:probb`, `pfDeepFlavourJetTags:probbb`, `pfDeepFlavourJetTags:problepb`, which represent the probability of having one bottom quark, two or one with a lepton, respectively with the recommended working point 0.6377. Finally, C7 requires all eight muons to have a transverse momentum greater than 3 GeV.

The efficiency for the signal with several combinations of these cuts is shown in Figure 4.6. In general, the different additional requests do not lower drastically the efficiency with respect to the first request of the algorithm (C1). Figure 4.7 compares the signal for $H_d = 45$ GeV and $\gamma_d = 17.5$ GeV with two background samples surviving the cuts. Blank spaces correspond to get rid of all background. The cut on the b-jets, for example, removes completely the contribution of $b\bar{b} \to 4\ell$.

To have a preliminary estimate of the sensitivity, the simplified formula pro-

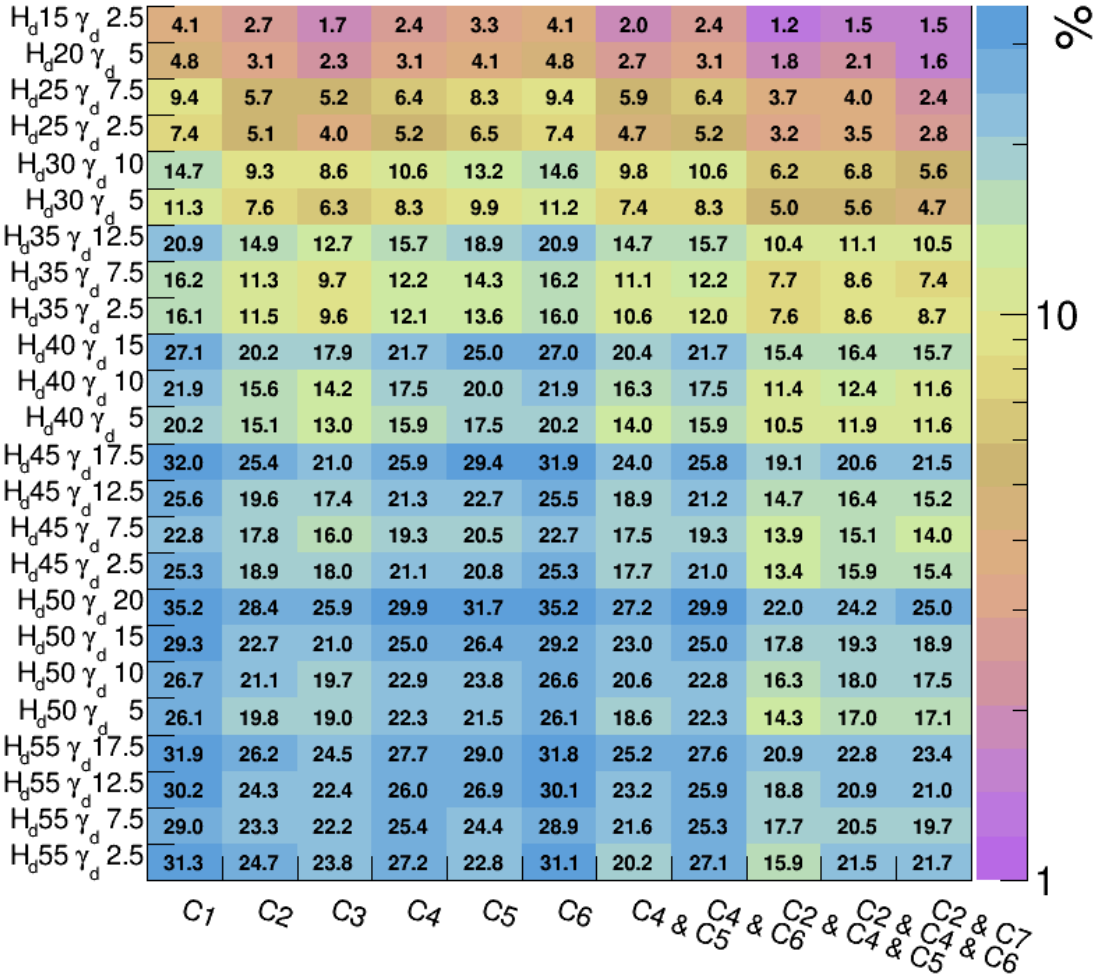

Figure 4.6: Signal efficiency, i.e. fraction of signal events selected by the algorithm and satisfying the additional requests, for different combinations of the cuts described in Table 4.5.

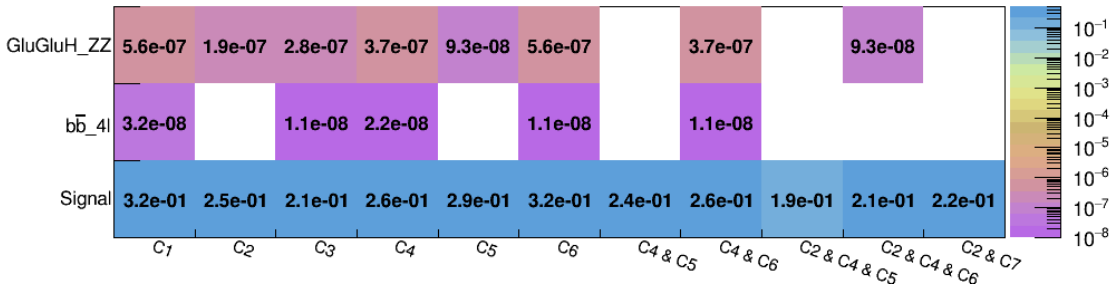

Figure 4.7: Efficiency, i.e. fraction of events selected by the algorithm (m_{ref} for quartets = 45 GeV and m_{ref} for pairs = 17.5 GeV) and satisfying the additional requests, on signal and background samples for different combinations of the cuts described in Table 4.5. The two background processes reported are the only ones surviving the selection.

posed in Ref. [192] has been used:

$$\frac{\epsilon}{a/2 + \sqrt{B}}. \tag{4.4}$$

Here ϵ is the signal efficiency shown in Figure 4.6, a the number of standard deviations corresponding to a one-sided Gaussian test at a certain significance α (for the following calculation $a = 1$) and B the number of background events. Worthy to observe, the expression does not depend on the signal cross section. This sensitivity is used as a cross-check for the choice of the cuts to apply. The background yield is computed as in Eq. (4.1). The goal is to maximise this sensitivity, which basically reflects the trend of efficiency due to the neglecting contribution of the background. Higher masses of the dark Higgs are more sensitive (see Figure B.1 in Appendix A).

The signal yield can be computed too by using $S = \epsilon\sigma\mathcal{L}$ with the cross sections in Table 4.3 where the neutralino mass is fixed to 60 GeV and the branching ratios $\mathcal{B}(\widetilde{N}_1 \to n_d H_d)$ and $\mathcal{B}(H_d \to \gamma_d\gamma_d)$ to 1 (see Figure 4.8). The lower efficiency at small masses is compensated by the higher cross section.

For this purpose, the cut labelled as C2 has been selected because it lets to get rid of bottom and charmed mesons efficiently, maintaining a high sensitivity according to Eq. (4.4). The invariant mass of the two muon pairs obtained by combining the four reconstructed muons with higher p_T is shown in Figure 4.9 (left). In blue the distribution for all the events recorded in 2018 is reported, while in red the one of the events passing the selection algorithm presented above without the requirement on the distance of the tracker track associated with the muon from the primary vertex. The peaks corresponding to the J/ψ and Υ resonances are clearly visible. On the right, the request on the primary vertex has been added.

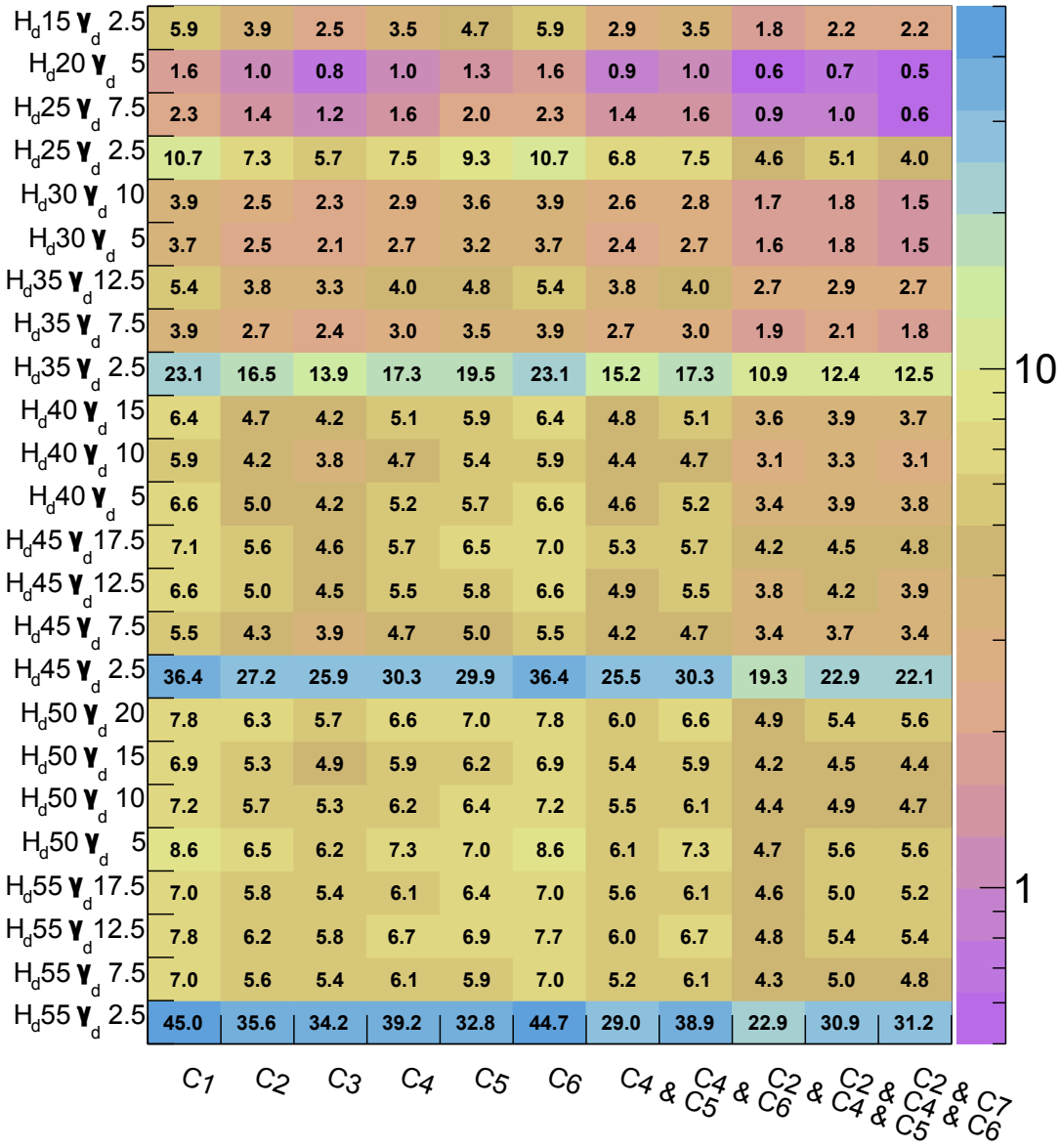

Figure 4.8: Signal yield ($S = \epsilon\sigma\mathcal{L}$) for different combinations of cuts described in Table 4.5. The cross section σ has been evaluated for a neutralino mass of 60 GeV assuming the branching ratios $\mathcal{B}(\widetilde{N}_1 \to n_d H_d)$ and $\mathcal{B}(H_d \to \gamma_d\gamma_d)$ equal to 1.

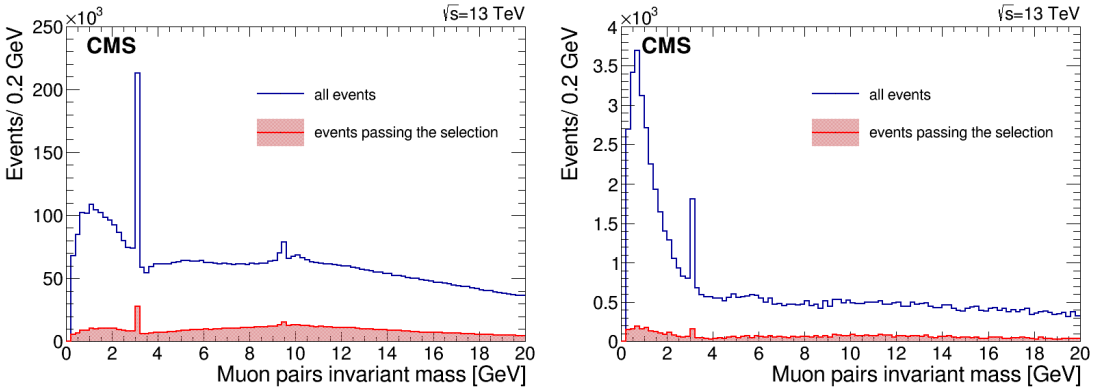

Figure 4.9: Muon pairs invariant mass distribution for data recorded by the CMS experiment in 2018. The first four muons with the highest transverse momentum and right charges are combined into pairs. In blue all the events and in red only the ones passing the selection algorithm. On the left, no request on the primary vertex is added, while on the right the four muons must have a transverse impact parameter (d_{xy}) smaller than 2 mm and a longitudinal distance (d_z) smaller than 5 mm.

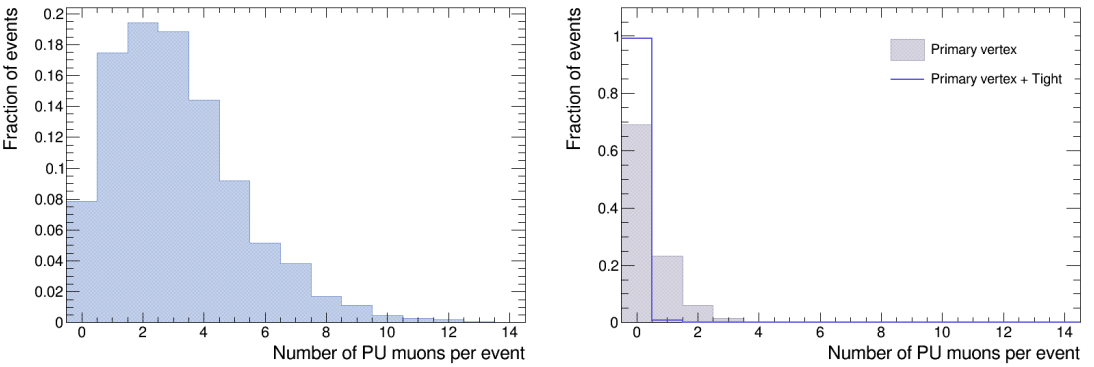

Figure 4.10: Right: distribution of the number of muons per event from pileup (PU). Right: distribution of the number of muons per event from PU with the request on the primary vertex (grey histogram) and tight identification (blue line).

This suppresses the Υ peak, but not completely the J/ψ one. With the request of C2, i.e. the cut on muon quality, this contribution is completely removed. This requirement is efficient also with PU muons. Figure 4.10 shows the distribution of the number of muons per event from simulated PU from one of our signal samples. There are, on average, three muons per event from PU, but by adding the request on the vertex and tight quality, they are all suppressed.

4.4 Systematic uncertainties

The calculation of the upper limits permits to incorporate the systematic uncertainties via nuisance parameters. Two classes, derived from previous studies [142, 193], have been taken into account: theoretical and experimental. They apply both to signal and background.

4.4.1 Theoretical uncertainties

First of all, as already discussed in Section 2.2.2, for a neutralino mass of 60 GeV, the dominant process for neutralino pair production is through the SM Higgs boson. Its production at the LHC depends on its transverse momentum which is affected by initial state radiation. While for $p_T \sim m_H$ the QCD radiative correction can be evaluated perturbatively through the fixed-order expansion, for $p_T \ll m_H$ Sudakov logarithms have to be taken into account, and all terms resummed. The signal MC samples are generated at LO. The corrections at NLO are known only in the limit of the top quark mass going to infinity, but the ones at NNLO have been computed in Ref. [194]. Therefore, a conservative systematic uncertainty of 2% is considered.

In addition, the uncertainties on the Higgs boson production cross section and branching ratio are set to 3.2% [195] and 2% [196] respectively.

Finally, systematic uncertainties related to the parton distribution function, the strong coupling α_s, and the QCD scales, i.e. renormalization and factorization, are studied [196, 197]. The factorization scale corresponds to the resolution with which the hadron is probed, while the renormalization one is introduced to resolve the ultraviolet divergence in the amplitudes. They are treated as uncorrelated and summed in quadrature giving a contribution of 8%.

4.4.2 Experimental uncertainties

From the experimental point of view, the first contribution is given by the uncertainty of luminosity measurement. The instantaneous luminosity is determined through

$$\mathcal{L}_{inst} = \frac{R}{\sigma_{vis}},$$

where R is the rate of detector measured quantities (e.g. hits, tracks, clusters) and σ_{vis} the visible cross section, determined via Van der Meer scan, which may suffer for many effects. Details of the procedure are reported in Ref. [198]. The uncertainty is 2.5%.

Secondly, the uncertainty on the muon reconstruction and identification is evaluated with the tag-and-probe method following the instructions recommended by

the Muon Physics Object Group. This allows for the study of systematic error as a function of the muon p_T and η. The analysis is performed using the dataset `Charmomium` both with MC Drell-Yan plus jet sample with $p_T > 8\,\text{GeV}$ and an MC J/ψ sample with $p_T > 2\,\text{GeV}$. The result is an overall uncertainty of 0.6% per muon, dominated by the region of $0 < \eta < 0.9$ [142]. This translates to an average of 4.8%.

The triple muon trigger efficiency is determined with the orthogonal method by using the three-muon events in the WZ dataset [142]. This method assumes that such events are mainly triggered by the substantial MET in the event topology, and therefore independent of muons selection criteria, thus ensuring an unbiased estimation of the efficiency. This results in an uncertainty of 6%.

Finally, the dimuon pairs can be affected by the overlap of muons in the tracker and muon system [199]. For these effects, conservative uncertainties of 1.3% and 1.2% per dimuon are set for the tracker and muon subdetectors respectively.

Other sources, such as the one related to muon tracking and pileup, are negligible.

4.5 Statistical interpretation for upper limits

For the statistical analysis, the frequentist limit recommended by the LHC Higgs combination group [200] with test statistics based on the profile likelihood is used [201].

The parameter of interest, i.e. the quantity on which the limit is calculated, is the signal strength modifier r. It is the number of signal events over the number of expected signal events. As already said, multiple systematic uncertainties can be handled with nuisance parameters θ. Assuming s and b the expected event yield of signal and background respectively, the upper limit is the product of Poisson probabilities:

$$\lambda(\text{data}|r,\theta) = \text{Poisson}(\text{data}|r \cdot s(\theta) + b(\theta)) \cdot p(\tilde{\theta}|\theta) \tag{4.5}$$

where "data" are the experimental observations. $p(\tilde{\theta}|\theta)$ is the probability density function of nuisance parameters used to construct sampling distributions. It defines the probability for the true value of a nuisance parameter to be equal to θ when the measurement gives $\tilde{\theta}$ as the best estimate. In the case of binned maximum likelihood fit,

$$\text{Poisson}(\text{data}|r \cdot s(\theta) + b(\theta))$$

is

$$\prod_i \frac{(r \cdot s_i(\theta) + b_i(\theta))_i^n}{n_i!} e^{-r \cdot s_i(\theta) - b_i(\theta)}$$

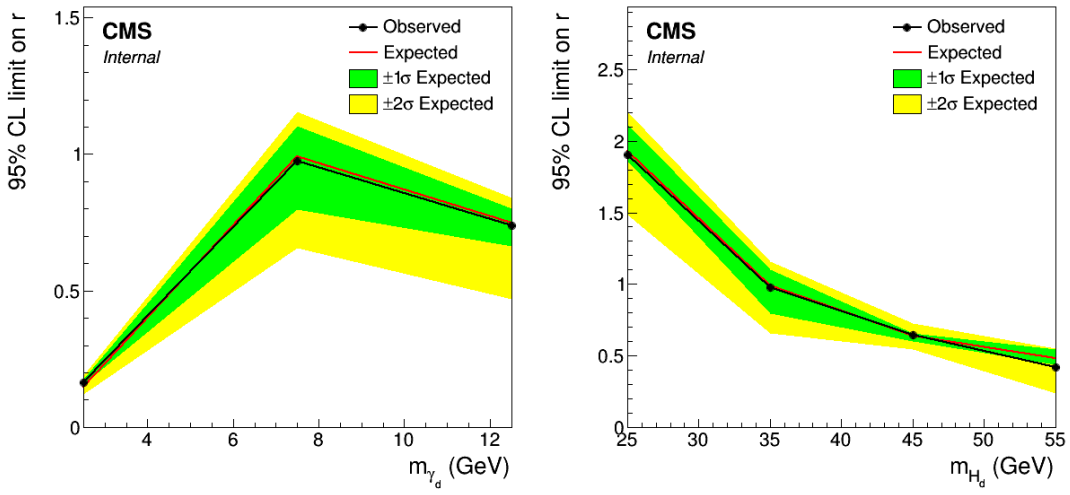

Figure 4.11: Left: Expected and observed 95% CL upper limit on r as a function of m_{γ_d} mass for a H_d mass of 35 GeV. Right: Expected and observed 95% CL upper limit on r as a function of H_d mass for a m_{γ_d} mass of 7.5 GeV.

, where n_i is the number of observed data events in the i-th bin, and s_i and b_i the expected yield in the same bin.

The test statistics based on profile likelihood (see Ref. [202] for further details) is used:

$$q_r = -2 \ln \left[\frac{\lambda(\text{data}|r, \hat{\theta}_r)}{\lambda(\text{data}|r = \hat{r}, \hat{\theta})} \right]$$

with $0 \leq \hat{r} \leq r$. $\hat{\theta}_r$ is the conditional maximum likelihood estimator for θ given r and data. The pair of estimator parameters $\hat{r}$ and $\hat{\theta}$ corresponds to the global maximum of the likelihood in Eq. (4.5). The nuisance parameters are therefore separately profiled for $r = \hat{r}$ and r. The limit $\hat{r} > 0$ is dictated by physics, while $\hat{r} \leq r$ guarantees a one-sided confidence interval. This equation allows finding the observed value $\tilde{q}_r^{\text{obs}}$ for a given r under test. By maximising Eq. (4.5), the values for the nuisance parameters $\tilde{\theta}_0^{\text{obs}}$ and $\tilde{\theta}_r^{\text{obs}}$ are computed. They represent the background only and signal plus background hypothesis. In fact, the number of observations is:

$$N_o = r \cdot s + b$$

and for $r = 0$ only the background contributes. At this point, toy experiments are simulated with MC method to construct the probability distribution functions:

$$f(\tilde{q}_r|r, \hat{\theta}_r^{\text{obs}})$$

$$f(\tilde{q}_r|0, \hat{\theta}_0^{\text{obs}})$$

for the two hypotheses.

The p-values are defined to quantify the degree of compatibility with $\tilde{q}_r^{\text{obs}}$ as:

$$p_r = P(\tilde{q}_r > \tilde{q}_r^{\text{obs}}|\text{signal+background}) = \int_{\tilde{q}_r^{\text{obs}}}^{\infty} f(\tilde{q}_r|r, \hat{\theta}_r^{\text{obs}}) d\tilde{q}_r$$

$$1 - p_b = P(\tilde{q}_r > \tilde{q}_r^{\text{obs}}|\text{background only}) = \int_{\tilde{q}_r^{\text{obs}}}^{\infty} f(\tilde{q}_r|0, \hat{\theta}_0^{\text{obs}}) d\tilde{q}_r.$$

The test confidence level is:

$$CLs(r) = \frac{p_r}{1 - p_b} \leq \alpha.$$

For example, the 95% CL upper limit on r is found when $CLs(r)$ is equal to 0.05. For nuisance parameters, the log-normal probability density functions are used.

The upper limit has been evaluated with `Combine` tool to generate the Brazilian plots. They are typically used to present exclusion limits for the existence of new particles. In this case, they provide the exclusion for the expected signal yield. The two examples in Figure 4.11 are discussed in detail in the next section.

4.6 Results

The selection algorithm in Section 4.3, with the additional cut requiring at least four tight muons and the remaining medium muons, allows for the evaluation of signal and background yields. These last are basically zero. Concerning the signal (see Figure 4.8), the cross section σ has been evaluated for a neutralino mass of 60 GeV assuming the branching ratios $\mathcal{B}(\widetilde{N}_1 \to n_d H_d)$ and $\mathcal{B}(H_d \to \gamma_d \gamma_d)$ equal to 1. This ensures that results are model independent. The events collected by the CMS experiment in 2018, corresponding to an integrated luminosity of 61.31 fb^{-1}, have also been counted.

From these numbers the 95% CL upper limit on the expected signal yield has been evaluated using the frequentist limit with test statistics based on the profile likelihood for different combinations of the dark photon and dark Higgs masses. Figure 4.11 shows the results for $m_{H_d} = 35\,\text{GeV}$ (left) and $m_{\gamma_d} = 7.5\,\text{GeV}$ as a function of the dark photon and dark Higgs mass, respectively. For $r < 1$ we can exclude the decay of the neutralino in eight muons. This is always the case except for the combinations reported in Table 4.6.

A summary picture is presented in Figures 4.12 and 4.13 where the theoretical predictions of the cross section are compared with the experimental limits at 95% CL. In both plots, the solid curves represent the model with a neutralino mass

Table 4.6: Dark Higgs and dark photon masses not excluded by the model independent analysis.

H_d mass (GeV)	γ_d mass (GeV)
20	5
30	5
25	7.5
35	7.5
30	10

of 60 GeV, the wino soft-SUSY breaking mass M_2 equal to 191.5 GeV, the Higgs-higgsino mass parameter μ at 357.7 GeV and $\tan\beta = 9.75$. The corresponding $\sigma(pp \to \widetilde{N_1}\widetilde{N_1})$ is 1.148 pb. The branching ratios $\mathcal{B}(\widetilde{N_1} \to H_d n_d)$ and $\mathcal{B}(H_d \to \gamma_d\gamma_d)$ are set to 1. The dependence of the solid green curve in Figure 4.12 on the dark photon mass arises from the calculation of the branching fraction $\mathcal{B}(\gamma_d \to 2\mu)$, while the solid lines in Figure 4.13 parallel to the x-axis are due to the independence from m_{H_d}, having assumed $\mathcal{B}(H_d \to \gamma_d\gamma_d) = 1$. For each dark Higgs mass, there is a splitting of predictions related to the different assumptions of dark photon mass. The experimental curves are extrapolated from the calculated limits on r described in the previous paragraph.

From Figure 4.12 it is evident that most of the experimental curves lay in the exclusion region bounded at the top by the theoretical prediction. In Figure 4.13 H_d masses higher than 30-35 GeV are excluded except for $m_{\gamma_d} = 2.5$ GeV.

When a more complete theory of the dark sector with all possible neutralino decays becomes available, the results presented here could be reused with appropriate reworking for a precise estimation of the hidden sector couplings. For example, a branching ratio of 0.1, instead of 1, would reduce the exclusion range. In this case, the sensitivity would benefit from a higher luminosity.

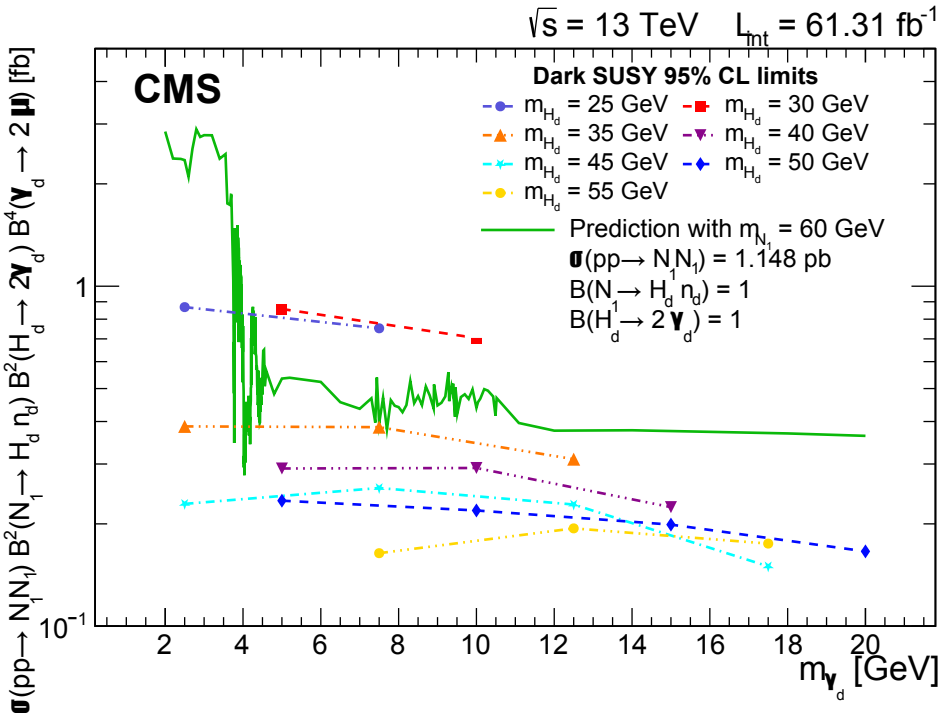

Figure 4.12: Expected 95% CL upper limits as a function of the dark photon mass m_{γ_d} on $\sigma(pp \to N_1N_1) \times \mathcal{B}^2(N_1 \to H_d n_d) \times \mathcal{B}^2(H_d \to \gamma_d\gamma_d) \times \mathcal{B}^4(\gamma_d \to 2\mu)$ with different values of m_{H_d} (dashed and dash-dotted curves). The limits are compared to the predicted rate (solid green curve) obtained using the simplified scenario with $\sigma(pp \to N_1N_1) = 1.148\,\text{pb}$ – corresponding to a neutralino mass of 60 GeV, $M_2 = 191.5\,\text{GeV}$, $\mu = 357.7\,\text{GeV}$ and $\tan\beta = 9.75$ – and $\mathcal{B}(N_1 \to H_d n_d) = 1$ and $\mathcal{B}(H_d \to \gamma_d\gamma_d) = 1$.

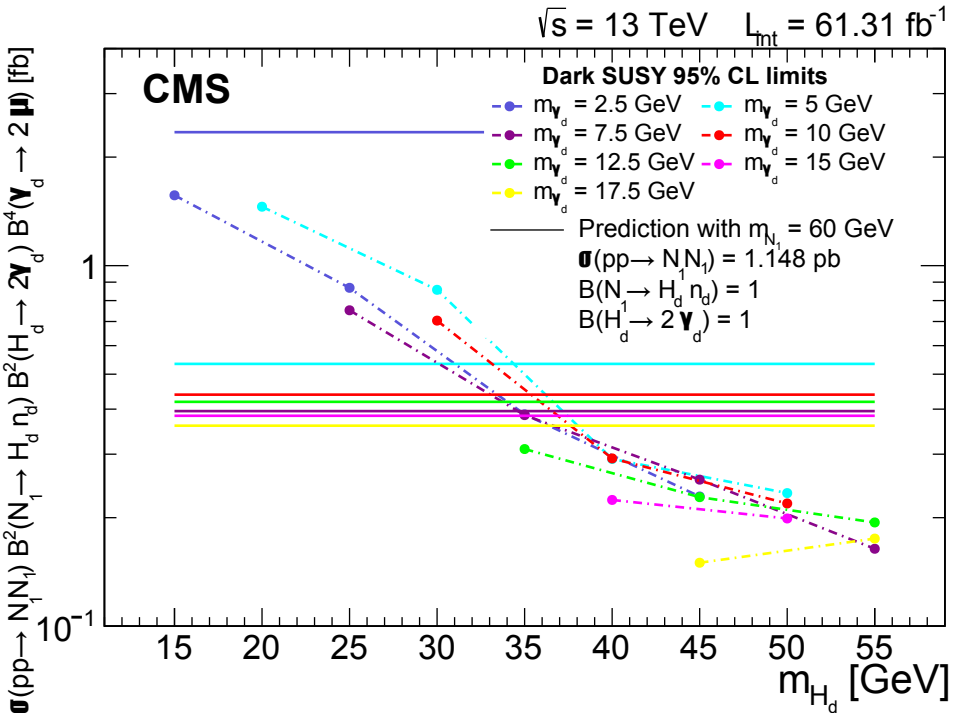

Figure 4.13: Expected 95% CL upper limits as a function of the dark Higgs mass m_{H_d} on $\sigma(pp \to N_1N_1) \times \mathcal{B}^2(N_1 \to H_d n_d) \times \mathcal{B}^2(H_d \to \gamma_d\gamma_d) \times \mathcal{B}^4(\gamma_d \to 2\mu)$ with different values of m_{γ_d} (dashed and dash-dotted curves). The limits are compared to the predicted rate (solid curve) obtained using the simplified scenario with $\sigma(pp \to N_1N_1) = 1.148\,\text{pb}$ – corresponding to a neutralino mass of 60 GeV, $M_2 = 191.5\,\text{GeV}$, $\mu = 357.7\,\text{GeV}$ and $\tan\beta = 9.75$ – and $\mathcal{B}(N_1 \to H_d n_d) = 1$ and $\mathcal{B}(H_d \to \gamma_d\gamma_d) = 1$.

Part II

A future outlook

Chapter 5

The Muon Collider

All the results obtained by experimental particle physics in the last sixty years and the discovery of the Higgs boson confirm that colliders are at the forefront of scientific discoveries in high-energy physics. The next colliders should offer broad opportunities for physics beyond the Standard Model. The case of a Muon Collider is discussed in this chapter after a rapid mention of future proposed accelerators. The design and construction of such a machine are going to present technological and experimental challenges mainly because of muon unstable nature. However, the final reward will be an extraordinary discovery potential.

A description of the detector and a brief discussion of the physics objects reconstruction is reported. In the end, details of the muon system and considerations about the technologies are examined.

5.1 Proposed future machines

The machines proposed for the future mainly belong to two groups:

- hadron colliders that move towards the energy frontier for the direct search of new physics
- electron-positron colliders that push the luminosity frontier, working at "lower" energy, for precision measurements campaign of Higgs and EW sector.

The collision of a hadron and a lepton is another option under investigation in particular to measure the proton substructure.

Table 5.1 summarizes the parameters of some future colliders. HL-LHC has been already discussed in Section 3.1.1. The hadron Future Circular Collider (FCC-hh) has been proposed to be hosted in a 100 km tunnel at CERN and will

Table 5.1: Summary of some proposed future colliders. The operative center-of-mass energy $\sqrt{s}$, the instantaneous and integrated luminosity and data taking years are reported. Table readapted from [203].

	beams	$\sqrt{s}$	$\mathcal{L}$ ($10^{34}\,\mathrm{cm}^{-2}\mathrm{s}^{-1}$)	$\mathcal{L}_{int}$ (ab^{-1})	time (years)	Refs.
HL-LHC	pp	14 TeV	5	6	12	[204]
FCC-hh	pp	100 TeV	30	30	25	[205]
FCC-ee	ee	91 GeV	100-200	150	4	[205]
		161 GeV	25	10	1-2	
		240 GeV	7	5	3	
		365 GeV	0.8-1.4	1.5	5	
CEPC	ee	91 GeV	17-32	16	2	[206]
		161 GeV	10	2.6	1	
		240 GeV	3	5.6	7	
ILC	ee	250 GeV	1.35-2.7	2	11.5	[207, 208]
		350 GeV	1.6	0.2	1	
		500 GeV	1.8-3.6	4	8.5	
		(1 TeV)	(3.6-7.2)	(8.0)	(8.5)	
CLIC	ee	380 GeV	1.5	1	8	[209]
		1.5 TeV	3.7	2.5	7	
		3 TeV	6	5	8	

reach the unprecedented center-of-mass energy of 100 TeV. This machine will also work as electron-positron collider at $\sqrt{s}$ close to the masses of Z (91 GeV), $2W$ (161 GeV) and 2 top quark (365 GeV). The Circular Electron Positron Collider (CEPC) in China will be as long as the FCC and will operate at the same center-of-mass energy of FCC-ee. The International Linear Collider (ILC) in Japan will study new physics in exotic Higgs decay (Higgs factory at 250 GeV), pair production of WIMPS, top quark and Higgs self-coupling. Finally, the Compact LInear Collider (CLIC) will have great potential for dark matter and new state discoveries. At the first proposed $\sqrt{s}$, it will focus on Higgs and top quark physics, then it will investigate the double Higgs production and rare decays and, at 3 TeV, the Higgs self-coupling and new physics.

Hadron colliders' main drawback is the pileup that makes reconstruction challenging. Electron-positron colliders, on the other hand, offer a clean environment. However, electron small mass prevents it to reach high energies because of losses due to synchrotron radiation. A possible solution is the linear colliders, but their huge length and the energy waste due to *Bremsstrahlung* make them very expensive. For all these reasons, already in the 1970s, the possibility of a muon collider

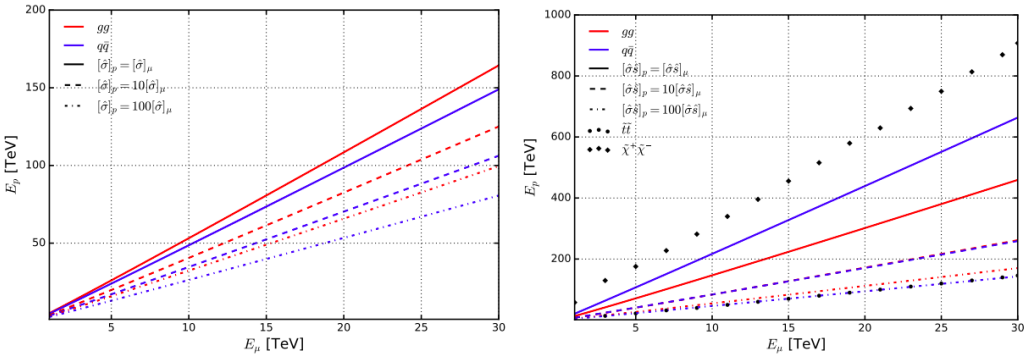

Figure 5.1: The equivalent proton collider energy $E_p = \sqrt{s_p}$ [TeV] required to reach the same beam-level cross section as a $\mu^+\mu^-$ collider with energy $E_\mu = \sqrt{s_\mu}$ [TeV] for $2 \to 1$ (left) and $2 \to 2$ (right) parton-level process, for benchmark scaling relationships between the parton-level cross sections $[\hat{\sigma}]_p$ and $[\hat{\sigma}]_\mu$ as well as for pair production of $\tilde{t}\bar{\tilde{t}}$ and $\tilde{\chi}^+\tilde{\chi}^-$through their leading $2 \to 2$ production modes [154].

has been introduced [210].

5.1.1 Advantages of a Muon Collider

A muon collider represents a promising solution because it combines the high precision of e^+e^- colliders and the high center-of-mass energy and luminosities of hadron machines.

Compared to electrons, muons have a 207 times greater mass, resulting in a suppression of the synchrotron radiation of factor 10^9 ($\approx m^4$). Therefore muons can reach the same energy of electrons with smaller colliders. By way of an example, muons in the LHC ring bent by a 16 T magnetic field will collide at $\sqrt{s} = 14$ TeV while electrons only at 0.2-0.4 TeV [203].

Compared to protons, instead, the advantages arise from the fact that muons are elementary particles and protons are not. Proton-proton collisions involve the scattering of partons that carry only a fraction of the available energy as shown in Eq. (3.1). Figure 5.1 compares hadron and muon collider potential in the neutral current annihilation process for one (left) and two (right) particles in the final state. The equivalent proton collider energy is defined, for a fixed $E_\mu = \sqrt{s_\mu}$, as the corresponding $\sqrt{s_p}$ such as $pp \to X$ has the same cross section as $\mu^+\mu^- \to X$ ($\sigma_p = \sigma_\mu$). For $2 \to 1$ processes the cross sections σ_μ and σ_p are expressed in terms of the partonic cross sections $[\hat{\sigma_\mu}]$ and $[\hat{\sigma_p}]_{ij}$ with ij partons participating in the process. At the muon collider $[\hat{\sigma_\mu}] = \sigma_\mu(s_\mu)$, while for protons all combinations of partons have to be accounted for. The equivalent proton collider energy is shown

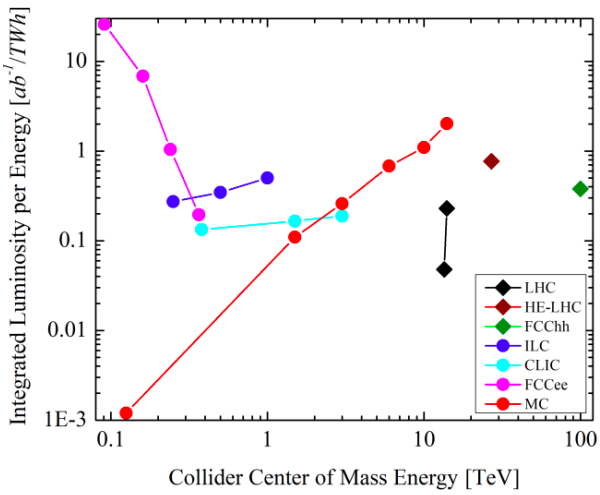

Figure 5.2: Annual integrated luminosity per TeraWatt hour of electric power consumption as a function of the center-of-mass energy. The effective energy reach of hadron colliders (LHC, High Energy-LHC and FCC-hh) is approximately a factor of seven lower than that of a lepton collider operating at the same energy per beam [211].

in Figure 5.1 (left) as a function of E_μ for $ij = gg$ (red) and $ij = q\bar{q}$ (blue). Different benchmarks assumptions on

$$\frac{1}{\beta} = \frac{[\hat{\sigma_\mu}]}{[\hat{\sigma_p}]}$$

are considered with the purpose of covering different coupling regimes. In fact, for example, $\beta = 10$ means that $ij \to X$ is governed by QCD and $\mu^+\mu^- \to X$ by QED. The σ_p is linear to σ_μ for all ij and benchmarks and, in general, a proton collider needs more energy than a muon collider to reach the same potential. As way of an example, for $q\bar{q}$ annihilation with $\beta = 1$ $\sqrt{s_p} = 5\sqrt{s_\mu}$ so a muon collider of 10 TeV has the same physics reach as a 50 TeV hadron collider.

For $2 \to 2$ processes, assuming $\sqrt{s_\mu}$ slightly above the threshold and adding some approximations, the equivalent proton energy is shown in Figure 5.1 right. The leading order production of top squarks and charginos pairs are also considered. As before, the linearity is maintained but the scaling is different: higher energy is needed by a proton collider to achieve the same reach as a muon collider. For $ij = q\bar{q}$ and $\beta = 1$ $\sqrt{s_p} = 22\sqrt{s_\mu}$.

Furthermore, Figure 5.2 highlights another important advantage of a muon collider which was also underlined by the European Strategy for Particle Physics. The electric power efficiency, defined as the collider annual integrated luminosity divided by the facility annual use, is shown. Already at 2 TeV a muon collider is the most efficient option. Moreover, the luminosity increases linearly with the center-of-mass energy and this drives a broad physics case.

5.2 The physics case of a multi-TeV Muon Collider

In the last few years, a wealth of phenomenological explorations have clearly indicated how rich the physics program of a multi-TeV machine will be. As already pointed out in the previous section, the luminosity is increasing with the center-of-mass energy (Fig. 5.3). Assuming as benchmarks reactions induced by EW interactions with cross section:

$$\sigma = \left(\frac{10\,\text{TeV}}{\sqrt{s_\mu}}\right)^2 \cdot 1\,\text{fb},$$

and requiring 10^4 events to carry out precision measurements at per cent level, a rough estimation of the required integrated luminosity is:

$$\mathcal{L}_{int} = \frac{N}{\sigma} = 10\,\text{ab}^{-1}\left(\frac{\sqrt{s_\mu}}{10\,\text{TeV}}\right)^2.$$

Therefore, $\mathcal{L}_{int} = 1\,\text{ab}^{-1}$ and $\mathcal{L}_{int} = 10\,\text{ab}^{-1}$ are assumed for a 3 TeV and 10 TeV muon collider, respectively. In the last case, five years of operations are required to reach the target integrated luminosity. Thus, a muon collider is a time-compact solution.

The last advantage in addition to physics potential, luminosity-energy relation and compactness is the possibility to probe both s-channel reactions for energetic final states and vector boson fusion for large production rate, SM coupling measurements and discovery of light and weakly interacting particles. The program spans from precision Higgs physics to muon-specific opportunities passing through BSM searches. A full report can be found in Refs. [214, 213, 215, 216].

As far as the Higgs sector is concerned, different center-of-mass energies can address distinct questions:

- a 125 GeV factory would allow, through resonant s-channel, the direct determination of Higgs boson width and Yukawa coupling with muons at unprecedented precision,
- a 3 TeV-1 ab^{-1} machine will overcome the HL-LHC potential in single Higgs coupling,
- a 10 TeV-10 ab^{-1} collider would have a permille level of precision in the study of the Higgs coupling with W, Z and bottom, and also the trilinear and quartic self-coupling [217, 219, 218].

A muon collider can also offer opportunities specifically related to muons, such as the study of flavour non-universality. A few TeV muon collider is sufficient to discover or disprove the physics responsible for B-anomalies that suggest new physics that couples more strongly to muons than electrons [220].

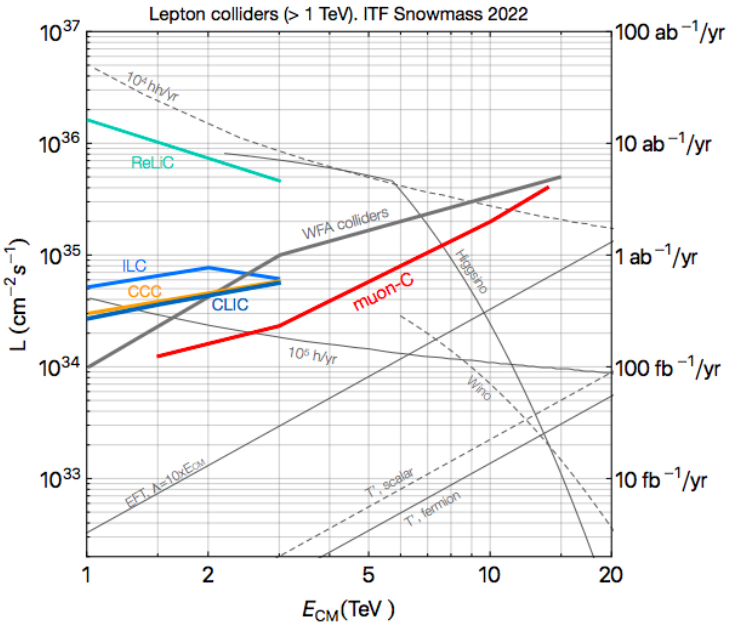

Figure 5.3: Luminosity per IP as a function of center-of-mass energy for the high-energy lepton collider proposals. The right axis shows integrated luminosity for one Snowmass year (10^7 s). Lines corresponding to yearly production rates of important processes and the luminosity requirement for 5σ discovery of the benchmark DM scenarios Higgsino and Wino are also shown. Figure taken from [212].

Moreover, all BSM scenarios where the muon magnetic momentum $g-2$ is generated by a semileptonic interaction between charm quark and muons or by the exchange of EW singlets with mass $m > 1$ GeV can be tested already at 3 TeV [221, 222]. Also, dark matter particles with mass from fractions of TeV to PeV can be investigated for example through direct searches for higgsinos signatures or dark matter in association with SM (e.g. EW bosons).

Some possible results are briefly discussed to confirm the muon collider potential. Figure 5.3 compares high-energy future colliders' proposals to probe different scenarios. The Cool Copper Collider (CCC) is a relatively new proposal to build a Higgs Factory with a 250 GeV energy collision energy based on an accelerator operated at cryogenic temperature to increase radiofrequency (RF) efficiency and the achievable accelerating gradient [223]. The Recycling Linear e^+e^- Collider (ReLiC) would recycle both the particles and used beam energy to increase average beams currents and to reach higher luminosity up to $10^{37}\,\mathrm{cm}^{-2}\mathrm{s}^{-1}$ [224]. The Wake Field Accelerators (WFA) might overcome the limits of RF acceleration to generate high-energy electron beams at a much smaller distance, resulting in more compact machines [225]. For the Higgs sector, the luminosity levels needed to

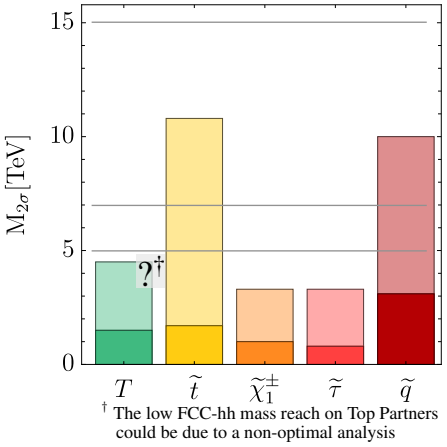

Figure 5.4: Discovery reach of a top partner and several supersymmetric particles. The lightly shaded and darker bars correspond to the 95% CL mass reach of the HL-LHC and FCC-hh as determined for the European Strategy Update briefing book [226]. The tentative discovery reach of a 10, 14 and 30 TeV muon collider are reported as horizontal lines [213].

collect 10^6 Higgs particles and 10^5 pairs in ten years are shown. One of the future colliders' aims is to address the hierarchy problem. Great interest is reserved for top partners (T'), as the top quark plays an important role in the EW symmetry breaking. The luminosity required for 20 events of scalar and fermionic partners is shown. Muon collider would have an excellent reach. For dark matter, a minimal model with fermionic doublet (higgsinos) and triplet (winos) is considered and again the muon collider is promising. Besides, the required luminosity to reach the new physics scale Λ ten times the center-of-mass energy is reported.

Concerning the naturalness, Figure 5.4 reports the 95% confidence level mass reach of a muon collider at different center-of-mass energies (horizontal lines) compared to the one of the HL-LHC and the FCC-hh for the top partner (T) and supersymmetric particles: charginos $\widetilde{\chi}_1^{\pm}$, s-tau lepton $\widetilde{\tau}$ and squarks $\widetilde{q}$. The discovery reach of a 10TeV muon collider exceeds the one of other future machines for all the examined particles.

Finally, a muon collider is an encouraging machine for the study of dark sectors. As way of an example, the production of a dark photon $\mu^+\mu^- \to \gamma X$ has been analysed in Ref. [235]. X can be:

- spin-1 particle (DP) interacting with muons through a magnetic dipole term:

$$\mathscr{L}_{DP} = \frac{1}{2\Lambda}(\bar{\mu}\sigma_{\mu\nu}\mu)F'^{\mu\nu}$$

  with $\sigma_{\mu\nu} = i\left[\gamma^\mu\gamma^\nu\right]/2$;
- spin-0 axion-like particle (ALP) with coupling to photons:

$$\mathscr{L}_{ALP} = \frac{1}{\Lambda}aF^{\mu\nu}\widetilde{F}_{\alpha\beta},$$

  where $\widetilde{F}_{\alpha\beta} = \frac{1}{2}\epsilon_{\alpha\beta\mu\nu}F^{\mu\nu}$ is the dual field strength and ϵ the Levi-Civita tensor.

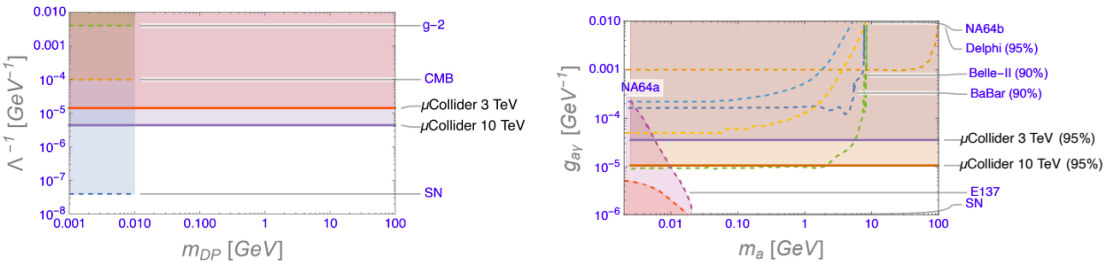

Figure 5.5: Left: Limits on dark photon coupling to muons as a function of the dark photon mass: for SN the scale of the coupling to muons has been set at $10^{4.4}$ [227] by the effect of dark radiation on Supernovae dynamics. For CMB see Ref. [228]. For $g-2$ see Refs. [85, 229]. For masses up to 100 GeV the muon collider limits are for all practical purposes mass independent. Right: Limits on $g_{\alpha\gamma} = 4/\Lambda$ as a function of the ALP mass: NA64a [230], Delphi [231] and Babar [232] are actual limits. Belle-II [108, 233], NA64b [230] and muon collider are future estimates. The limit indicated by E137 is the one from Ref. [234] as modified for a small (10^{-4}) visible branching fraction. Figure is taken from [235].

The limits for a 3 TeV and 10 TeV muon collider are shown in Figure 5.5 with comparisons to other experiments. Lower bounds at 95% confidence level at the lowest energy have been derived corresponding to $\Lambda = 141$ and $\Lambda = 112$ for DP and ALP, respectively. They can rise to $\Lambda = 345$ and $\Lambda = 459$ at the highest energy. Moreover, the muon collider can distinguish between the two spin scenarios. For $\Lambda \sim 300$, in fact, 500 events, collected in five years, are enough to discriminate.

5.3 Muon Collider machine and detector design

In light of the aforementioned advantages, the Internation Muon Collider Collaboration (IMCC) [236] was born to study the feasibility of a Muon Collider. It aims to build a 10 TeV machine with a 3 TeV design as the entry stage. Some tentative target values are reported in Table 5.2. The main limit of such an apparatus arises from the muon short lifetime, $\tau = 2.2\,\mu$s at rest, that corresponds, in the laboratory frame, to:

$$\tau' = \tau\gamma \tag{5.1}$$

with γ relativistic factor. This poses relevant technological challenges in the machine and detector design.

Table 5.2: Tentative target parameters for a muon collider. A complete list of design parameters is reported in Refs. [238, 237].

Parameters	Target values	
Centre-of-mass energy	3 TeV	10 TeV
Circumference	4.5 km	10 km
Muons per bunch	2.2×10^{12}	1.8×10^{12}
Luminosity	$1.8 \times 10^{34}\,\mathrm{cm}^{-2}\mathrm{s}^{-1}$	$20 \times 10^{34}\,\mathrm{cm}^{-2}\mathrm{s}^{-1}$

5.3.1 Accelerator complex

The US Muon Accelerator Program (MAP) made an effort to find a way to accelerate muons [239] . Their idea, the so-called *proton driver scheme*, has been adopted by the IMCC (Figure 5.6 top). A high-intensity bunched proton beam impinges on a heavy metal target generating a few hundred MeV positive and negative pions that decay to muons. The low energy and the large transverse momentum, and consequently emittance, of these tertiary particles require cooling and a quick acceleration before their decay. Cooling is the process of reducing the emittance, i.e. the area occupied by the beam in position-and-momentum phase space, of a charged-particle beam. The Muon Ionization Cooling Experiment (MICE) demonstrated the principle of ionization cooling based on a beam passing through an absorber, like liquid hydrogen or lithium hydride, and losing momentum by ionization [240]. High-gradient RF cavities then restore the longitudinal momentum. Many stages are necessary to reduce the emittance of five orders of magnitude in six dimensions. Muons are then accelerated by a complex of machines, Recirculating Linear (RL) and Fixed Field Alternating Gradient (FFAG) accelerators and Rapid Cycling Synchrotron (RCS), and injected into the collider ring. The 10 TeV is planned to have two collision points.

As already said, the main drawback is related to muon unstable nature:

$$\mu^+ \to e^+ \nu_e \bar{\nu}_\mu \tag{5.2a}$$

$$\mu^- \to e^- \bar{\nu}_e \nu_\mu \tag{5.2b}$$

The effects of electrons and positrons from muon decay are discussed in Section 5.3.2. On the other hand, an intense flux of neutrinos will exit from the ground at a significant distance from the collider. The challenge is to keep this neutrino hazard under control and find synergies with other physics projects that might benefit from high-energy neutrinos [242].

To overcome the problem of cooling and reduce neutrino-induced radiation, muon beams with a small emittance should be used in order to reach the required luminosity with a smaller number of particles. The positron scheme [243], deeply

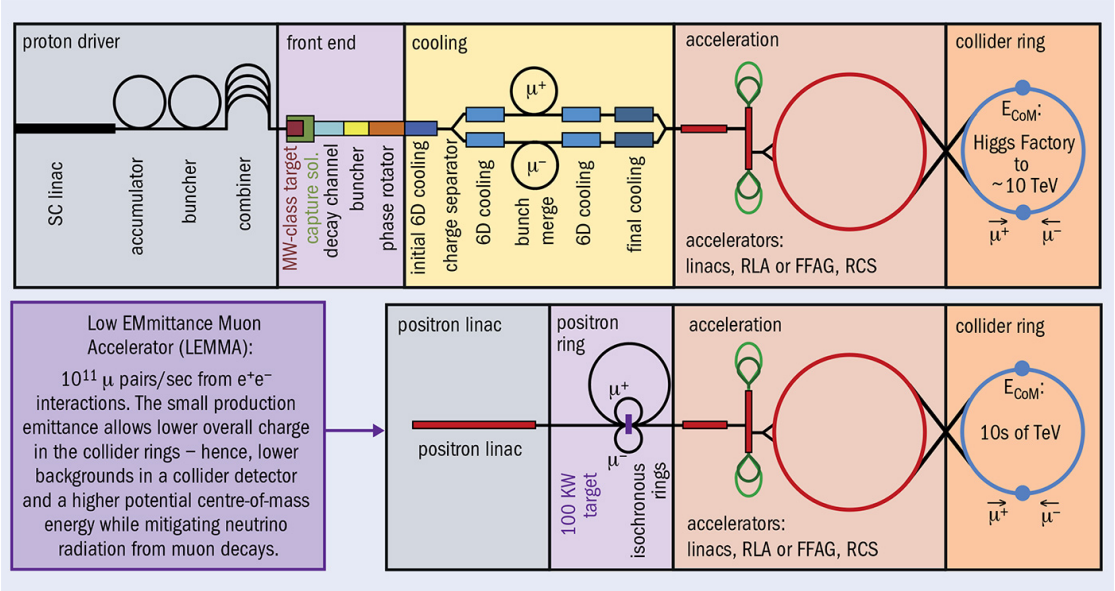

Figure 5.6: Schematic layouts of Muon Collider complexes based on the proton driver scheme and on the positron driver scheme [241].

investigated by the Low EMittance Muon Accelerator (LEMMA) group [244, 245], satisfies these requirements (Figure 5.6 bottom). The idea foresees the production of muons through electron-positron annihilation just above the threshold. An intense beam of positrons at 45 GeV hits on electrons at rest generating muons at 22 GeV that requires no cooling and have a relativistic factor $\gamma = 200$ corresponding to a lifetime $\tau' \sim 500\,\mu s$, as shown in Eq. (5.1), which makes acceleration less challenging. However, a very large positron charge is needed to reach the same luminosity as the proton scheme, so the feasibility is still under study and discussion.

5.3.2 Beam-induced background

Electrons and positrons from the decay of muons in Eq. (5.2), together with synchrotron photons radiated by these primary particles, are a source of background to the experiment: the beam-induced background (BIB). As an example, at 1.5 TeV, the muons have a relativistic factor $\gamma \sim 7100$ and therefore a decay length $\lambda_D = c\tau' = c\tau\gamma \sim 4.7 \times 10^6$ m. Assuming 2×10^{12} muons per bunch (see Table 5.2) there are $\sim 4 \times 10^5$ decays/m [247]. The electron (or positron) brings around 1/3 of the initial energy, i.e. 250 GeV, and radiates photons. From the interaction with the machine components, many particles are produced: charged hadrons, electrons, photons, neutrons and Bethe-Heitler muons. The Bethe-Heitler

Table 5.3: Total number of particles produced in a bunch crossing by the beam muon decays that enter the detector [246].

	Collider energy		
	1.5 TeV	3 TeV	10 TeV
photons	7.1×10^7	9.6×10^7	1.07×10^8
neutrons	4.7×10^7	5.8×10^7	1.01×10^8
electron/positrons	7.1×10^5	9.3×10^5	9.6×10^5
charged hadrons	1.7×10^4	2.0×10^4	4.3×10^4
muons	3.1×10^3	3.3×10^3	4.8×10^3

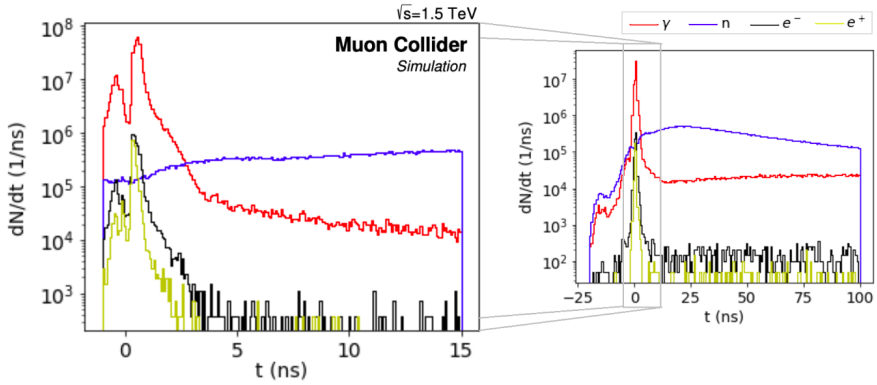

Figure 5.7: Time distribution of BIB particles exiting the machine. The results were obtained with FLUKA, considering the primary negative muon decays within 100 m from the IP [248]. Similar results at 3 TeV are reported in [249].

lepton pair production process is the interaction of a high-energy photon with a nucleus A: $\gamma + A \to A' + \mu^+\mu^-$.

The background level depends, of course, on beam energy and machine detector interface (MDI). Thus, the proper design of the interaction region and MDI is vital for the Muon Collider.

The study of BIB mitigation was first carried out by MAP with the MARS software [250]. Details are available in Refs. [251, 252]. The crucial result was the optimization of a nozzle for 1.5 TeV machine [253]. The nozzle is a double-cone shape tungsten absorber cladded with borated polyethilene located inside the detector in the proximity of the IP. Together with the magnetic field it traps most of the electrons from muons decay and reduces BIB by orders of magnitude. The IMCC is extending the study to higher energy using FLUKA [254, 255] for simulation. The good agreement between the two software has been proved in Ref. [256]. The number of BIB particles produced in each bunch crossing and arriving at the detector after the shielding is reported in Table 5.3. It has been obtained

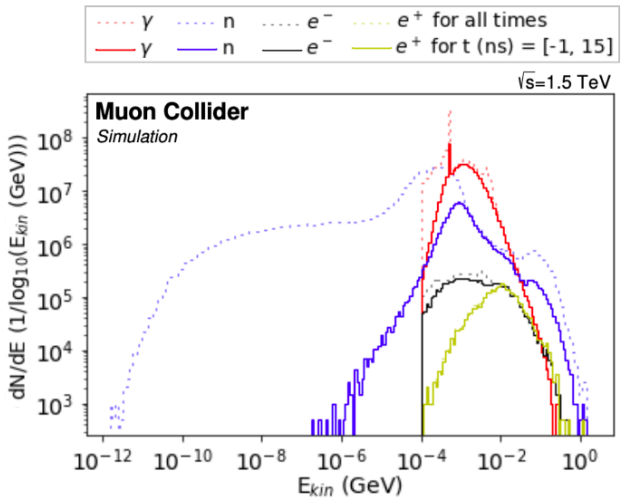

Figure 5.8: Lethargy plot of BIB particles, divided by particle type. No time cut is applied to distributions represented in dotted lines while in solid line only particles exiting the machine between -1 and 15 ns are considered. The results were obtained with `FLUKA`, considering the primary negative muon decays within 100 m from the IP [248]. Similar results at 3 TeV are reported in [249].

fixing the number of muons per bunch at 2×10^{12}. The most distinctive effect is the large multiplicity: $\mathcal{O}(10^8)$ particles exit the MDI in a single bunch crossing. These preliminary results indicate that the high-energy option, i.e. 10 TeV, is not significantly worse even if the incoherent pair production is not negligible. The optimization of the lattice and nozzle is the future target.

Some BIB key features are relevant to the detector design. First of all, the very high flux of photons and neutrons involves significant radiation damage to the detector. Secondly, the BIB time of arrival is spread over several tens of ns, to be compared with 30 ps time spread of $\mu^+\mu^-$ collisions at 1.5 TeV, with the majority around the beam crossing time $t = 0$ (see Figure 5.7). Thus, time-sensitive detectors seem ideal to suppress background. Finally, BIB particles, except neutrons, are very soft. The nozzle, in fact, stops high-energy ones. Only charged hadrons and muons can reach higher energies but their multiplicity is low. In Figure 5.8, energy cut-offs of 100 keV for electrons, positrons, muons and photons, and 10^{-14} GeV for neutrons are applied.

To conclude, BIB simulation is crucial to quantify the requirements for the detector and a careful choice of technologies and reconstruction techniques could help in mitigating the BIB negative effects.

5.3.3 Detector description

The detector geometry currently implemented in the simulation is inherited by CLIC [258, 259] with changes, in particular in the tracker system, to cope with BIB. It is a hermetic detector with 4π coverage, as the CSM apparatus, with the same onion scheme: moving from the IP outwards, it consists of a vertex and

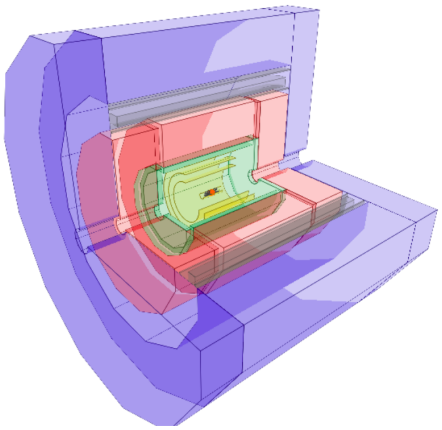

Figure 5.9: Illustration of the full detector, from the `Geant4` model. Different colors represent different subdetector systems: the innermost region, highlighted in the yellow shade, represents the tracking detectors. The green and red elements represent the calorimeter system, while the blue outermost shell represents the magnet return yoke instrumented with muon chambers. The space between the calorimeters and the return yoke is occupied by a 3.57 T solenoid magnet [257].

Table 5.4: Boundary dimensions of individual subsystems of the Muon Collider Detector concept as defined in the current geometry.

Subsystem	Region	R dimensions [cm]	|Z| dimensions [cm]	Material
Vertex detector	barrel	3.0-10.4	65.0	Si
	endcap	2.5-11.2	8.0-28.2	Si
Inner tracker	barrel	12.7-55.4	48.2-69.2	Si
	endcap	40.5-55.5	52.4-219.0	Si
Outer tracker	barrel	81.9-148.6	124.9	Si
	endcap	61.8-143.0	131.0-219.0	Si
ECAL	barrel	150.0-170.2	221.0	W+Si
	endcap	31.0-170.0	230.7-250.9	W+Si
HCAL	barrel	174.0-333.0	221.0	Fe+PS
	endcap	307.0-324.6	235.4-412.9	Fe+PS
Solenoid	barrel	348.3-429.0	412.9	Al
Muon detector	barrel	446.1-645.0	417.9	Fe+RPC
	endcap	57.5-645.0	417.9-563.8	Fe+RPC

tracking system, the ECAL, the HCAL and a 3.57 T solenoid with the return yoke instrumented with muon detectors. Figure 5.9 shows the layout, while Table 5.4 reports the dimensions of all the subsystems, divided, as usual, in a barrel and two endcaps. The coordinate system adopted is equal to the one described in Section 3.2. As already said, tungsten nozzles have been added to absorb BIB. They start from $|z| = 6$ cm and subtend an angle of 10° up to $|z| = 100$ cm. Then, from 100 to 600 cm, the angle is decreased to 5°.

Concerning the inner tracking system, it is made of a vertex detector, an inner and an outer tracker. Due to the nozzle, the acceptance region is limited to $10° < \theta < 170°$. In the innermost layer, 1000 hits/cm^2 are expected from the background, therefore high granularity is mandatory. For comparison, the density of BIB hits is in general, ten times larger than the expected contribution from pileup events at the HL-LHC detector. The vertex consists of four double layers in the barrel and four disks in each endcap of $25 \times 25\,\mu\text{m}^2$ pixel detectors with 50 µm thickness. They ensure a time resolution of 30 ps. Each double layer has two sensitive regions with a 2.2 mm gap. The inner tracker consists of three cylinders in the barrel and seven disks per side of 50 µm × 1 mm macropixels, while the outer tracker is equipped with 50 µm × 10 mm strips arranged in three cylinders and four disks per endcap. They both have a time resolution of 60 ps.

Regarding the calorimeters, which are both sampling, they also require good timing $\sigma_t = 100$ ps and high granularity to reach the goal of separating W and Z bosons in the di-jet channel with 3-4% jet resolution for energies above 100 GeV. The electromagnetic part is made of forty layers of 500 µm thick silicons sensors (cell size = $5 \times 5\,\text{mm}^2$) interleaved with 1.9 mm tungsten plates as absorbers. The total length corresponds to 22 X_0 and 1 λ_I. The hadronic one has sixty layers of 20 mm steel plates with 30 mm plastic scintillators (PS) as the active material for a total of 17.5 λ_I.

Finally, the muon system is placed outside the solenoid with a magnetic field in the barrel of 1.34 T. It is instrumented with seven layers of track-sensitive chambers in the barrel and endcap, respectively. They are interleaved with the iron slabs of the return yoke. The technology chosen to cover an area of 1942 m^2 in the barrel and 1547 m^2 in the endcaps is the glass Resistive Plate Chambers with $30 \times 30\,\text{mm}^2$ cells. Further details are reported in the last section of this chapter.

A detailed description of the current design and a discussion of the promising technologies and R&D directions are available in Ref. [257].

5.4 Physics objects reconstruction

Not only the careful design of the machine and detector but also a judicious choice of reconstruction techniques is necessary to deal with the BIB. A full simulation

is mandatory to access the feasibility of the experiment implementation. This is done within the Muon Collider Software framework [260], mostly based on the `ILCSoft` developed for the International Linear Collider [261]. The tools used are:

- `LCIO` (Linear Collider I/O), a persistency framework that allows to share and compare results of different linear colliders providing a consistent basis for event data storage [262];
- `Geant4`, the toolkit for simulating the passage of particles through matter [263];
- `DD4HEP` to provide the full detector description [264];
- `Marlin`, a generic `C++` application framework for the analysis of `LCIO` data and the full reconstruction of events [265]. Tasks are addressed in a dedicated module called *processor*.

As for the CMS experiment, the idea is to perform particle reconstruction and identification through particle-flow algorithms that aim to reconstruct the four-vector of all detected particles. For charged particles, momentum is measured in the tracking system, while photons and neutrons energies are obtained from calorimeters. The `PandoraPFA` framework has been already tested to study the potential of high-granularity calorimetry at multi-TeV lepton colliders like CLIC [177]. A detailed description of the procedure to build PF objects (PFO) is reported in Refs. [266, 177]. Briefly, the main steps are:

1. study of fundamental elements, i.e. tracks are examined and quality cuts requested to select suitable ones, calibration factors are applied to calorimeter hits;
2. hits clustering with a cone-based forward projective algorithm from the inner to the outermost layer;
3. merging of cluster fragments according to well-established topological rules;
4. matching of clusters with projected tracks;
5. reclustering to improve the track momentum and cluster energy combination;
6. charged hadrons removal and final PFO construction.

It is evident that the entire procedure strongly relies on track reconstruction. Therefore, the approaches that have been investigated up to now are described. A complete discussion of the results obtained for tracks and other physics objects is available at Ref. [248]. As an example, jet reconstruction will be reported. The case of muons will be discussed in the next chapter.

5.4.1 Track reconstruction

Neglecting the energy losses and the multiple scattering, a charged particle in a magnetic field follows a helicoidal trajectory with a radius directly proportional

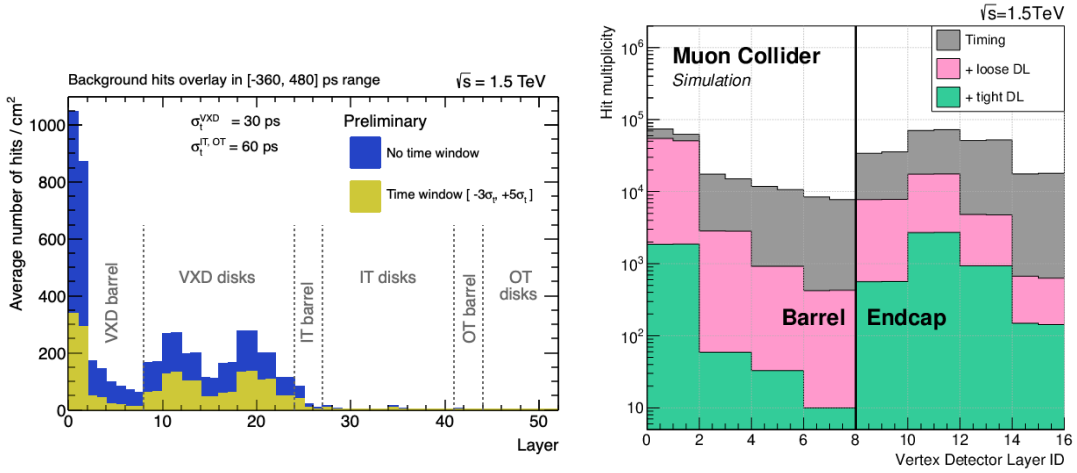

Figure 5.10: Left: Average hit density per bunch crossing in the tracker as a function of the detector layer. Right: Expected reduction of hit multiplicity in the Vertex Detector achieved by applying the loose or tight double-layer filtering [248].

to the transverse momentum and indirectly to the field as in Eq. (3.2). A track is a series of hits in the tracker system layers with five parameters to describe the helix. These are explained in detail in Ref. [267]. In a nutshell, there are two steps for track reconstruction: pattern recognition to identify the hits and fitting procedure to deduce the parameters. Concerning the first, the main obstacle at a Muon Collider comes from the BIB occupancy as already pointed out in the detector description. To reduce the density in the tracker by a factor of 2, a time window $[-3\sigma_t, +5\sigma_t]$ has been applied as shown in Figure 5.10 left. Consequently, the number of hits given as input to the pattern recognition is lessened.

Three different approaches have been studied so far; the first two are based on the Conformal Tracking (CT) developed for the e^+e^- clean environment, while the third one on the Combinatorial Kalman Filter (CKF) especially designed for hadron colliders [268, 269].

CT is a technique using cellular automaton-based track finding [270] performed in a conformally mapped space [271]. All the details are available in Ref. [272]. To further reduce the number of hits used as seeds for tracks two different strategies have been tested: region of interest (ROI) and double-layer filter.

In the first one hits in a certain region are preselected thanks to existing objects in calorimeters and muon system. Figure 5.11 left shows the efficiency as a function of the transverse momentum for single-muon events in the presence of BIB. Three regions in polar angle θ are reported. A muon is considered reconstructed if at least half of the hits associated with the track originated from the true muon, i.e. the one from the MC simulation. The results are excellent except for very forward

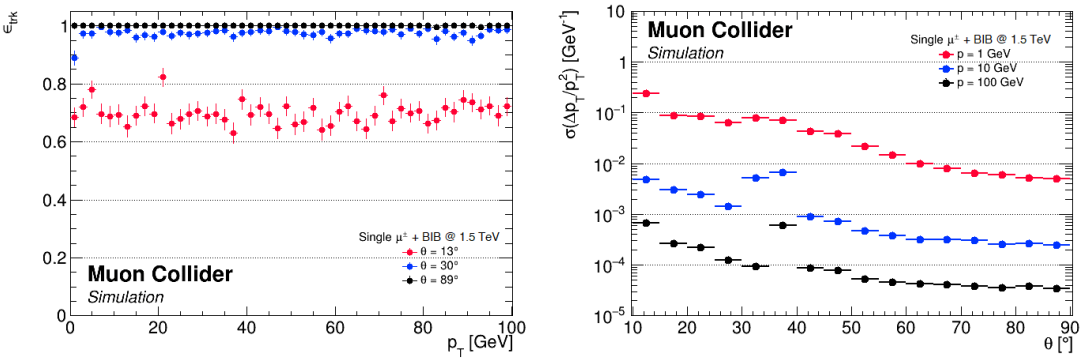

Figure 5.11: Left: Track reconstruction efficiency as a function of p_T for single-muon events overlaid with BIB. Right: Momentum resolution as a function of polar angle for single-muon events overlaid with BIB. CT algorithm with ROI is used [248].

particles (red points) due to the proximity to nozzles and the high occupancy. On the right, the resolution is displayed. It is defined as the standard deviation of a Gaussian function fitted to

$$\frac{\Delta p_T}{p_T^2} = \frac{p_{T,\text{reco}} - p_{T,\text{MC}}}{p_{T,\text{MC}}^2}, \tag{5.3}$$

where the $p_{T,\text{MC}}^2$ at the denominator ensures the independence of the quantity from the transverse momentum itself. This approach takes weeks to reconstruct a single event and it is therefore prohibitive in terms of CPU and memory resources.

The double-layer filter is the one adopted in CMS Phase II [163]. The concept is illustrated in Figure 5.12. The pixel sensors have double-layers (horizontal black lines) crossed by signal particles (green) and BIB (grey). In the first case hit pairs are perfectly aligned with the beamspot and have a sizeable angular difference when measured from the center of the detector. Hit doublets created by BIB, instead, are characterised by larger angular differences due to their shallow crossing angle and displaced origin. Moreover, electrons are usually soft and stop in the first layer. Therefore, the filter selects only hits with a pair in the neighbouring layer aligned with the IP. According to the cuts applied on the azimuthal and polar difference a loose and a tight filter can be applied and Figure 5.10 right shows the expected reduction of hits multiplicity in the two cases. Usually, a two-stage reconstruction is performed: the loose working point is applied to reconstruct high-p_T particles and identify the IP, and then the tight filter allows all tracks reconstruction. However, this technique turns out to be efficient only for prompt muons.

To overcome the limits of the CT with ROI and double-layer filter, a CKF has been implemented using, instead of `ILCSoft`, `ACTS` (A Common Tracking

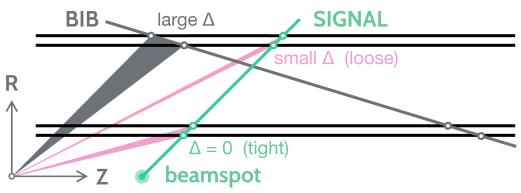

Figure 5.12: Illustration of the double-layer filtering used for the rejection of BIB-induced hits in the Vertex Detector [248].

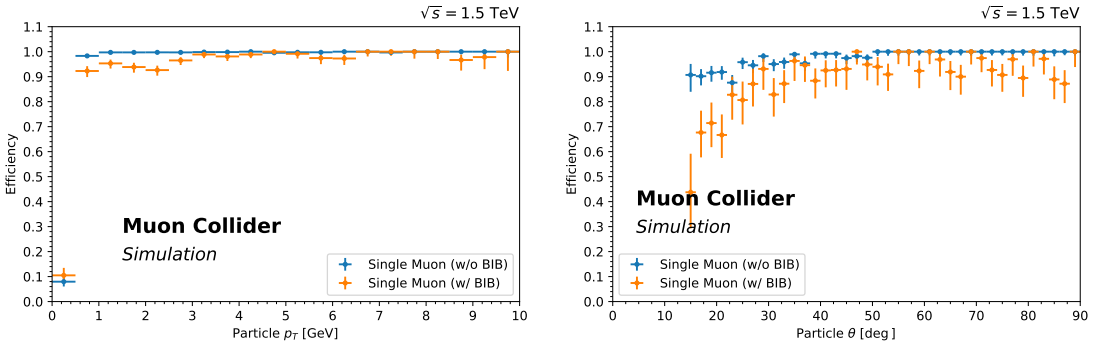

Figure 5.13: Track reconstruction efficiency for events containing a single muon with (blue) and without (orange) BIB overlay as a function of the true muon p_T (left) and of the true muon polar angle (right). CKF technique is used for track reconstruction [248].

System) [273] which is faster. At the moment, the full reconstruction of an event requires only four minutes. This filter calls for a triplet of hits in the outer half of the four layers of the Vertex Detector, and usually around 150000 seeds are created for each event. The algorithm proceeds outwards, even if the possibility of exploiting hits from Outer Tracker, which is less affected by BIB, and moving inwards, is under discussion. The seeding efficiency is full for pT$>$ 2 and the muons are reconstructed with 90% efficiency or greater even in presence of BIB (Figure 5.13).

Jet reconstruction performance

The tracks reconstructed with CKF are the starting point of jet reconstruction. This is a very hard task because requires information from many subdetectors. The `PandoraPFA` algorithm combines tracks with at least three hits in the Vertex Detector and two in the inner tracker together with clusters made of calorimeter hits filtered requiring a precise energy and time window. Jets are then reconstructed from the PFO with the k_t ($n = 1$ in Eq. 3.3) algorithm with R=0.5. The efficiency for b-jets is shown in Figure 5.14 left. To evaluate the performance di-jet events have been used from $H \to b\bar{b}$ and $Z \to \bar{b}b$. The invariant mass distributions have been fitted with a Gaussian curve and the relative width, i.e. the ratio of the standard deviation and the mean, is 27% and 29% respectively.

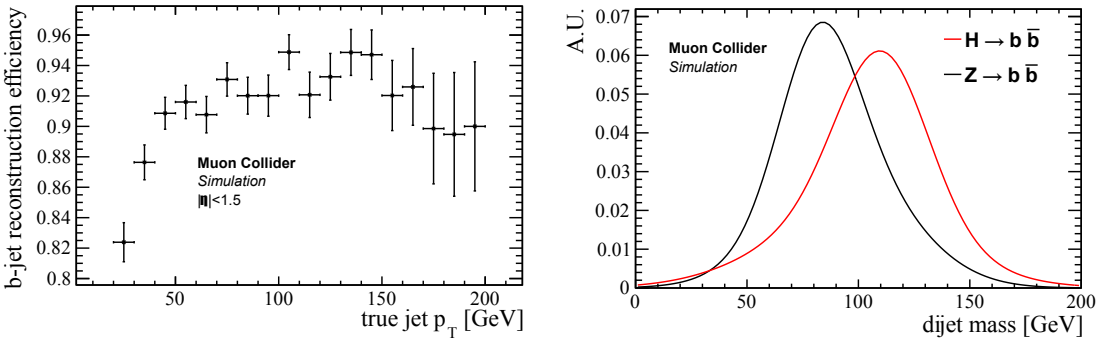

Figure 5.14: Left: Efficiency of b-jets reconstruction as a function of the truth-level jet p_T. Right: Fitted di-jet invariant mass distributions for $H \to \bar{b}b$ and $Z \to \bar{b}b$. The distributions are normalised to the same area [248].

5.5 Design the muon system

The dark-SUSY process considered in this work is characterised by eight muons in the final state. This triggers the interest in the design of the muon spectrometer for a Muon Collider.

So far, the geometry of the muon system foresees the instrumentation of the iron yoke plates with several layers of track-sensitive chambers. The return yoke is made of 8 iron slabs of 24.4 cm thickness in the barrel and 7 slabs 19.7 cm thick in the endcap interleaved with 7 and 6 layers of gaseous detectors respectively. The technology chosen by the CLIC experiment, i.e. glass Resistive Plate Chambers, was implemented in the simulation. The detailed characteristics of the apparatus are reported in Table 5.5. With the solenoid operated at 3.57 T, the magnetic field in the barrel region is -1.34 T in the barrel and decreases rapidly in the yoke endcap (0.01 T).

Table 5.5: Characteristics of the simulated muon system.

	radius [mm]	$\lvert z\rvert$ [mm]	layers	sensor area [m^2]	channels
Barrel	$4461 < r < 6450$	< 4179	7	1942	$2.2\ 10^6$
Endcap	$446 < r < 6450$	$4179 < \lvert z\rvert < 5700$	6	1547	$1.7\ 10^6$

This is the configuration used for the studies on the muon reconstruction techniques reported in Chapter 6.

5.5.1 BIB in the muon system

BIB is mainly due to electrons and positrons from muon decay interacting with the machine components. Since it may degrade detector performance, a proper

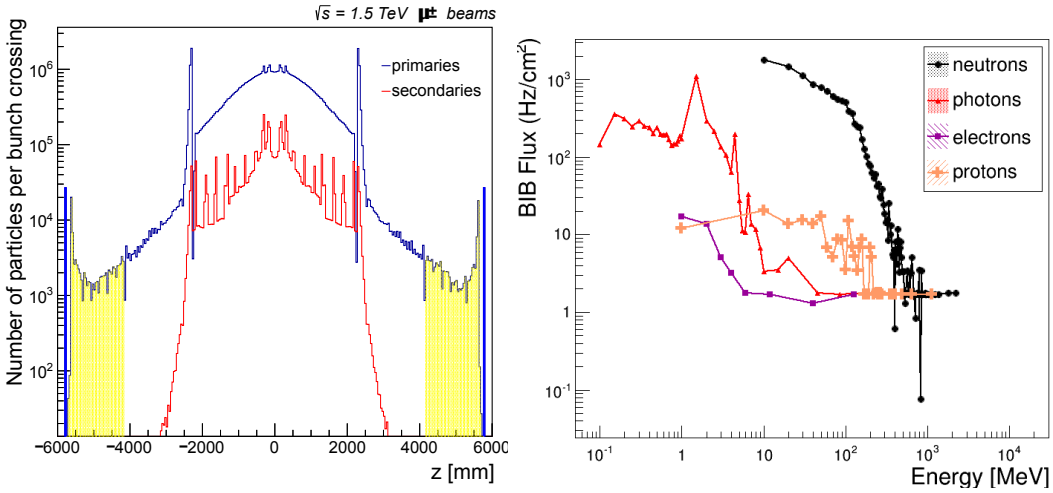

Figure 5.15: Left: z coordinate final position for BIB particles. The first and the last bin in solid blue are the integrals of all particles escaping the detector. The muon system endcaps are highlighted in yellow [274]. Right: Flux of the BIB particles in the entire endcap [275].

detector design has to be considered, as already pointed out in Section 5.3.2. For the muon system, the furthest detector from the interaction point, the situation is not so critical.

Figure 5.15 left shows the final position along the beam axis for BIB particles generated with `MARS` software for a 1.5 TeV machine. Only a small percentage ($\sim$ 8%) of primary particles reaches the muon detector. Here BIB is mainly composed of neutrons and photons, with a small contribution from electrons (Figure 5.15 right). The fluxes for the neutral component are reported in Figure 5.16 for different geometrical regions. Neutrons have energies in the range 10 MeV-2.5 GeV with the majority below 100 MeV, photons energy, instead, extends from 100 keV to 200 MeV with a prevalence below 10 MeV. As expected fluxes are higher in the inner part of the endcap closer to the beamline. This is confirmed by the hits layout.

BIB hits in the cell are characterised by an average energy of 0.14 MeV and a time with respect to bunch crossing smaller than 0.1 ns. This last feature can be exploited to discriminate between BIB and real signals by using detectors with excellent time resolution. Hits are concentrated around the beam axis and therefore barrel is basically almost free from the background. Figure 5.17 on the left shows the distribution in the first layer of the endcap. The region displayed is the central part of the whole layer of 500 $\times$ 500 cells. The term cluster refers to

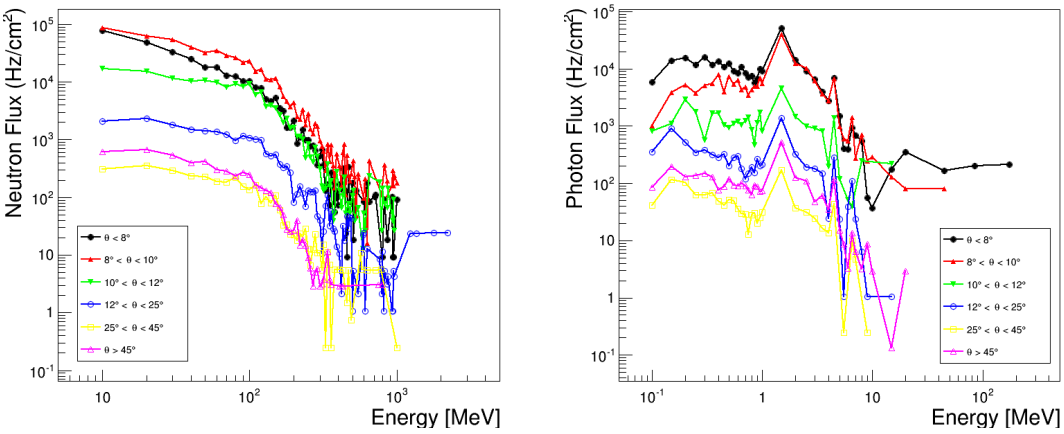

Figure 5.16: Neutron (left) and photon (right) fluxes from BIB in the endcap of the muon system of a muon collider experiment with $\sqrt{s} = 1.5\,\text{TeV}$. Different colors represent different geometrical regions of the endcap [275].

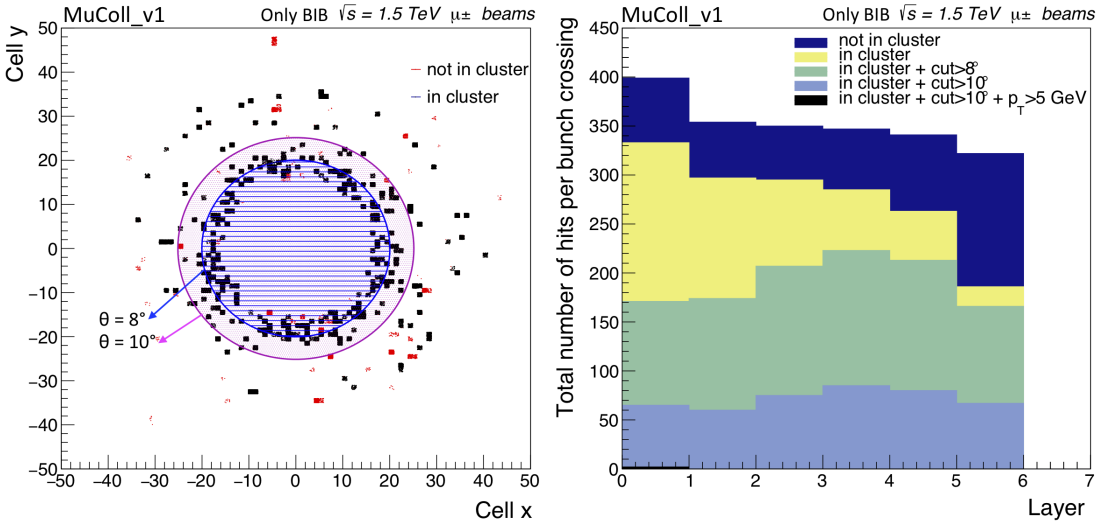

Figure 5.17: Left: BIB muon hit spatial distribution in the first layer of the muon system endcap. In red the hits not associated with a cluster by the `Pandora` algorithm. The blue circle corresponds to region $\theta < 8°$, while the purple to $\theta < 10°$. Right: Number of hits per bunch crossing in each layer of the muon system with different cuts applied [274].

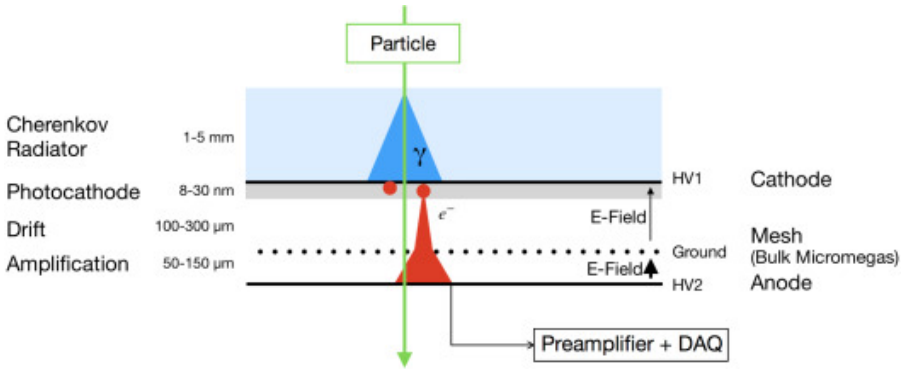

Figure 5.18: The Picosec detection concept [278].

the combination of hits inside a cone and on neighbouring layers performed within the `PandoraPFA` framework (see Section 6.2 for further details). The first results highlight that a geometrical cut on the polar angle combined, for example, with a cut on the track transverse momentum, allows getting rid of almost all the BIB hits in the muon system (Figure 5.17 right).

This low occupancy in the muon system compared to tracker and calorimeters suggests the possibility to use muon objects to seed the global muon reconstruction, as will be discussed in Section 6.4.2.

5.5.2 Considerations about the technologies

Starting from BIB particle fluxes shown in Section 5.5.1, a `Geant4` standalone simulation has been developed to estimate neutrons and photons hit rates for different detectors. The technologies considered are:

- double gap glass RPC as implemented in the current simulation,
- double gap High-Pressure Laminate (HPL) RPC as the classical version of the current detectors [276],
- triple GEM [277],
- Picosec Micromegas [278].

Multigap RPCs are typically used for trigger purposes due to their good time resolution. Their main drawback is related to the spatial resolution and the rate capability limited by the resistivity of the plates. Moreover, the standard gas mixture used to operate them ($C_2H_2F_4$:SF_6) has a high global warming potential and new environmental-friendly mixtures are mandatory for future colliders. MicroPattern Gaseous Detectors (MPGDs), on the other hand, overcome the limit of spatial resolution of RPC because the electrodes are created with photo-lithographic techniques that allow reducing the electrode spacing of one order of magnitude. GEM

Table 5.6: Performance of different technologies.

	time resolution	spatial resolution	rate capability
RPC (HPL or glass)	1 ns	∼1 mm	∼1 kHz/cm^2
MPGD (GEM or MM)	5-10 ns	∼100 µm	∼ 100 kHz/cm^2

detectors and Micromegas (MM) belong to this category [279]. They are characterised by a high rate capability but the time resolution (σ_t) is limited by the fluctuations in the position of the first ionization cluster in the drift gap. In fact, in gas with drift velocity (v_d)

$$\sigma_t = \frac{1}{\lambda v_d}$$

where λ is the average number of primary clusters generated by an ionizing particle inside the gap per unit length [280]. For comparison, the main features of RPC and classical MPGDs are schematised in Table 5.6. A new approach is under study to improve the time resolution of MPGD: the Picosec Micromegas detector. The design is shown in Figure 5.18. A Cherenkov radiator is placed on top of a standard MM with a reduced drift gap of 200 µm. The passage of a charged particle through the Cherenkov radiator produces ultraviolet photons, which are then absorbed in the photocathode and partially converted into electrons. These electrons enter the drift gap avoiding the fluctuations in the position of the first ionization cluster. A time resolution of 24 ps for 150 GeV muons has been obtained [278].

These four types of detectors are simulated in `Geant4` with a basic geometry without electronics, cooling, shieldings, and so forth. `Geant4` allows one to choose among a wide range of physics processes and models. For high-energy hadrons, i.e. for protons, neutrons, pions and kaons above 5-25 GeV, two different string models are applied for the modelling of interactions with nuclei: diffractive scattering (FTF) and quark-gluon string (QGS). The physics list used for this study is the `FTFP_BERT_HP` recommended for a typical high-energy physics collider detector. However, the same results are obtained with the `QGSP_BERT` exploited within the Muon Collider software framework with `Geant4.10.06.p02` version. More details can be found in Ref. [281].

First of all, the sensitivity, i.e. the probability for a BIB particle to generate a visible signal in the detector, is computed as:

$$s = \frac{N}{M},$$

where N is the number of events in which at least one charged particle reaches the sensitive gap and M is the number of incident particles. These are counted by adding a fake layer of air (0.1 mm) on top of the detector. Figure 5.19 shows the results for the different technologies with neutrons and photons. The sensitivity

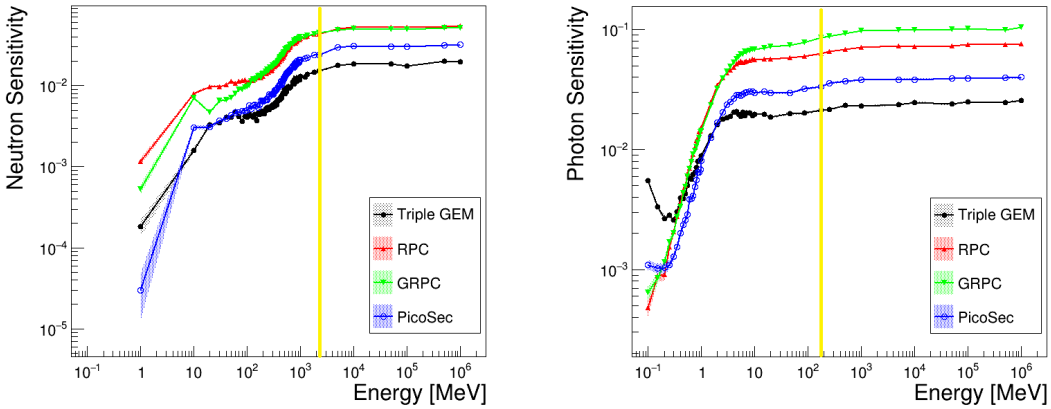

Figure 5.19: Simulated sensitivity to neutrons (left) and photons (right). Different colors represent different gaseous detector technologies considered. The vertical yellow line is the maximum energy reached at $\sqrt{s} = 1.5\,\text{TeV}$, subsequent bins have been simulated in view of the planned center-of-mass energies [275].

of glass RPC is comparable to the one of standard HPL RPC and it is nearly an order of magnitude higher than MPGD. This is due to the material budget. RPC, in fact, contain aluminium and hydrogenated compounds (Mylar and HPL) that are absent in GEM. The sensitivity of Picosec is greater than GEM. A possible explanation is the presence of the radiator. The yellow vertical line is the maximum energy reached at 1.5 TeV, the subsequent bins have been simulated as a clue for future planned center-of-mass energies.

The sensitivity is then convoluted with the fluxes shown in Figure 5.16 for each angular region to give the hit rate:

$$HR = f \otimes s.$$

The total hit rate, given by the sum over all energies

$$\text{total } HR = \sum_{E} HR(E),$$

is shown in Figure 5.20. The error for neutrons is higher due to uncertainties in the physics list. As expected, it is lower for MPDGs compared to RPC. Moreover, for RPC the expected hit rate due to BIB is of some kHz/cm^2, already at the limit of the current rate capability. This suggests that different technologies should be considered at least for the endcap region.

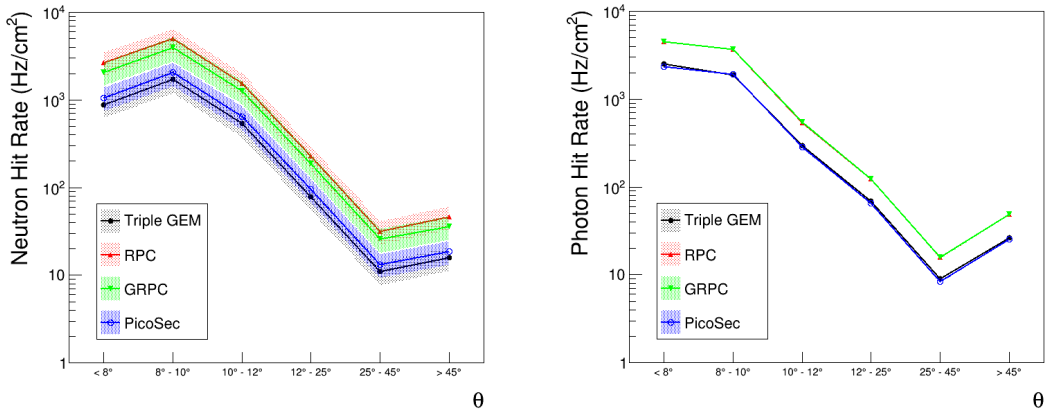

Figure 5.20: Estimated hit rate from neutrons (left) and photons (right) at 1.5 TeV muon collider. Different colors represent different gaseous detector technologies considered [275].

Chapter 6

Dark-SUSY predictions

A preliminary study of the potential of a Muon Collider to the dark-SUSY process analysed so far is reported. A theoretical evaluation of the electroweak background is discussed together with results obtained without the beam-induced background.

The peculiar signature, characterised by eight muons in the final state, suggests this as a benchmark for muon reconstruction. This chapter summarises the different strategies tested without and with the beam-induced background.

6.1 Samples

To evaluate the sensitivity to the dark-SUSY channel in Figure 2.3 at a future Muon Collider (protons replaced by muons) operating at a center-of-mass energy of 3 TeV, different sources of background and parameters choice have been analysed with respect to the CMS experiment.

The 3 TeV machine is expected to work with an instantaneous luminosity of $1.8 \times 10^{34}\,\mathrm{cm^{-2}s^{-1}}$ and to reach $1\,\mathrm{ab^{-1}}$ in about five years of operations.

6.1.1 Signal

As already pointed out in Section 2.2.2, the $\widetilde{N}_1$ mass is set to 96.69 GeV corresponding to a neutralino pair production cross section of $13.36\,\mathrm{fb^{-1}}$. This allows for broadening the H_d mass range. Moreover, the kinematics is different from the CMS experiment since the center-of-mass energy is fully available and muons are boosted. Figure 6.1 compares the muon transverse momentum and polar angle distributions for the same H_d and γ_d masses at the CMS (blue histograms) and Muon Collider (red histograms). Therefore, also a small mass of the dark photon

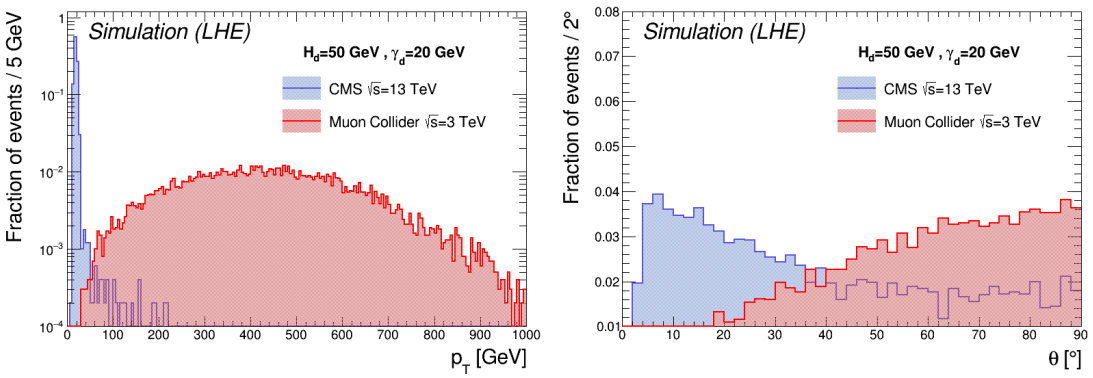

Figure 6.1: Muon transverse momentum (left) and polar angle (right) distributions at the CMS experiment with center-of-mass energy 13 TeV and Muon Collider running at 3 TeV.

Table 6.1: Signal datasets. The cross section has been evaluated for a neutralino mass of 96.68 GeV assuming the branching ratios $\mathcal{B}(\widetilde{N}_1 \to n_d H_d)$ and $\mathcal{B}(H_d \to \gamma_d \gamma_d)$ equal to 1.

N_1 mass (GeV)	H_d mass (GeV)	γ_d mass (GeV)	Cross section (pb)
96.69	30	0.5	2.62×10^{-4}
96.69	30	2.5	2.73×10^{-5}
96.69	30	10	5.11×10^{-6}
96.69	50	10	5.11×10^{-6}
96.69	50	20	4.22×10^{-6}
96.69	70	10	5.11×10^{-6}
96.69	70	20	4.22×10^{-6}
96.69	70	30	3.75×10^{-6}

($m_{\gamma_D} = 0.5$ GeV) has been investigated. The mass of the dark neutralino is kept set to 1 GeV. The complete list is reported in Table 6.1 with the cross section values evaluated according to Eq.(2.5), assuming $\mathcal{B}(\widetilde{N}_1 \to n_d H_d)$ and $\mathcal{B}(H_d \to \gamma_d \gamma_d)$ equal to 1.

The event generator `MadGraph` is used to simulate the process under consideration at LO. The full simulation is performed without BIB overlay with `ILCSoft`. For muon reconstruction, the details are reported in Section 6.2.

Table 6.2: $a\cdot$ (muon pairs) + $b\cdot$ (Z bosons) background samples.

a	b	σ (fb)	$\sigma \times BR$ (fb)
3	1	1.64×10^{-5}	5.41×10^{-7}
2	2	3.13×10^{-4}	3.41×10^{-7}
1	3	1.65×10^{-3}	5.95×10^{-8}
0	4	3.10×10^{-3}	3.68×10^{-9}

6.1.2 EW background

For the CMS experiment, the majority of the background arises from the combination of pileup muons. Some QCD processes with many muons in the final state were considered, but they are rejected after the application of proper cuts. At a lepton machine, SM EW physics channels may play a significant role, thus their contribution is evaluated. However, the MC event generators currently available show limitations when the multiplicity of the particles in the final state is high (≥ 6) and require a meticulous selection of kinematics cut to let the integration converge.

To have a hint of the contribution of these processes, the case of

$$a \cdot (\text{muon pairs}) + b \cdot (\text{Z bosons})$$

has been simulated with `Whizard` [282, 283]. Factors a and b are properly selected to give eight muons in the final state. b is forced to be > 0 to reduce the multiplicity. For this reason, neutrinos are not added even if the signal presents missing energy as a signature. The results are shown in Table 6.2, where σ is the cross section of the process $\mu^+\mu^- \to a \cdot (\mu^+\mu^-) + b \cdot Z$ and the branching ratio $\mathcal{B}(Z \to \mu^+\mu^-)$, equivalent to 3.3%, is taken into account in the last column. It is clear that processes with a cross section of $\mathcal{O}(10^{-7}\,\text{fb})$ require $10^4\,\text{ab}^{-1}$ of integrated luminosity for a single event, a value that is far above the tentative target of $1\,\text{ab}^{-1}$. Therefore, these backgrounds are negligible.

Another check that has been done concerns the production of the double Higgs. In fact, to let the integration converge more easily for the above processes, the Higgs boson resonance has been skipped requiring the invariant mass of four muons, or two muons plus a Z boson, not to be between 124 and 126 GeV.

The double Higgs production ($\mu^+\mu^- \to HH\nu_\mu\bar{\nu}_\mu$) has been generated with `Whizard` at 3 TeV center-of-mass energy. The resulting cross section is 0.84 fb. However, multiplying for the branching ratio $H \to 4\mu$, which is equivalent to 2.85×10^{-5}, it comes down to 6.8×10^{-10} fb which will give no events with $1\,\text{ab}^{-1}$ integrated luminosity. Thus, also this contribution is negligible.

6.2 Muon reconstruction

Given the high multiplicity of muons in the final state, a great deal of effort has been put into their reconstruction. The CT algorithm described in Section 5.4.1 has been used to reconstruct muon tracks that are fundamental elements of the `PandoraPFA New` algorithm. This new version, adopted in `ILCSoft` for muons, is based on an inward projective reconstruction, performed according to four main steps:

1. identification of yoke track candidates,
2. extrapolation of inner tracks to the muon system,
3. matching of inner tracks and yoke tracks,
4. identification of muon hits in the calorimeters.

The details are reported in Ref. [284]. Briefly, a cone-based clustering algorithm is used to identify tracks of muon hits. A cluster, i.e. a collection of hits inside a cone on neighbouring layers, is promoted to yoke track if it satisfies some requirements on the minimum number of occupied layers and on the difference between the last and the first layer number (both set to 5 for the studies of this section). The inner track reconstructed with CT is then extrapolated to the muon system using a helix and, in order to match it with the yoke track, two variables are calculated:

- the distance of the closest approach of the helix to the centroid of the cluster, i.e. the mean position of the hits in the innermost layer of the yoke track
- the cosine of the angle between the helix at the entry point in the muon system and the track.

The first is set to 200 mm and the second to 0.98. At this level, the minimum energy of the candidate track can be selected through a parameter that is initially set to 0.1 GeV and then increased to 7 GeV. Finally, all the hits in the calorimeters are identified.

The result obtained for single muons generated with a polar angle in the range $8° < \theta < 172°$ and p_T up to 1 TeV are shown in Figure 6.2 and 6.3. Efficiency is defined as the fraction of generated particles associated with a cluster, i.e. reconstructed by the `Pandora` algorithm. It is higher than 99% for $p_T > 10$ GeV and higher than 98% in the considered angular region. The results are comparable with the ones obtained by CLIC. The resolution as defined in Eq. (5.3) is less than $10^{-4}\,\text{GeV}^{-1}$ for $p_T > 30$ GeV and better in the barrel region ($45° < \theta < 135°$) compared to the endcap where the magnetic field is basically absent and is difficult to measure the curvature of trajectories.

The same reconstruction approach has been tested for physics channels. Figure 6.4 on the left shows the efficiency for the reconstruction of the four muons

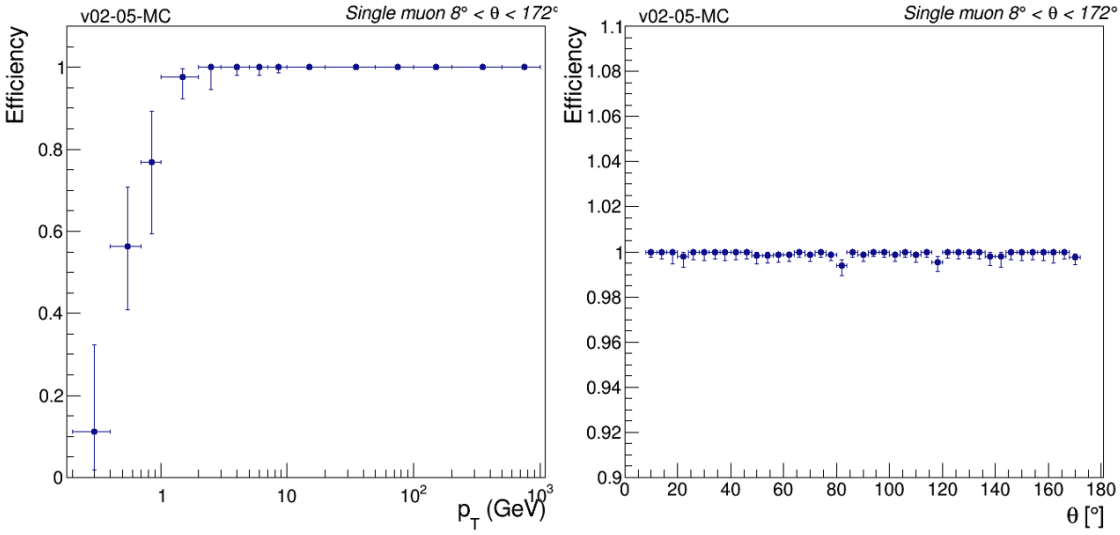

Figure 6.2: Muon reconstruction efficiency as a function of transverse momentum (left) and polar angle (right) for a single muon. Results obtained with CT standard technique for tracks and the `Pandora` algorithm [274].

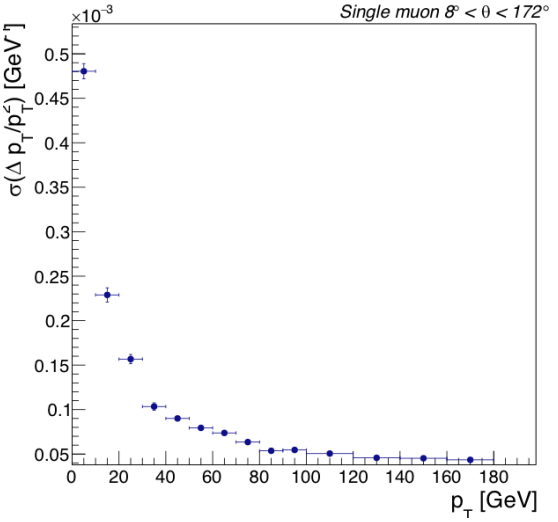

Figure 6.3: Momentum resolution as a function of the transverse momentum for single muons without BIB. Results obtained with CT standard technique for tracks and `Pandora` algorithm [274].

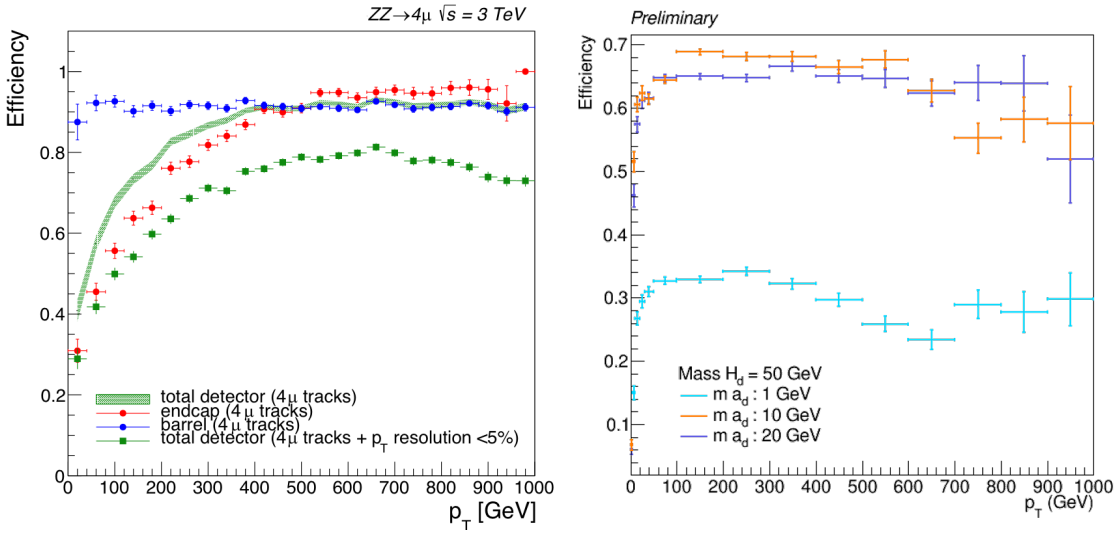

Figure 6.4: Muon reconstruction efficiency as a function of transverse momentum for two Z bosons decaying into muons (left)[274] and dark-SUSY channel with eight muons in the final state (right) [285]. Results obtained with CT standard technique for tracks and the `Pandora` algorithm.

from the decay of two Z bosons generated at 3 TeV center-of-mass energy. The green band is the efficiency for the total detector, while the blue and red points represent the one for the barrel and endcap respectively. It is evident that efficiency is driven by the performance of reconstruction in the endcap region. Green points depict the total efficiency adding the request that the percentage difference between reconstructed and generated transverse momentum is lower than 5%. On the right, the case of the dark-SUSY channel is portrayed. Reconstruction efficiency for all the eight leptons at small dark photon mass ($m_{\gamma_D} = 1\,\text{GeV}$) is low because the majority of muons has a small transverse momentum ($p_T < 10\,\text{GeV}$) or is outside geometrical acceptance.

In general, in absence of the BIB, muon reconstruction is quite straightforward and the results are as a whole satisfactory.

6.3 Analysis strategy and preliminary results

As already discussed in Section 6.1.2, the background is negligible. The selection algorithm is designed to pair muons by exploiting the symmetry of the event. The steps are the following:

- among all the reconstructed muons, the first eight with higher transverse

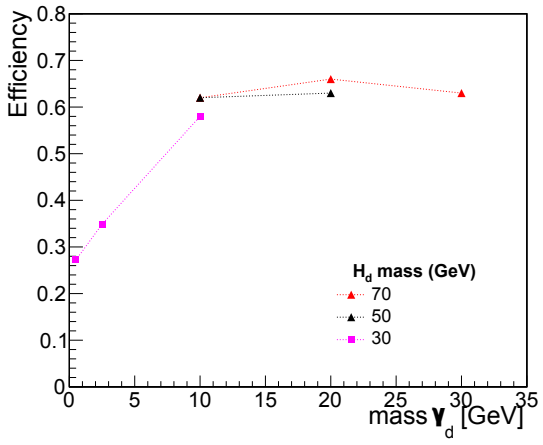

Figure 6.5: Efficiency for signal samples. Efficiency is defined as the fraction of events selected by the algorithm in a defined mass region.

momentum are selected and paired according to the charge, and then two pairs are associated if they satisfy the condition for mass compatibility given by:

$$\frac{|m_{(\mu\mu)1} - m_{(\mu\mu)2}|}{\frac{1}{2}(m_{(\mu\mu)1} + m_{(\mu\mu)2})} < 0.2, \tag{6.1}$$

where $m_{(\mu\mu)}$ is the muon pair invariant mass. This is based on the assumption that the dark photons from which the muon pairs originate decay in the same way.

- If the four muon pairs respect Eq. (6.1), a similar cut is applied to the quartets:

$$\frac{|m_{(\mu\mu\mu\mu)1} - m_{(\mu\mu\mu\mu)2}|}{\frac{1}{2}(m_{(\mu\mu\mu\mu)1} + m_{(\mu\mu\mu\mu)2})} < 0.2, \tag{6.2}$$

assuming again that the dark Higgses decay in the same way.

This algorithm is independent of the masses of dark photons and dark Higgs. To evaluate the acceptance of this criterion, the number of events inside a mass region that pass all the requests in the above list are counted. The mass region is defined in Eq. (4.3). The efficiency is shown in Figure 6.5 as a function of the dark photon mass, and reflects the trend observed in Figure 6.4 on the right. As expected it reduces at smaller masses because the muon transverse momentum and therefore the resolution on invariant mass decreases.

The event yield is evaluated as $S = \epsilon\sigma\mathcal{L}$ with the values reported in Table 6.2. The results for $\mathcal{L} = 1\,\text{ab}^{-1}$ are shown in Figure 6.6. The higher cross section

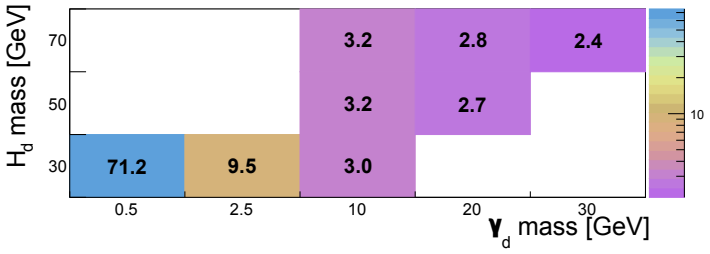

Figure 6.6: Signal yield at an integrated luminosity of $1\,\mathrm{ab}^{-1}$. The cross section σ has been evaluated for a neutralino mass of 96.68 GeV assuming the branching ratios $\mathcal{B}(\widetilde{N}_1 \to n_d H_d)$ and $\mathcal{B}(H_d \to \gamma_d\gamma_d)$ equal to 1.

at smaller masses compensates for the loss in efficiency. The results is obtained assuming no background and neglecting possible systematic uncertainties.

From a theoretical point of view, the neutralino pair is not produced resonantly through the SM Higgs boson, and thus the SUSY uncertainty has to be considered. Furthermore, a full simulation of the irreducible background (eight muons plus two neutrinos) is not possible at the moment due to event generators limitations. Other processes might also be investigated. Moreover, for the signal, initial and final state radiation could affect the sensitivity and the exploitation of a lepton-photon recombination algorithm should be considered.

On the other hand, concerning the experimental systematics uncertainties, a precise luminosity measurement is required and the efficiency may worsen mainly due to the presence of BIB. In this case, the muon reconstruction requires new investigations.

6.4 Further studies for muon reconstruction

In the presence of the BIB, two different strategies have been tested:

- `Pandora` with CKF to reconstruct tracks overcoming the limits of CT
- a standalone muon reconstruction.

6.4.1 `Pandora` combined with Conformal Kalman Filter

In this first case, muons are reconstructed and identified with the `PandoraPFA New` algorithm by matching muon clusters with inner tracks obtained with the CKF approach implemented in `ACTS` (see Section 5.4.1). For single muons with $8° < \theta < 172°$ and p_T up to 50 GeV the efficiency is higher than 95% for $p_T > 15$ GeV

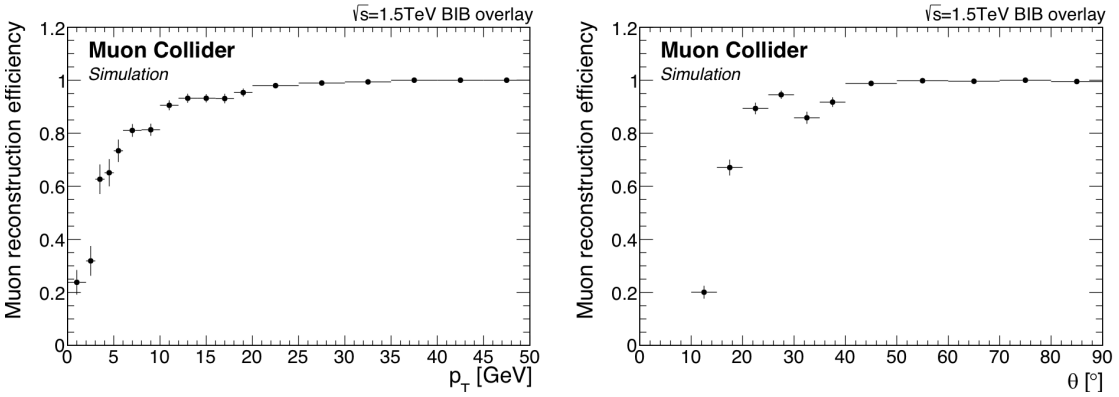

Figure 6.7: Muon reconstruction efficiency as a function of transverse momentum (left) and polar angle (right) for single muons overlaid with BIB. Results obtained with the CKF technique for tracks and `Pandora` algorithm [286].

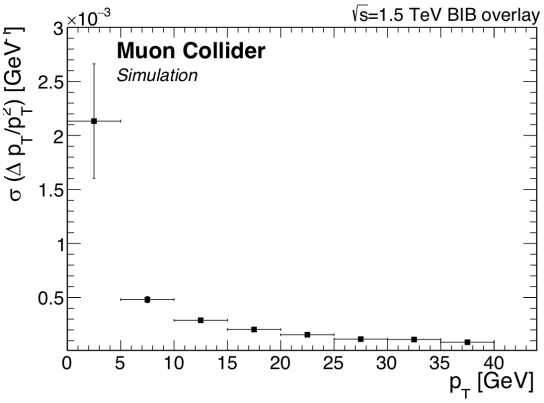

Figure 6.8: Momentum resolution as a function of the transverse momentum for single muons overlaid with BIB. Results obtained with the CKF technique for tracks and `Pandora` algorithm [286].

and higher than 99% for $p_T > 20\,\text{GeV}$ (Figure 6.7 left). It is greater than 99% in the barrel region (Figure 6.7 right). The inefficiency in the endcap is due to the CKF technique limit, as evident in Figure 5.13. The resolution is again less than $10^{-4}\,\text{GeV}^{-1}$ for $p_T > 5\,\text{GeV}$ (see Figure 6.8).

The results for single muons are excellent and compatible with the ones obtained without BIB overlaid. However, some issues have arisen for physics channels with multi-muons in the final state, suggesting that an optimization of the approach is required. By way of example, a preliminary study of $h \to ZZ* \to \mu^+\mu^- 2j$ at 3 TeV center-of-mass energy shows an efficiency of 80% for single muon reconstruction [287].

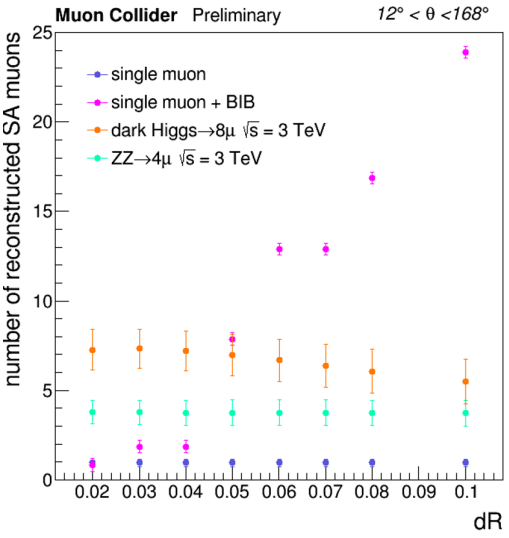

Figure 6.9: Number of reconstructed standalone (SA) muons as a function of cone aperture ΔR for different physics channels [288]. Blue and pink points represent the case of a single muon without and with BIB overlaid respectively. In orange the case of the dark-SUSY channel with eight muons expected. In teal the case of two Z bosons decaying in four muons.

6.4.2 Standalone muon processor

As already pointed out BIB occupancy in the muon system is low and therefore standalone (SA) muon objects can be used to seed the global muon track reconstruction. The new `Pandora` algorithm itself proceeds with an inward projective approach but is fully driven by the tracker where BIB hit density is enormous. Thus a new processor, which is the module of the `Marlin` framework to address tasks, has been developed to clusterize hits in the muon system.

The most energetic hit in the first layer is used as a seed for the SA track. A cone is opened in the direction given by the straight line connecting the hit with the detector center. The angular aperture of the cone ($\Delta R_\mu = \sqrt{\Delta\phi^2 + \Delta\eta^2}$) is an adjustable parameter of the processor. Hits on other layers inside the cone are added to the cluster. At least hits on five layers are required. The average position of hits weighted with energy is stored. A cone in the direction given by the straight line connecting the detector center and this barycentre is opened with an angular aperture ΔR_t. This allows for identifying an ROI for the CT algorithm. Vertex Detector, Inner Tracker and Outer Tracker hits in the cone are filtered. At the moment no information from ECAL and HCAL is used.

Figure 6.9 shows the number of reconstructed SA muons as a function of the angular aperture ΔR_μ for different samples. In the case of a single muon with BIB overlaid only a SA muon has to be reconstructed and this requires an angular aperture $\Delta R_\mu = 0.02$. To maximise track purity and mitigate BIB contamination ΔR_t has been set to 0.05.

Two different samples have been used to evaluate the performance of this processor:

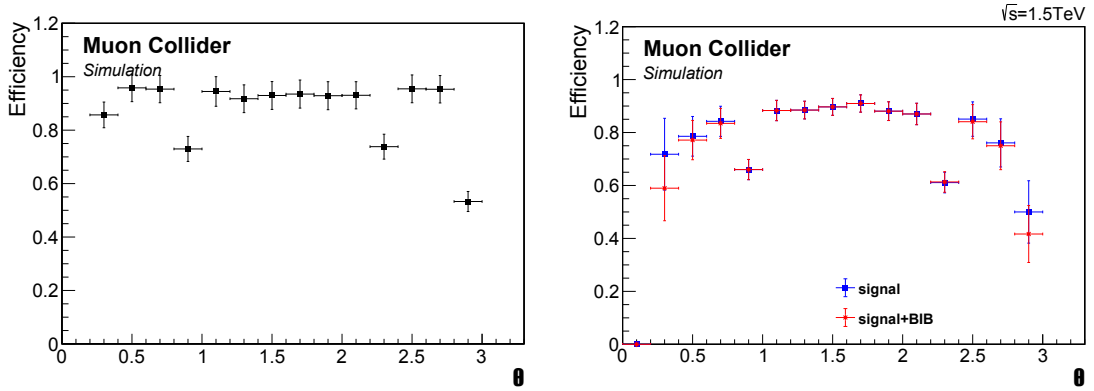

Figure 6.10: Muon reconstruction efficiency as a function of the polar angle in a sample of single muons with no BIB overlaid (left) and in a sample with multi-muons in the final state both with and without BIB (right). Results obtained with the SA algorithm.

- single muons with transverse momentum uniformly distributed in the range 100 MeV-700 GeV and polar angle $8° < \theta < 172°$ with no BIB overlaid
- channel with Higgs and Z bosons resulting in six muons in the final state, generated at 1.5 TeV center-of-mass energy.

Efficiencies in this case are defined as the fraction of generated muons matched to a track within a cone of aperture 0.01. From Figure 6.10 an efficiency loss is evident for low polar angles ($\theta \approx 0$ and π radians) due to the limit of the CT algorithm. The two dips at $\theta \sim 0.8$ and 2.3 rad, equivalent to $\sim 45°$ and $135°$ correspond to the passage between the barrel and endcap. Tracks with hits in both regions required a dedicated approach still under study. Efficiency as a function of the transverse momentum in a region restricted to $15° < \theta < 165°$ has been evaluated in order to avoid the intrinsic limits of CT (Figure 6.11 top). An efficiency greater than 85% is achieved for $p_T > 80$ GeV. for both samples. The drop of the curve at low transverse momentum is due to muons with hits both in the barrel and endcap (as said before their reconstruction will be implemented) and to tracks with high curvature for which the ΔR_μ and ΔR_t have to be tuned and the definition of direction with a straight line instead of a helix is too simplistic.

The muon transverse momentum resolution in Figure 6.11 bottom is comparable with the results obtained with different strategies for both samples. Comparing blue and red curves, which refer to signals without and with BIB respectively, it is evident that the efficiency with BIB is a bit lower in the endcap where all spurious hits are concentrated. The highest efficiency in presence of BIB is a countereffect due to BIB hits wrongly kept by the filter. The results are comparable in the sample with single and multi-muons as the dark-SUSY process.

In conclusion, this out-in approach requires still some work but seems promising

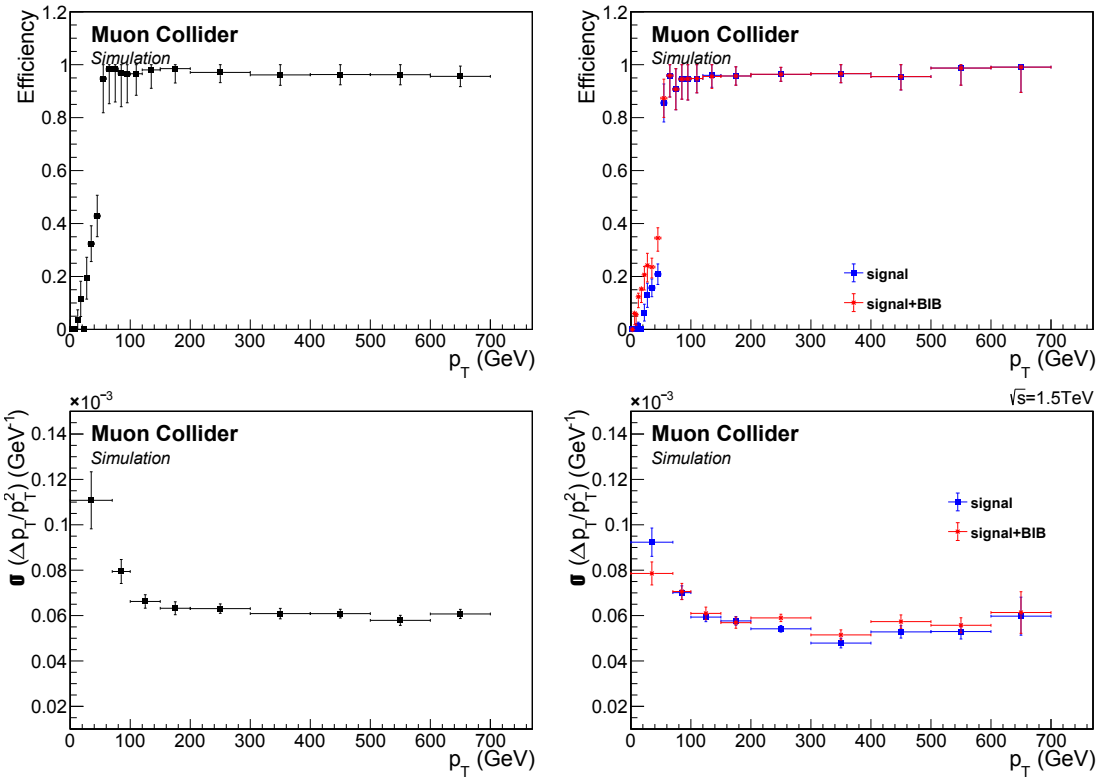

Figure 6.11: Top: Muon reconstruction efficiency as a function of transverse momentum in a sample of single muons with no BIB overlaid (left) and in a sample with multi-muons in the final state both with and without BIB (right). Results obtained with the SA algorithm [289]. Bottom: Muon track transverse momentum resolution as a function of p_T in a sample of single muons with no BIB overlaid (left) and in a sample with multi-muons in the final state both with and without BIB (right). Results obtained with the SA algorithm.

in the case of many muons.

Conclusions

The work presented in this thesis is framed within the studies on physics beyond the Standard Model and, in particular, focuses on the search for hidden sectors. These are possible explanations for the nature of dark matter.

We extended the Minimal Supersymmetric Standard Model dark sector (dark-SUSY) with a dark Higgs boson. This originates from a neutralino and decays into two dark photons that then decay into pairs of muons. In total, starting from neutralino pair production, eight muons are present in the final state of the process analyzed. We studied all the details in collaboration with theoretical colleagues to compute Feynman rules with the `FeynRules` tool and got the model to pass to event generators for the simulation of the process.

As far as the CMS experiment is concerned, the search was carried out on the full dataset collected during 2018 at a center-of-mass energy of 13 TeV, corresponding to an integrated luminosity of $61.3\,\text{fb}^{-1}$. The individuation of possible sources of background required a meticulous analysis. SM processes with eight muons in the final state have such a small cross section that can be neglected. However, the combination of muons from pileup, i.e. simultaneous proton-proton collisions in the same bunch crossing, has to be considered. This requires the addition of cuts on muon quality for the selection algorithm to properly reject no-signal muons. Model independent confidence limits on the cross section have been found.

At the Muon Collider, the dark-SUSY process has been used as a benchmark for muon reconstruction. After the estimate of the contribution of the EW channels as background, some preliminary predictions on the signal yield have been obtained for a machine operating at 3 TeV center-of-mass energy with an integrated luminosity of $1\,\text{ab}^{-1}$ in absence of beam-induced background.

For the muon reconstruction, the standard in-out approach based on Conformal Tracking and the Pandora algorithm was used. Adding the BIB, however, it fails and thus the Conformal Kalman Filter was also studied. Despite being currently the most promising solution, it still needs a lot of work and parameter tuning.

In this context, the standalone algorithm developed in this work may help by providing information to define a region of interest. Such an algorithm would profit from the detector's excellent spatial and time resolution. The results obtained with `Geant4` show that the technology implemented at the moment in the simulation, the glass Resistive Plate Chamber, is already at the limit of its rate capability and thus Picosec proposal is under investigation. These results together with future efforts will reach the performance required to ensure the overwhelming physics program.

Appendix A

MSSM parameters

The parameters for the MSSM given as input to `MadGraph` generator are here reported. The code in the table is in agreement with the MC particle numbering scheme [56]. The strong coupling α_s is set to 0.118, while the fine structure constant α at the Z pole is 1/128. The default value of the neutralino mass is shown, for the analysis in Part I it has been set to 60 GeV.

Table A.1: SM particles masses and widths. Spaces left blank are equivalent to a value of 0 GeV.

particle	code	mass (GeV)	width (GeV)	particle	code	mass (GeV)	width (GeV)
d	1	–	–	ν_μ	14	–	–
u	2	–	–	τ	15	1.78	–
s	3	–	–	ν_τ	16	–	–
c	4	–	–	Z	23	91.2	2.41
b	5	4.89	–	W^+	24	79.8	2
t	6	175	1.56	h^0, H_1^0	25	125	10^{-5}
e	11	–	–	H^0, H_2^0	35	400	0.575
ν_e	12	–	–	A^0, H_3^0	36	400	0.632
μ	13	0.105	–	H^+	37	408	0.547

Table A.2: SUSY particles masses and widths.
a. Particulary in the third generation, the left and right sfermion states may mix, as already shown in Table tab:mssm. The lighter mixed state is given the smaller number.

particle	code	mass (GeV)	width (GeV)	particle	code	mass (GeV)	width (GeV)
$\widetilde{d}_L$	1000001	568	5.31	$\widetilde{\chi}_2^0$	1000023	182	0.021
$\widetilde{u}_L$	1000002	561	5.48	$\widetilde{\chi}_1^+$	1000024	182	0.017
$\widetilde{s}_L$	1000003	568	5.31	$\widetilde{\chi}_3^0$	1000025	364	1.92
$\widetilde{c}_L$	1000004	561	5.48	$\widetilde{\chi}_4^0$	1000035	382	2.58
$\widetilde{b}_1$	1000005[a]	513	3.74	$\widetilde{\chi}_2^+$	1000037	380	2.49
$\widetilde{t}_1$	1000006[a]	400	2.02	$\widetilde{d}_R$	2000001	545	0.28
$\widetilde{e}_L$	1000011	203	0.21	$\widetilde{u}_R$	2000002	549	1.15
$\widetilde{\nu}_{eL}$	1000012	185	0.15	$\widetilde{s}_R$	2000003	545	0.29
$\widetilde{\mu}_L$	1000013	203	0.21	$\widetilde{c}_R$	2000004	549	1.15
$\widetilde{\nu}_{\mu L}$	1000014	185	0.15	$\widetilde{b}_2$	2000005[a]	544	0.80
$\widetilde{\tau}_1^-$	1000015[a]	134	0.148	$\widetilde{t}_2$	2000006[a]	586	7.37
$\widetilde{\nu}_{\tau L}$	1000016	185	0.147	$\widetilde{e}_R^-$	2000011	144	0.22
$\widetilde{g}$	1000021	608	5.51	$\widetilde{\mu}_R^-$	2000013	144	0.22
$\widetilde{\chi}_1^0$	1000022	96.7	10^{-5}	$\widetilde{\tau}_2^-$	2000015[a]	207	0.27

Appendix B

MC signal samples for CMS

B.1 Production

The MC samples for the dark-SUSY signal at the CMS experiment have been generated through the following steps:

	CMSSW release	global tag
GEN	CMSSW_10_6_24	106X_upgrade2018_realistic_v4
SIM	CMSSW_10_6_17_patch1	106X_upgrade2018_realistic_v11_L1v1
DIGI	CMSSW_10_6_17_patch1	106X_upgrade2018_realistic_v11_L1v1
HLT	CMSSW_10_2_16_UL	102X_upgrade2018_realistic_v15
RECO	CMSSW_10_6_17_patch1	106X_upgrade2018_realistic_v11_L1v1
MINIAOD	CMSSW_10_6_20	106X_upgrade2018_realistic_v16_L1v1

Generation

```
cmsDriver.py Configuration/GenProduction/python/B2G-RunIISummer20UL18wmLHEGEN
-01119-fragment.py --python_filename DarkSUSY_LHEGEN_cfg.py --eventcontent RAWSIM
--customise Configuration/DataProcessing/Utils.addMonitoring --datatier GEN
--fileout file:output.root --conditions 106X_upgrade2018_realistic_v4 --beamspot
Realistic25ns13TeVEarly2018Collision --step GEN --geometry DB:Extended --era
Run2_2018 --no_exec --mc -n 5000 --filein file:input.lhe
```

The file in LHE format is the output of `MadGraph` generator. `Pythia8` with `TuneCP5` is used.

Simulation

```
cmsDriver.py --python_filename DarkSusy_SIM_cfg.py --eventcontent RAWSIM
--customise Configuration/DataProcessing/Utils.addMonitoring --step SIM
--conditions 106X_upgrade2018_realistic_v11_L1v1 --fileout file:output.root
--beamspot Realistic25ns13TeVEarly2018Collision --geometry DB:Extended
--datatier GEN-SIM --filein file:input.root --runUnscheduled --era Run2_2018
--no_exec --mc -n 5000
```

Digitization

```
cmsDriver.py --python_filename DarkSusy_DIGI_cfg.py --eventcontent PREMIXRAW
--customise Configuration/DataProcessing/Utils.addMonitoring --datamix PreMix
--pileup_input dbs:/Neutrino_E-10_gun/RunIISummer20ULPrePremix-UL18_106X_
upgrade2018_realistic_v11_L1v1-v2/PREMIX --step DIGI,DATAMIX,L1,DIGI2RAW
--conditions 106X_upgrade2018_realistic_v11_L1v1 --datatier GEN-SIM-DIGI
--fileout file:output.root --procModifiers premix_stage2 --geometry DB:Extended
--filein file:input.root  --era Run2_2018 --runUnscheduled --no_exec --mc -n 5000
```

Trigger

```
cmsDriver.py --python_filename DarkSusy_HLT_cfg.py --eventcontent RAWSIM
--customise Configuration/DataProcessing/Utils.addMonitoring --datatier GEN-SIM-RAW
--fileout file:output.root --conditions 102X_upgrade2018_realistic_v15
--customise_commands process.source.bypassVersionCheck = cms.untracked.bool(True)
--step HLT:2018v32 --geometry DB:Extended --filein file:input.root
--era Run2_2018--no_exec --mc -n 5000
```

Reconstruction

```
cmsDriver.py --python_filename DarkSusy_RECO_cfg.py --eventcontent AODSIM
--customise Configuration/DataProcessing/Utils.addMonitoring --datatier AODSIM
--fileout file:output.root --conditions 106X_upgrade2018_realistic_v11_L1v1
--step RAW2DIGI,L1Reco,RECO,RECOSIM,EI --geometry DB:Extended --era Run2_2018
--filein file:input.root --runUnscheduled --no_exec --mc -n 5000
```

MiniAOD format

```
cmsDriver.py  --python_filename DarkSusy_MINIAOD_cfg.py --eventcontent MINIAODSIM
--customise Configuration/DataProcessing/Utils.addMonitoring --datatier MINIAODSIM
--fileout file:output.root --conditions 106X_upgrade2018_realistic_v11_L1v1
--step PAT --geometry DB:Extended --filein file:input.root --era Run2_2018
--runUnscheduled --no_exec --mc -n 5000
```

The `CMSSW_10_6_24` release has been used for the analysis.

B.2 Results of sensitivity

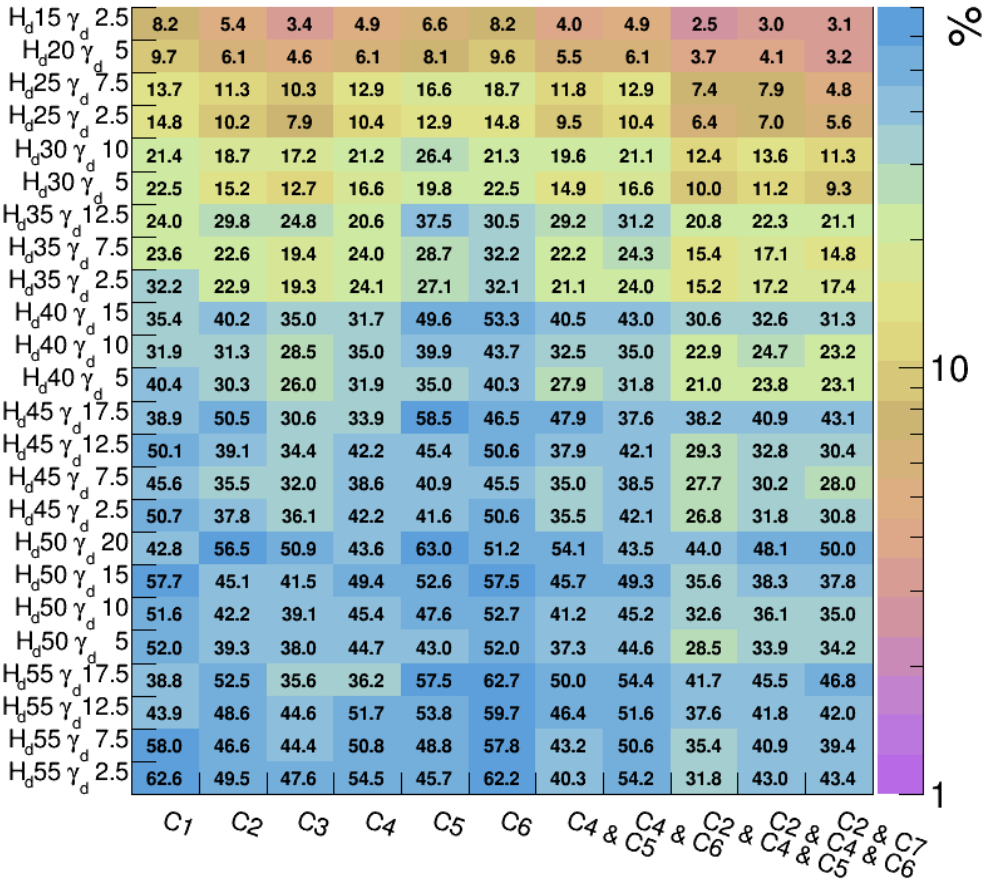

Figure B.1: Sensitivity, as defined in Eq. (4.4) with $a = 1$, for different signal samples and cuts.

List of Acronyms

ACTS A Common Tracking System

ALICE A Large Ion Collider Experiment

ALP axion-like particle

AOD Analysis Object Data

APD avalanche photodiode

ATLAS A Toroidal LHC ApparatuS

BIB beam-induced background

BSM beyond the Standard Model

CCC Cool Copper Collider

CEPC Circular Electron Positron Collider

CERN *Conseil Européen pour la Recherche Nucléaire*

CKF Combinatorial Kalman Filter

CKM Cabibbo-Kobayashi-Maskawa

CL confidence level

CLIC Compact LInear Collider

CMB Cosmic Microwave Background

CMS Compact Muon Solenoid

CP charge-conjugation parity

CSC Cathode Strip Chambers

CT Conformal Tracking

DCA distance of closest approach

DM dark matter

DT Drift Tubes

ECAL electromagnetic calorimeter

EYETS Extended Year-End Technical Stop

EW electroweak

FCC Future Circular Collider

GCT Global Calorimeter Trigger

GEM Gaseous Electron Multiplier

GMT Global Muon Trigger

GSF Gaussian Sum Filter

GUT Grand Unified Theory

HCAL hadronic calorimeter

HGCal High Granularity Calorimeter

HL-LHC High-Luminosity LHC

HLT High Level Trigger

HPL High-Pressure Laminate

ID identification

ILC International Linear Collider

IMCC Internation Muon Collider Collaboration

IP interaction point

ISR initial state radiation

KF Kalman Filter

L1 Level 1 Trigger

LEMMA Low EMittance Muon Accelerator

LEP Large Electron-Positron

LHC Large Hadron Collider

LHCb Large Hadron Collider beauty

LHE Les Houches Event

LO leading-order

LS Long Shutdown

LSP lightest supersymmetric particle

MACHO MAssive Compact Halo Objects

MAP Muon Accelerator Program

MC MonteCarlo

MDI machine detector interface

MET missing transverse energy

MICE Muon Ionization Cooling Experiment

MM Micromegas

MPGD MicroPattern Gaseous Detector

MSSM Minimal Supersymmetric Standard Model

MSSMD Minimal Supersymmetric Standard Model Dark

PAT Physics Analysis Toolkit

PF particle-flow

PFO particle-flow objects

PS Proton Synchrotron

PSB Proton Synchrotron Booster

PU pileup

QCD Quantum Chromodynamics

QED Quantum Electrodynamics

Relic Recycling Linear Collider

RF radiofrequency

ROI region of interest

RPC Resistive Plate Chambers

SA standalone

SM Standard Model

SPS Super Proton Synchrotron

SSB spontaneous symmetry breaking

SUSY supersymmetry

TEC Tracker Endcap

TIB Tracker Inner Barrel

TID Tracker Inner Disk

TOB Tracker Outer Barrel

TP Trigger Primitive

TPB Tracker Pixel Barrel

TPE Tracker Pixel Endcap

UFO Universal FeynRules Output

VBF vector boson fusion

VPCT vacuum phototriode

WFA Wake Field Accelerators

WIMP Weakly Interacting Massive Particle

Bibliography

[1] R. N. Cahn and G. Goldhaber. *The experimental foundations of particle physics*. Cambridge University Press, 2009.

[2] M. Thomson. *Modern particle physics*. Cambridge University Press, 2013.

[3] F. Halzen and A. D. Martin. *Quark & Leptons: An introductory course in modern particle physics*. John Wiley & Sons, 2008.

[4] D. Griffiths. *Introduction to elementary particles*. John Wiley & Sons, 2020.

[5] S. Tomonaga. On a Relativistically Invariant Formulation of the Quantum Theory of Wave Fields. *Prog. Theor. Phys.*, 1(2):27–42, 1946.

[6] J. Schwinger. Quantum Electrodynamics. I. A Covariant Formulation. *Phys. Rev.*, 74:1439–1461, 10, 1948.

[7] R. P. Feynman. Mathematical Formulation of the Quantum Theory of Electromagnetic Interaction. *Phys. Rev.*, 80:440–457, 3, 1950.

[8] C. N. Yang and R. L. Mills. Conservation of Isotopic Spin and Isotopic Gauge Invariance. *Phys. Rev.*, 96:191–195, 1, 1954.

[9] D. J. Gross and F. Wilczek. Ultraviolet Behavior of Non-Abelian Gauge Theories. *Phys. Rev. Lett.*, 30:1343–1346, 26, 1973.

[10] D. J. Gross and F. Wilczek. Asymptotically Free Gauge Theories. I. *Phys. Rev. D*, 8:3633–3652, 10, 1973.

[11] H. D. Politzer. Reliable Perturbative Results for Strong Interactions? *Phys. Rev. Lett.*, 30:1346–1349, 26, 1973.

[12] C. S. Wu et al. Experimental Test of Parity Conservation in Beta Decay. *Phys. Rev.*, 105:1413–1415, 4, 1957.

[13] J. H. Christenson et al. Evidence for the 2π Decay of the K_2^0 Meson. *Phys. Rev. Lett.*, 13:138–140, 4, 1964.

[14] E. Fermi. Tentativo di una teoria dei raggi β. *Il Nuovo Cimento (1924-1942)*, 11(1):1–19, 1934.

[15] S. L. Glashow. Partial-symmetries of weak interactions. *Nucl. Phys.*, 22(4):579–588, 1961.

[16] S. Weinberg. A Model of Leptons. *Phys. Rev. Lett.*, 19:1264–1266, 21, 1967.

[17] A. Salam. Elementary particle theory. In *Prog. Of the Nobel Symposium*, volume 367, 1968.

[18] N. Cabibbo. Unitary Symmetry and Leptonic Decays. *Phys. Rev. Lett.*, 10:531–533, 12, 1963.

[19] M. Kobayashi and T. Maskawa. CP-Violation in the Renormalizable Theory of Weak Interaction. *Prog. Theor. Phys.*, 49(2):652–657, 1973.

[20] P. W. Higgs. Broken Symmetries and the Masses of Gauge Bosons. *Phys. Rev. Lett.*, 13:508–509, 16, 1964.

[21] F. Englert and R. Brout. Broken Symmetry and the Mass of Gauge Vector Mesons. *Phys. Rev. Lett.*, 13:321–323, 9, 1964.

[22] F. Hasert et al. Search for elastic muon-neutrino electron scattering. *Phys. Lett. B*, 46(1):121–124, 1973.

[23] F. Hasert et al. Observation of neutrino-like interactions without muon or electron in the gargamelle neutrino experiment. *Phys. Lett. B*, 46(1):138–140, 1973.

[24] C. Rubbia. Experimental observation of the intermediate vector bosons W^+, W^-, and Z^0. *Rev. Mod. Phys.*, 57(3):699, 1985.

[25] SLD Electroweak and Heavy Flavour Groups. Precision electroweak measurements on the Z resonance. *Phys. Rep.*, 427(5):257–454, 2006.

[26] J. Augustin et al. Discovery of a Narrow Resonance in e^+e^- Annihilation. *Phys. Rev. Lett.*, 33:1406–1408, 23, 1974.

[27] J. J. Aubert et al. Experimental Observation of a Heavy Particle J. *Phys. Rev. Lett.*, 33:1404–1406, 23, 1974.

[28] M. L. Perl et al. Evidence for Anomalous Lepton Production in e^+e^- Annihilation. *Phys. Rev. Lett.*, 35:1489–1492, 22, 1975.

[29] CDF Collaboration. Observation of Top Quark Production in $\overline{p}p$ Collisions with the Collider Detector at Fermilab. *Phys. Rev. Lett.*, 74:2626–2631, 14, 1995.

[30] D0 Collaboration. Search for High Mass Top Quark Production in $p\overline{p}$ Collisions at $\sqrt{s}$ 1.8 TeV. *Phys. Rev. Lett.*, 74:2422–2426, 13, 1995.

[31] CMS Collaboration. Observation of a new boson at a mass of 125 GeV with the CMS experiment at the LHC. *Phys. Lett. B*, 716(1):30–61, 2012.

[32] ATLAS Collaboration. Observation of a new particle in the search for the Standard Model Higgs boson with the ATLAS detector at the LHC. *Phys. Lett. B*, 716(1):1–29, 2012.

[33] CDF Collaboration. High-precision measurement of the W boson mass with the CDF II detector. *Science*, 376(6589):170–176, 2022.

[34] T. Kajita. Nobel Lecture: Discovery of atmospheric neutrino oscillations. *Rev. Mod. Phys.*, 88(3):030501, 2016.

[35] A. B. McDonald. Nobel lecture: the Sudbury Neutrino Observatory: observation of flavor change for solar neutrinos. *Rev. Mod. Phys.*, 88(3):030502, 2016.

[36] P. Minkowski. $\mu \to e\gamma$ at a rate of one out of 109 muon decays? *Phys. Lett. B*, 67(4):421–428, 1977.

[37] B. Pontecorvo. Neutrino Experiments and the Problem of Conservation of Leptonic Charge. *Zh. Eksp. Teor. Fiz.*, 53:1717–1725, 1967.

[38] Z. Maki, M. Nakagawa, and S. Sakata. Remarks on the Unified Model of Elementary Particles. *Prog. Theor. Phys.*, 28(5):870–880, 1962.

[39] Super-Kamiokande Collaboration. Solar neutrino measurements in Super-Kamiokande-IV. *Phys. Rev. D*, 94:052010, 5, 2016.

[40] KamLAND Collaboration. Reactor on-off antineutrino measurement with KamLAND. *Phys. Rev. D*, 88:033001, 3, 2013.

[41] T2K Collaboration. Constraint on the matter–antimatter symmetry-violating phase in neutrino oscillations. *Nature*, 580:339–344, 7803, 2020.

[42] Double Chooz Collaboration. Double Chooz θ_{13} measurement via total neutron capture detection. *Nature Physics*, 16:558–564, 5, 2020.

[43] A. D. Sakharov. Violation of CP Invariance, C asymmetry, and baryon asymmetry of the universe. *Pisma Zh. Eksp. Teor. Fiz.*, 5:32–35, 1967.

[44] BABAR Collaboration. Measurement of CP-Violating Asymmetries in B^0 Decays to CP Eigenstates. *Phys. Rev. Lett.*, 86:2515–2522, 12, 2001.

[45] Belle Collaboration. Observation of Large CP Violation in the Neutral B Meson System. *Phys. Rev. Lett.*, 87:091802, 9, 2001.

[46] LHCb Collaboration. First Observation of CP Violation in the Decays of B_s^0 Mesons. *Phys. Rev. Lett.*, 110:221601, 22, 2013.

[47] LHCb Collaboration. Observation of CP Violation in Charm Decays. *Phys. Rev. Lett.*, 122:211803, 21, 2019.

[48] C. A. Baker et al. Improved Experimental Limit on the Electric Dipole Moment of the Neutron. *Phys. Rev. Lett.*, 97:131801, 13, 2006.

[49] H. Georgi and S. L. Glashow. Unity of All Elementary-Particle Forces. *Phys. Rev. Lett.*, 32:438–441, 8, 1974.

[50] D. Croon et al. GUT Physics in the Era of the LHC. *Front. Phys.*, 7, 2019.

[51] G. F. Giudice. Naturally speaking: the naturalness criterion and physics at the LHC. *Perspectives on LHC physics*:155–178, 2008.

[52] G. t Hooft et al. Recent developments in gauge theories. *Phys. Today*, 34(5):83, 1981.

[53] S. P. Martin. A supersymmetry primer. In *Perspectives on supersymmetry II*, pages 1–153. 2010.

[54] M. Drees. An introduction to supersymmetry. arXiv: `9611409 [hep-ph]`.

[55] S. Weinberg. *The quantum theory of fields III: Supersymmetry*. Cambridge university press, 2005.

[56] Particle Data Group. Review of Particle Physics. *PTEP*, 2022:083C01, 2022.

[57] CMS Supersymmetry - public results. `https://cms-results.web.cern.ch/cms-results/public-results/publications/SUS/SUS.html`.

[58] C. Devereux. *Cosmological Clues: Evidence for the Big Bang, Dark Matter and Dark Energy*. CRC Press, 2020.

[59] F. Zwicky. Die Rotverschiebung von extragalaktischen Nebeln. *Helvetica Physica Acta*, 6:110–127, 1933.

[60] V. C. Rubin et al. Extended rotation curves of high-luminosity spiral galaxies. IV. Systematic dynamical properties, Sa -> Sc. *Astrophys. Journal*, 225:L107–L111, 1978.

[61] K. G. Begeman et al. Extended rotation curves of spiral galaxies: dark haloes and modified dynamics. *Mon. Notices Royal Astron. Soc.*, 249(3):523–537, 1991.

[62] D. Clowe et al. A direct empirical proof of the existence of dark matter. *Astrophys. Journal*, 648(2):L109–L113, 2006.

[63] H. Miyatake et al. First identification of a CMB lensing signal produced by 1.5 million galaxies at z 4: Constraints on matter density fluctuations at high redshift. *Phys. Rev. Lett.*, 129(6):061301, 2022.

[64] Planck Collaboration. Planck 2018 results - VIII. Gravitational lensing. *Astron. Astrophys.*, 641:A8, 2020.

[65] U. Sarkar. *Particle and Astroparticle physics*. CRC Press, 2007.

[66] D. Fixsen. The temperature of the cosmic microwave background. *Astrophys. Journal*, 707(2):916, 2009.

[67] Planck Collaboration. Planck 2018 results - VI. Cosmological parameters. *Astron. Astrophys.*, 641:A6, 2020.

[68] A. Schneider et al. Non-linear evolution of cosmological structures in warm dark matter models. *Mon. Notices Royal Astron. Soc.*, 424(1):684–698, 2012.

[69] R. D. Peccei and H. R. Quinn. CP conservation in the presence of pseudoparticles. *Phys. Rev. Lett.*, 38(25):1440, 1977.

[70] The XENON Experiment: Enlightening the Dark. `http://www.xenon1t.org/`.

[71] LUX Dark Matter Experiment. `https://sites.brown.edu/luxdarkmatter/`.

[72] PandaX, Particle and Astrophysical Xenon TPC. `https://pandax.sjtu.edu.cn/`.

[73] The Fermi Large Area Telescope. `https://glast.sites.stanford.edu/`.

[74] High Energy Stereoscopic System. `https://www.mpi-hd.mpg.de/hfm/HESS/`.

[75] The Very Energetic Radiation Imaging Telescope Array System. `https://veritas.sao.arizona.edu/`.

[76] The IceCube neutrino observatory. `https://icecube.wisc.edu/`.

[77] The Alpha Magnetic Spectrometer. `https://ams02.space/`.

[78] S. Coutu. Positrons Galore. *APS Physics*, 6:40, 2013.

[79] B. Dong. Searches for dark sector particles (including long-lived mediators and missing ET signatures) in ATLAS and CMS, 2022. URL: `https://indico.cern.ch/event/922783/contributions/4913949/attachments/2483512/4264599/bdong-IDM2022.pdf`. Presented at the 14th International Conference on Identification of Dark Matter.

[80] R. O. Essig. Dark Sectors and New, Light, Weakly-Coupled Particles. arXiv: `1311.0029`.

[81] J. Alexander et al. Dark sectors 2016 workshop: community report. arXiv: `1608.08632`.

[82] I. Cholis et al. The PAMELA positron excess from annihilations into a light boson. *J. Cosmol. Astropart. Phys.*, 2009(12):007–007, 2009.

[83] J. Jaeckel et al. Signatures of a Hidden Cosmic Microwave Background. *Phys. Rev. Lett.*, 101:131801, 13, 2008.

[84] G. Jungman et al. Supersymmetric dark matter. *Phys. Rep.*, 267(5):195–373, 1996.

[85] M. Pospelov. Secluded U(1) below the weak scale. *Phys. Rev. D*, 80:095002, 9, 2009.

[86] V. Barger et al. Proton size anomaly. *Phys. Rev. Lett.*, 106:153001, 15, 2011.

[87] M. Fabbrichesi, E. Gabrielli, and B. Mele. Hunting down massless dark photons in kaon physics. *Phys. Rev. Lett.*, 119:031801, 2017.

[88] S. Biswas, E. Gabrielli, and B. Mele. Dark Photon Searches via Higgs Boson Production at the LHC and Beyond. *Symmetry*, 14:1522, 2022.

[89] M. Cobal et al. Z-boson decays into an invisible dark photon at the LHC, HL-LHC and future lepton colliders. *Phys. Rev. D*, 102:035027, 2020.

[90] M. Fabbrichesi, E. Gabrielli, and G. Lanfranchi. *The physics of the dark photon: a primer*. Springer, 2021.

[91] NA48/2 Collaboration. Search for the dark photon in ϕ^0 decays. *Phys. Lett. B*, 746:178–185, 2015.

[92] A1 Collaboration. Search at the Mainz Microtron for Light Massive Gauge Bosons Relevant for the Muon $g-2$ Anomaly. *Phys. Rev. Lett.*, 112:221802, 22, 2014.

[93] BaBar Collaboration. Search for a Dark Photon in e^+e^- Collisions at BaBar. *Phys. Rev. Lett.*, 113:201801, 20, 2014.

[94] KLOE-2 Collaboration. Search for a vector gauge boson in ϕ meson decays with the KLOE detector. *Phys. Lett. B*, 706(4):251–255, 2012.

[95] KLOE-2 Collaboration. Limit on the production of a light vector gauge boson in ϕ meson decays with the KLOE detector. *Phys. Lett. B*, 720(1):111–115, 2013.

[96] KLOE-2 Collaboration. Search for light vector boson production in $e^+e^- \to \mu^+mu^-\gamma$ interactions with the KLOE experiment. *Phys. Lett. B*, 736:459–464, 2014.

[97] KLOE-2 Collaboration. Limit on the production of a new vector boson in $e^+e^- \to U\gamma$, $U \to \phi^+\phi^-$ with the KLOE experiment. *Phys. Lett. B*, 757:356–361, 2016.

[98] CMS Collaboration. Search for a Narrow Resonance Lighter than 200 GeV Decaying to a Pair of Muons in Proton-Proton Collisions at $\sqrt{s} = 13$ TeV. *Phys. Rev. Lett.*, 124:131802, 13, 2020.

[99] LHCb Collaboration. Search for $A' \to \mu^+\mu^-$ decays. *Phys. Rev. Lett.*, 124:041801, 4, 2020.

[100] E. M. Riordan et al. Search for short-lived axions in an electron-beam-dump experiment. *Phys. Rev. Lett.*, 59:755–758, 7, 1987.

[101] L. Marsicano et al. Dark photon production through positron annihilation in beam-dump experiments. *Phys. Rev. D*, 98:015031, 1, 2018.

[102] A. Bross et al. Search for short-lived particles produced in an electron beam dump. *Phys. Rev. Lett.*, 67:2942–2945, 21, 1991.

[103] S. Gninenko. Constraints on sub-GeV hidden sector gauge bosons from a search for heavy neutrino decays. *Phys. Lett. B*, 713(3):244–248, 2012.

[104] J. Blumlein and J. Brunner. New exclusion limits for dark gauge forces from beam-dump data. *Phys. Lett. B*, 701(2):155–159, 2011.

[105] J. Blumlein and J. Brunner. New exclusion limits on dark gauge forces from proton Bremsstrahlung in beam-dump data. *Phys. Lett. B*, 731:320–326, 2014.

[106] T. Lagouri. Review on Higgs hidden-dark sector physics. *Phys. Scripta*, 97(2):024001, 2022.

[107] J. H. Chang et al. Revisiting Supernova 1987A constraints on dark photons. *J. High Energy Phys.*, 2017(1):107, 2017.

[108] Belle Collaboration. The Belle II Physics Book. *Prog. Theor. Exp. Phys.*, 2019(12):123C01, 2019.

[109] P. Ilten et al. Proposed Inclusive Dark Photon Search at LHCb. *Phys. Rev. Lett.*, 116:251803, 25, 2016.

[110] P. Ilten et al. Dark photons from charm mesons at LHCb. *Phys. Rev. D*, 92:115017, 11, 2015.

[111] NA62 Collaboration. ADDENDUM I TO P326 Continuation of the physics programme of the NA62 experiment. Technical report, 2019. URL: `https://cds.cern.ch/record/2691873`.

[112] S. Gninenko. Addendum to the NA64 Proposal: Search for the $A' \to$ *invisible* and $X \to e^+e^-$ decays in 2021. Technical report, 2018. URL: `http://cds.cern.ch/record/2300189`.

[113] J. L. Feng et al. ForwArd Search ExpeRiment at the LHC. *Phys. Rev. D*, 97:035001, 3, 2018.

[114] A. Berlin et al. Dark sectors at the Fermilab SeaQuest experiment. *Phys. Rev. D*, 98:035011, 3, 2018.

[115] Heavy Photon Search Collaboration. Search for a dark photon in electroproduced e^+e^- pairs with the Heavy Photon Search experiment at JLab. *Phys. Rev. D*, 98:091101, 9, 2018.

[116] A. Caldwell et al. Particle physics applications of the AWAKE acceleration scheme. arXiv: `1812.11164`.

[117] L. Doria et al. Dark Matter at the Intensity Frontier: the new MESA electron accelerator facility. arXiv: `1908.07921`.

[118] L. Doria et al. Search for light dark matter with the MESA accelerator. arXiv: `1809.07168`.

[119] D. Curtin et al. Illuminating dark photons with high-energy colliders. *J. High Energy Phys.*, 2015(2):1–45, 2015.

[120] M. Karliner et al. Radiative return capabilities of a high-energy, high-luminosity e^+e^- collider. *Phys. Rev. D*, 92:035010, 3, 2015.

[121] M. D'Onofrio et al. Searching for dark photons at the LHeC and FCC-he. *Phys. Rev. D*, 101:015020, 1, 2020.

[122] J. L. Feng et al. Protophobic Fifth-Force Interpretation of the Observed Anomaly in ^8Be Nuclear Transitions. *Phys. Rev. Lett.*, 117:071803, 7, 2016.

[123] J. L. Feng et al. Particle physics models for the 17 MeV anomaly in beryllium nuclear decays. *Phys. Rev. D*, 95:035017, 3, 2017.

[124] J. Beacham et al. Physics beyond colliders at CERN: beyond the Standard Model working group report. *J. Phys. G: Nucl. Part. Phys.*, 47(1):010501, 2019.

[125] CMS Collaboration. Properties of the Higgs-like boson in the decay H to ZZ to 4l in pp collisions at $\sqrt{s}$=7 and 8 TeV. Technical report, 2013. URL: `https://cds.cern.ch/record/1523767`.

[126] ATLAS Collaboration. Measurement of the total ZZ production cross section in proton proton collision at $\sqrt{s} = 8$ TeV in 20 fb^{-1} with the ATLAS detector. Technical report, 2013. URL: `https://cds.cern.ch/record/1525555`.

[127] CMS Collaboration. Search for a non-standard-model Higgs boson decaying to a pair of new light bosons in four-muon final states. *Phys. Lett. B*, 726(4):564–586, 2013.

[128] A. Falkowski et al. Hidden higgs decaying to lepton jets. *J. High Energy Phys.*, 2010(5):1–39, 2010.

[129] N. Arkani-Hamed et al. A theory of dark matter. *Phys. Rev. D*, 79:015014, 2009.

[130] M. Baumgart et al. Non-abelian dark sectors and their collider signatures. *J. High Energy Phys.*, (04):014, 2009.

[131] ATLAS Collaboration. Search for long-lived neutral particles decaying into lepton jets in proton-proton collisions at $\sqrt{s} = 8$ TeV with the ATLAS detector. *J. High Energy Phys.*, 2014:1–48, 2014.

[132] ATLAS Collaboration. A search for prompt lepton-jets in pp collisions at $\sqrt{s} = 8$ TeV with the ATLAS detector. *J. High Energy Phys.*, 2016:62, 2016.

[133] PHENIX Collaboration. Search for dark photons from neutral meson decays in $p + p$ and $d + \mathrm{Au}$ collisions at $\sqrt{s_{NN}} = 200\mathrm{GeV}$. *Phys. Rev. C*, 91:031901, 3, 2015.

[134] S. Abrahamyan et al. Search for a New Gauge Boson in Electron-Nucleus Fixed-Target Scattering by the APEX Experiment. *Phys. Rev. Lett.*, 107:191804, 19, 2011.

[135] HADES Collaboration. Searching a Dark Photon with HADES. *Phys. Lett. B*, 731:265–271, 2014.

[136] A. Fradette et al. Cosmological Constraints on Very Dark Photons. *Phys. Rev. D*, 90:035022, 2014.

[137] J. B. Dent et al. Constraints on Light Hidden Sector Gauge Bosons from Supernova Cooling, 2012. arXiv: `1201.2683 [astro-ph.CO]`.

[138] H. K. Dreiner et al. Supernova constraints on MeV dark sectors from e^+e^- annihilations. *Phys. Rev. D*, 89:105015, 2014.

[139] R. Essig et al. Discovering new light states at neutrino experiments. *Phys. Rev. D*, 82:113008, 11, 2010.

[140] B. Batell et al. Exploring portals to a hidden sector through fixed targets. *Phys. Rev. D*, 80:095024, 9, 2009.

[141] LHCb Collaboration. Search for dark photons produced in 13 tev *pp* collisions. *Phys. Rev. Lett.*, 120:061801, 6, 2018.

[142] CMS Collaboration. A search for pair production of new light bosons decaying into muons in proton-proton collisions at 13 TeV. *Phys. Lett. B*, 796:131–154, 2019.

[143] CMS Collaboration. Searches for invisible decays of the Higgs boson in pp collisions at $\sqrt{s} = 7$, 8, and 13 TeV. *J. High Energy Phys.*, 02:135, 2017.

[144] CMS Collaboration. Search for long-lived particles that decay into final states containing two electrons or two muons in proton-proton collisions at s=8 tev. *Phys. Rev. D*, 91:052012, 2015.

[145] Darmé, Luc and others. Light dark Higgs boson in minimal sub-GeV dark matter scenarios. *J. High Energy Phys.*, 03:084, 2018.

[146] C. Cheung et al. Lepton Jets in (Supersymmetric) Electroweak Processes. *J. High Energy Phys.*, 04:116, 2010.

[147] W. R. Inc. Mathematica, Version 13.2. URL: `https://www.wolfram.com/mathematica`.

[148] A. Alloul et al. FeynRules 2.0—A complete toolbox for tree-level phenomenology. *Comput. Phys. Commun.*, 185(8):2250–2300, 2014.

[149] J. F. Gunion et al. *The Higgs Hunter's Guide*. 2000.

[150] D. Curtin et al. Exotic decays of the 125 GeV Higgs boson. *Phys. Rev. D*, 90:075004, 2014.

[151] E. Izaguirre and D. Stolarski. Searching for Higgs Decays to as Many as 8 Leptons. *Phys. Rev. Lett.*, 121:221803, 2018.

[152] J. Alwall et al. The automated computation of tree-level and next-to-leading order differential cross sections, and their matching to parton shower simulations. *J. High Energy Phys.*, 07:079, 2014.

[153] Joint LEP SUSY working group Results. `https://lepsusy.web.cern.ch/lepsusy/`.

[154] A. Costantini et al. Vector boson fusion at multi-TeV muon colliders. *J. High Energy Phys.*, 2020(9):1–59, 2020.

[155] O. S. Brüning et al. *LHC Design Report*. CERN Yellow Rep. Monogr. 2004. DOI: `10.5170/CERN-2004-003-V-1`.

[156] CMS Luminosity - public results. `https://twiki.cern.ch/twiki/bin/view/CMSPublic/LumiPublicResults`.

[157] High Luminosity LHC project. `https://hilumilhc.web.cern.ch/content/hl-lhc-project`.

[158] O. Aberle et al. *High-Luminosity Large Hadron Collider (HL-LHC): Technical design report*. CERN Yellow Rep. Monogr. 2020. DOI: `10.23731/CYRM-2020-0010`.

[159] CMS Collaboration. CMS, the Compact Muon Solenoid: Technical proposal, 1994.

[160] CMS Collaboration. The CMS experiment at the CERN LHC. The Compact Muon Solenoid experiment. *J. Instrum.*, 3:S08004. 361 p, 2008.

[161] CMS Collaboration. Cutaway diagrams of CMS detector, 2019. URL: https://cds.cern.ch/record/2665537.

[162] CMS Collaboration. *The CMS tracker system project: Technical Design Report*. CERN, 1997. URL: https://cds.cern.ch/record/368412.

[163] CMS Collaboration. The Phase-2 Upgrade of the CMS Tracker. Technical report, 2017. URL: https://cds.cern.ch/record/2272264.

[164] CMS Collaboration. *The CMS electromagnetic calorimeter project: Technical Design Report*. CERN, 1997. URL: https://cds.cern.ch/record/349375.

[165] Q. Ingram. Energy resolution of the barrel of the CMS Electromagnetic Calorimeter. *J. Instrum.*, 2(04):P04004–P04004, 2007.

[166] CMS Collaboration. *The CMS hadron calorimeter project: Technical Design Report*. CERN, 1997. URL: https://cds.cern.ch/record/357153.

[167] CMS HCAL/ECAL Collaborations. The CMS barrel calorimeter response to particle beams from 2 to 350 GeV/c. *Eur. Phys. J. C*, 60(3):359–373, 2009.

[168] CMS Collaboration. The Phase-2 Upgrade of the CMS Barrel Calorimeters. Technical report, 2017. URL: https://cds.cern.ch/record/2283187.

[169] CMS Collaboration. The Phase-2 Upgrade of the CMS Endcap Calorimeter. Technical report, 2017. URL: https://cds.cern.ch/record/2293646.

[170] CMS Collaboration. The Phase-2 Upgrade of the CMS Muon Detectors. Technical report, 2017. URL: https://cds.cern.ch/record/2283189.

[171] CMS Collaboration. *The CMS muon project: Technical Design Report*. CERN, 1997. URL: https://cds.cern.ch/record/343814.

[172] CMS Collaboration. *CMS TriDAS project: Technical Design Report, Volume 1: The Trigger Systems*. URL: https://cds.cern.ch/record/706847.

[173] CMS Collaboration. The CMS high level trigger. *Eur. Phys. J. C*, 46(3):605–667, 2006.

[174] CMS Collaboration. The Phase-2 Upgrade of the CMS Level-1 Trigger. Technical report, 2020. URL: https://cds.cern.ch/record/2714892.

[175] CMS Collaboration. The Phase-2 Upgrade of the CMS Data Acquisition and High Level Trigger. Technical report, 2021. URL: https://cds.cern.ch/record/2759072.

[176] CMS Collaboration. Particle-flow reconstruction and global event description with the CMS detector. *J. Instrum.*, 12(10):P10003–P10003, 2017.

[177] M. Thomson. Particle flow calorimetry and the PandoraPFA algorithm. *Nucl. Instrum. Methods. Phys. Res. A*, 611(1):25–40, 2009.

[178] CMS Collaboration. Description and performance of track and primary-vertex reconstruction with the CMS tracker. *J. Instrum.*, 9(10):P10009–P10009, 2014.

[179] R. Frühwirth. Application of Kalman filtering to track and vertex fitting. *Nucl. Instrum. Methods. Phys. Res. A*, 262(2):444–450, 1987.

[180] W. Adam et al. Reconstruction of Electrons with the Gaussian-Sum Filter in the CMS Tracker at the LHC. Technical report, 2005. URL: `https://cds.cern.ch/record/815410`.

[181] M. Cacciari et al. FastJet user manual. *Eur. Phys. J. C*, 72(3):1–54, 2012.

[182] M. Cacciari et al. The anti-$k_t$jet clustering algorithm. *J. High Energy Phys.*, 2008(04):063–063, 2008.

[183] D. Bertolini et al. Pileup per particle identification. *J. High Energy Phys.*, 2014(10):59, 2014.

[184] CMS Collaboration. Performance of the reconstruction and identification of high-momentum muons in proton-proton collisions at $\sqrt{s}$= 13 TeV. *J. Instrum.*:P02027–P02027, 2020.

[185] CMS Collaboration. Performance of the CMS muon detector and muon reconstruction with proton-proton collisions at $\sqrt{s} = 13$ TeV. *J. Instrum.*, 13(06):P06015, 2018.

[186] C. Oleari. The POWHEG-BOX. *Nucl. Phys. B Proc. Suppl.*, 205-206:36–41, 2010.

[187] Y. Gao et al. Spin Determination of Single-Produced Resonances at Hadron Colliders. *Phys. Rev. D*, 81:075022, 2010.

[188] C. Bierlich et al. A comprehensive guide to the physics and usage of PYTHIA 8.3, 2022. arXiv: `2203.11601 [hep-ph]`.

[189] G. Sorrentino. Monte Carlo tuning in CMS. In *106° Congresso Nazionale della Societa'Italiana di Fisica*, pages 1–4, 2021.

[190] CMS Collaboration. Performance of the CMS muon trigger system in proton-proton collisions at $\sqrt{s} = 13$ TeV. *J. Instrum.*, 16:P07001, 2021.

[191] CMS Collaboration. CMS Phase 1 heavy flavour identification performance and developments. Technical report, 2017. URL: `https://cds.cern.ch/record/2263802`.

[192] G. Punzi. Sensitivity of searches for new signals and its optimization, 2003. arXiv: `physics/0308063`.

[193] W. Shi. *A Model Independent Search for New Bosons Decaying into Muons at LHC*. PhD thesis, Rice University, 2021.

[194] M. Grazzini and H. Sargsyan. Heavy-quark mass effects in Higgs boson production at the LHC. *J. High Energy Phys.*, 09:129, 2013.

[195] LHC Higgs Cross Section Working Group. Handbook of LHC Higgs Cross Sections: 4. Deciphering the Nature of the Higgs Sector, 2016.

[196] CMS Collaboration. Studies of Higgs boson production in the four-lepton final state at $\sqrt{s} = 13$TeV, 2016.

[197] J. M. Campbell and R. K. Ellis. MCFM for the Tevatron and the LHC. *Nucl. Phys. B Proc. Suppl.*, 205-206:10–15, 2010.

[198] CMS luminosity measurement for the 2018 data-taking period at $\sqrt{s} =$ 13TeV, 2019.

[199] CMS Collaboration. Search for Light Resonances Decaying into Pairs of Muons as a Signal of New Physics. *J. High Energy Phys.*, 07:098, 2011.

[200] Procedure for the LHC Higgs boson search combination in Summer 2011, 2011.

[201] G. Cowan. *Statistical data analysis*. Oxford university press, 1998.

[202] G. Cowan et al. Asymptotic formulae for likelihood-based tests of new physics. *Eur. Phys. J. C*, 71:1554, 2011.

[203] J. De Blas et al. Higgs boson studies at future particle colliders. *J. High Energy Phys.*, 2020(1):1–97, 2020.

[204] M. Cepeda et al. Report from Working Group 2: Higgs Physics at the HL-LHC and HE-LHC. *CERN Yellow Rep. Monogr.*, 7:221–584, 2019. arXiv: `1902.00134 [hep-ph]`.

[205] A. Abada et al. FCC physics opportunities. *Eur. Phys. J. C*, 79(6):1–161, 2019.

[206] CEPC Study Group. CEPC Conceptual Design Report: Volume 2 - Physics & Detector, 2018. arXiv: `1811.10545 [hep-ex]`.

[207] K. Fujii et al. Physics Case for the 250 GeV Stage of the International Linear Collider, 2017. arXiv: `1710.07621 [hep-ex]`.

[208] P. Bambade et al. The International Linear Collider: A Global Project, 2019. arXiv: `1903.01629 [hep-ex]`.

[209] CLIC Collaboration. The Compact Linear e^+e^- Collider (CLIC): Physics Potential, 2018. arXiv: `1812.07986 [hep-ex]`.

[210] G. I. Budker. Accelerators and colliding beams. *Conf. Proc. C*, 690827:33–39, 1969.

[211] K. R. Long et al. Muon colliders to expand frontiers of particle physics. *Nature Physics*, 17(3):289–292, 2021.

[212] T. Roser et al. Report of the Snowmass 2021 Collider Implementation Task Force, 2022. arXiv: 2208.06030.

[213] C. Aimè et al. Muon Collider Physics Summary, 2022. arXiv: 2203.07256.

[214] J. De Blas et al. The physics case of a 3 TeV muon collider stage, 2022. arXiv: 2203.07261.

[215] H. Al Ali et al. The muon smasher's guide. *Rep. Prog. Phys.*:084201, 2022.

[216] K. Black et al. Muon Collider Forum Report, 2022. arXiv: 2209.01318.

[217] D. Buttazzo, R. Franceschini, and A. Wulzer. Two paths towards precision at a very high energy lepton collider. *J. High Energy Phys.*, 2021(5):1–39, 2021.

[218] D. Buttazzo et al. Fusing vectors into scalars at high energy lepton colliders. *J. High Energy Phys.*, 2018(11):1–37, 2018.

[219] M. Chiesa et al. Measuring the quartic Higgs self-coupling at a multi-TeV muon collider. *J. High Energy Phys.*, 2020(9):1–29, 2020.

[220] A. Azatov et al. New physics in b $\to$ s$\mu\mu$: FCC-hh or a muon collider? *J. High Energy Phys.*, 2022(10):1–50, 2022.

[221] D. Buttazzo and P. Paradisi. Probing the muon g-2 anomaly with the Higgs boson at a muon collider. *Phys. Rev. D*, 104(7):075021, 2021.

[222] J. Arakawa et al. Probing muon $g-2$ at a future muon collider, 2022. arXiv: 2208.14464.

[223] M. Bai et al. C^3: A "Cool" Route to the Higgs Boson and Beyond, 2021. arXiv: 2110.15800.

[224] V. N. Litvinenko et al. The ReLiC: Recycling Linear $e+e-$ Collider, 2022. arXiv: 2203.06476.

[225] T. Kurz et al. Demonstration of a compact plasma accelerator powered by laser-accelerated electron beams. *Nat. Commun.*, 12(1):1–9, 2021.

[226] European Strategy For Particle Physics Preparatory Group. Physics briefing book, 2019. arXiv: 1910.11775.

[227] R. Bollig et al. Muons in Supernovae: Implications for the Axion-Muon Coupling. *Phys. Rev. Lett.*, 125(5), 2020.

[228] F. D'Eramo et al. Hot axions and the h_0 tension. *J. Cosmol. Astropart. Phys.*, 2018(11):014–014, 2018.

[229] M. Escudero et al. Cosmology with a very light $L_\mu - L_\tau$ gauge boson. *J. High Energy Phys.*, 2019(3):1–29, 2019.

[230] D. Banerjee et al. Search for axionlike and scalar particles with the NA64 experiment. *Phys. Rev. Lett.*, 125(8):081801, 2020.

[231] J. Abdallah et al. Search for one large extra dimension with the DELPHI detector at LEP. *Eur. Phys. J. C*, 60(1):17–23, 2009.

[232] BaBar Collaboration. Search for invisible decays of a dark photon produced in $e + e-$ collisions at BaBar. *Phys. Rev. Lett.*, 119(13):131804, 2017.

[233] M. J. Dolan et al. Revised constraints and Belle II sensitivity for visible and invisible axion-like particles. *J. High Energy Phys.*, 2017(12):1–29, 2017.

[234] J. D. Bjorken et al. Search for neutral metastable penetrating particles produced in the SLAC beam dump. *Phys. Rev. D*, 38:3375–3386, 11, 1988.

[235] M. Casarsa et al. Monochromatic single photon events at the muon collider. *Phys. Rev. D*, 105(7):075008, 2022.

[236] International Muon Collider Collaboration. `https://muoncollider.web.cern.ch/`.

[237] C. Adolphsen et al. European Strategy for Particle Physics–Accelerator R&D Roadmap, 2022. arXiv: `2201.07895`.

[238] D. Stratakis et al. A Muon Collider Facility for Physics Discovery, 2022. arXiv: `2203.08033`.

[239] M. Palmer. The US muon accelerator program, 2015. arXiv: `1502.03454`.

[240] MICE Collaboration. Demonstration of cooling by the muon ionization cooling experiment. *Nature*, 578(7793):53–59, 2020.

[241] J. P. Delahaye et al. Muon colliders, 2019. arXiv: `1901.06150`.

[242] B. J. King. Neutrino radiation challenges and proposed solutions for many-TeV muon colliders. In *AIP Conf. Proc.* Volume 530 of number 1, pages 165–180. American Institute of Physics, 2000.

[243] M. Boscolo et al. The future prospects of muon colliders and neutrino factories. *Reviews of Accelerator Science and Technology*, 10(01):189–214, 2019.

[244] M. Antonelli et al. Novel proposal for a low emittance muon beam using positron beam on target. *Nucl. Instrum. Methods. Phys. Res. A*, 807:101–107, 2016.

[245] D. Alesini et al. Positron driven muon source for a muon collider. Technical report, 2019. URL: http://cds.cern.ch/record/2676800.

[246] D. Calzolari. Machine-detector interface studies for a 10 TeV muon collider. https://indico.cern.ch/event/1175126/contributions/5024029/attachments/2525935/4345891/MDIcollab.pdf, 2022. Presented at the First Muon Collider Collaboration Meeting.

[247] N. Mokhov and S. Striganov. Detector backgrounds at muon colliders. *Physics Procedia*, 37:2015–2022, 2012.

[248] N. Bartosik et al. Simulated Detector Performance at the Muon Collider, 2022. arXiv: 2203.07964.

[249] F. Collamati. Machine-induced background studies for 1.5 TeV and 3 TeV. https://indico.cern.ch/event/1175126/contributions/5024027/attachments/2526757/4346502/Collamati_MDI_Oct2022.pdf, 2022. Presented at the First Muon Collider Collaboration Meeting.

[250] N. V. Mokhov and C. C. James. The MARS Code System User's Guide Version 15(2016), 2017.

[251] N. Mokhov et al. Muon Collider interaction region and machine-detector interface design, 2012. arXiv: 1202.3979.

[252] Y. I. Alexahin et al. Muon collider interaction region design. *Phys. Rev. ST Accel. Beams*, 14:061001, 6, 2011.

[253] G. W. Foster and N. V. Mokhov. Backgrounds and detector performance at a 2× 2 TeV μ+ μ- collider. In *AIP Conf. Proc.* Volume 352 of number 1, pages 178–190, 1996.

[254] C. Ahdida et al. New capabilities of the FLUKA multi-purpose code. *Front. Phys.*:705, 2022.

[255] A. Ferrari et al. *FLUKA: A multi-particle transport code (program version 2005)*. CERN Yellow Rep. Monogr. CERN, 2005. URL: https://cds.cern.ch/record/898301.

[256] F. Collamati et al. Advanced assessment of beam-induced background at a muon collider. *J. Instrum.*, 16(11):P11009, 2021.

[257] S. Jindariani et al. Promising Technologies and R&D Directions for the Future Muon Collider Detectors, 2022. arXiv: 2203.07224.

[258] L. Linssen et al. Physics and detectors at CLIC: CLIC conceptual design report, 2012. arXiv: 1202.5940.

[259] CLICdp. CLICdet: The post-CDR CLIC detector model, 2017.

[260] Muon Collider Software. https://confluence.infn.it/display/muoncollider/Software.

[261] ILC Soft. https://ilcsoft.desy.de/portal/.

[262] F. Gaede et al. LCIO-A persistency framework for linear collider simulation studies, 2003. arXiv: 0306114.

[263] S. Agostinelli et al. Geant4—a simulation toolkit. *Nucl. Instrum. Methods. Phys. Res. A*, 506(3):250–303, 2003.

[264] M. Frank et al. AIDASoft/DD4hep, 2018. URL: http://dd4hep.cern.ch/.

[265] F. Gaede. Marlin and LCCD—Software tools for the ILC. *Nucl. Instrum. Methods. Phys. Res. A*, 559(1):177–180, 2006.

[266] J. Marshall and M. Thomson. The pandora particle flow algorithm, 2013. arXiv: 1308.4537.

[267] T. Kramer. Track parameters in LCIO. *LC Notes*, 2006.

[268] P. Billoir. Progressive track recognition with a Kalman-like fitting procedure. *Comput. Phys. Commun.*, 57(1):390–394, 1989.

[269] P. Billoir and S. Qian. Simultaneous pattern recognition and track fitting by the Kalman filtering method. *Nucl. Instrum. Methods. Phys. Res. A*, 294(1):219–228, 1990.

[270] A. Glazov et al. Filtering tracks in discrete detectors using a cellular automaton. *Nucl. Instrum. Methods. Phys. Res. A*, 329(1-2):262–268, 1993.

[271] M. Hansroul et al. Fast circle fit with the conformal mapping method. *Nucl. Instrum. Methods Phys. Res., A*, 270(CERN-DD-88-20):498–501, 1988.

[272] E. Brondolin et al. Conformal tracking for all-silicon trackers at future electron–positron colliders. *Nucl. Instrum. Methods. Phys. Res. A*, 956:163304, 2020.

[273] X. Ai et al. A common tracking software project. *Computing and Software for Big Science*, 6(1):1–23, 2022.

[274] C. Aimè et al. Muon Reconstruction Performance in Presence of Beam-Induced Background at Muon Collider, 2020. Presented at the APS April Meeting.

[275] I. Vai et al. Muon reconstruction performance and detector-design considerations for a Muon Collider. *PoS*, EPS-HEP2021:833, 2022.

[276] P. Paolucci and other. CMS Resistive Plate Chamber overview, from the present system to the upgrade phase I. RPC project overview, from the present system to the upgrade. *J. Instrum.*, 8:P04005, 2013.

[277] F. Sauli. The gas electron multiplier (GEM): Operating principles and applications. *Nucl. Instrum. Methods. Phys. Res. A*, 805:2–24, 2016.

[278] J. Bortfeldt et al. PICOSEC: Charged particle timing at sub-25 picosecond precision with a Micromegas based detector. *Nucl. Instrum. Methods. Phys. Res. A*, 903:317–325, 2018.

[279] Y. Giomataris et al. MICROMEGAS: a high-granularity position-sensitive gaseous detector for high particle-flux environments. *Nucl. Instrum. Methods. Phys. Res. A*, 376(1):29–35, 1996.

[280] D. Abbaneo et al. R&D on a new type of micropattern gaseous detector: The Fast Timing Micropattern detector. *Nucl. Instrum. Methods. Phys. Res. A*, 845:313–317, 2017.

[281] Geant4 Collaboration. Physics Reference Manual. `https://geant4.web.cern.ch/support/user_documentation`.

[282] W. K. et al. WHIZARD simulating multi-particle processes at LHC and ILC. *Eur. Phys. J. C*, 71:1–29, 2011.

[283] M. Moretti et al. O'Mega: An Optimizing matrix element generator:1981–2009, 2001. arXiv: `hep-ph/0102195`.

[284] E. van der Kraaij and J. Marshall. Development of the PANDORA PFA NEW muon reconstruction algorithm. Technical report, 2011. URL: `https://cds.cern.ch/record/1443539`.

[285] C. Aimè et al. Dark-SUSY channels to study muon reconstruction performance at the Muon Collider. *PoS*, EPS-HEP2021:644, 2022.

[286] C. Aimè. Muon detectors performance. `https://indico.cern.ch/event/1175126/contributions/5024033/attachments/2526702/4346101/annualmeeting.pdf`, 2022. Presented at the First Muon Collider Collaboration Meeting.

[287] C. Aimè. Muon R&D. `https://agenda.infn.it/event/33332/contributions/187234/`, 2022. Presented at RD_MUCOL Riunione di Collaborazione - Italia.

[288] C. Aimè et al. Reconstructing muons at a Muon Collider. `https://indico.cern.ch/event/949705/contributions/4555614/attachments/2368733/4047293/179_ChiaraAime.pdf`, 2021. Presented at 30th International Symposium on Lepton Photon Interactions.

[289] C. Aimè et al. Muon detector for a Muon Collider. *Nucl. Instrum. Methods. Phys. Res. A*:167800, 2022.